

POLITECNICO DI MILANO
School of Environmental and Civil engineering



POLO TERRITORIALE DI COMO

Master of Science in Environmental and Geomatic engineering

**GNSS PRECISE POINT POSITIONING FOR
METEOROLOGICAL APPLICATIONS**

Supervisor: Prof. Giovanna VENUTI

Co-Supervisor: Dott. Eugenio REALINI

Master graduation Thesis by:
Davide GALLIANI
Id. 804296

Academic Year 2014/2015

Index

List of Figures	iii
List of Tables.....	v
List of Equations	vii
List of Graphs	viii
Abstract.....	ix
Riassunto	x
Introduction	1
1 GNSS system.....	2
1.1 <i>GPS positioning principle</i>	2
1.2 <i>GPS design.....</i>	3
1.2.1 Space segment	4
1.2.2 Control segment.....	5
1.2.3 User segment	7
1.2.4 Signals.....	7
1.2.5 Operational functioning and observation equations	10
1.3 <i>GPS positioning techniques.....</i>	13
1.3.1 Point positioning	13
1.3.2 Differential positioning.....	15
2 Physics of the atmosphere	17
2.1 <i>Basic concepts.....</i>	17
2.1.1 Equation of state	19
2.1.2 Atmospheric water vapor.....	20
2.1.2.1 Mixing ratio w	20
2.1.2.2 Partial pressure of water vapor and dry air.....	20
2.1.2.3 Specific humidity q	21
2.1.2.4 Relative humidity RH	21
2.1.2.5 Refractivity.....	22
2.1.2.6 Temperature and pressure profiles.....	23

3 Tropospheric delay modelling and Precise Point Positioning	25
3.1 <i>Troposphere delay modelling</i>	25
3.1.1 Azimuthal asymmetry and gradient parameters.....	29
3.2 <i>Precise Point Positioning</i>	32
3.2.1 Parameter estimation in the Bernese GPS Software.....	34
4 Experiments and results	38
4.1 <i>Case study data</i>	38
4.1.1 Mist dataset.....	38
4.1.2 Uji dataset	39
4.2 <i>MisT data processing</i>	40
4.2.1 Effect of troposphere anisotropic model and estimation rate.....	40
4.2.2 Weekly estimation for Mist data.....	47
4.3 <i>UJI data processing</i>	56
4.3.1 Comparison with respect to RTnet solution.....	56
4.3.1.1 Notes about RTnet solution.....	56
4.3.1.2 Solution details	57
4.3.2 Time windows solutions	79
4.4 <i>Results</i>	83
Conclusions and further improvements.....	84
References	85
Acknowledgments	88

List of Figures

Figure 1: Basic idea of GPS positioning (Ahmed, 2008); 1, 2 and 3 are satellites whose coordinate are known and the receiver is somewhere on the Earth.....	3
Figure 2: GNSS architecture (Subirana, Zornoza, & Hernandez-Pajares, 2013)	3
Figure 3: Current GPS space segment.....	4
Figure 4: Actual satellites	5
Figure 5: GPS monitoring stations (Jospeh L. Awange, 2011)	6
Figure 6: IGS stations	7
Figure 7: Composition of the signal (Hofmann-Wellenhof et al., 2008).....	8
Figure 8 GPS errors and biases (Ahmed, 2008)	11
Figure 9: Point positioning	14
Figure 10: Differential positioning	15
Figure 11: Typical vertical structure of atmospheric temperature (K) in the lowest 100 km of the atmosphere (Fleming, Chandra, Barnett, & Corney, 1990).....	17
Figure 12: Possible subdivision schemes of the earth' atmosphere (Seeber, 2003)	18
Figure 13: Temperature and dry-air pressure in the 1976 US Standard Atmosphere	23
Figure 14 Zenithal troposphere delay modelling (Reguzzoni, 2012).....	25
Figure 15 A) Elevation angle η B)Relation between radius difference dr, distance difference ds, and zenith angle z ($z=90^\circ - \eta$) (Kleijer, 2004)	26
Figure 16: Tilting of the tropospheric zenith by angle β ; $\Delta\rho_k \cdot f(z)$ is equivalent to STD (Meindl et al., 2004)	30
Figure 17: Poor satellite configuration	36
Figure 18: BSW screenshot about the so called Relative a priori sigma parameter	37
Figure 19: Como and Dani stations (inter-distance of 9.14km - red line)	38
Figure 20: UJI Network, the dense network of 15 stations covered an area of 67km^2 with a maximum inter-distance of about 10km	39
Figure 21: Total zenith delay for Como station, 26 th October 2008	42
Figure 22: Total zenith delay for Dani station, 26 th October 2008	42
Figure 23: Total zenith delay for Como station, 26 th October 2008	44
Figure 24: Total zenith delay for Dani station, 26 th October 2008	44
Figure 25: Total zenith delay for Como station, 26 th October 2008	46
Figure 26: Total zenith delay for Dani station, 26 th October 2008	46
Figure 27: Total zenith delay for Como station, from 26 th October 2008 to 1 st November 2008 (Mist_11).....	49
Figure 28: Total zenith delay for Dani station, from 26 th October 2008 to 1 st November 2008 (Mist_11).....	49
Figure 29: Total zenith delay for Como station, from 26 th October 2008 to 1 st November 2008 (Mist_12).....	51
Figure 30: Total zenith delay for Dani station, from 26 th October 2008 to 1 st November 2008 (Mist_12).....	51
Figure 31: Total zenith delay for Como station, from 26 th October 2008 to 1 st November 2008 (Mist_13).....	53
Figure 32: Total zenith delay for Dani station, from 26 th October 2008 to 1 st November 2008 (Mist_13).....	53
Figure 33: Total zenith delay solution comparison: A) PPP vs ASI; B) PPP vs EUREF; C) PPP vs BEK	55

Figure 34: Total zenith delay RTnet solution for FPOL station, 26 th July 2012. Note the behavior in the first minutes.....	57
Figure 35: MMKI zenith tropospheric delay, note the strange behavior from 250 th minute to 750 th	59
Figure 36: Tropospheric zenith delay for MMKI station (Uji_7), sigma 0,001 m/min	59
Figure 37: Tropospheric zenith delay for MMKI station, Bernese after linear trend removal solution in red (Uji_7)	62
Figure 38: Tropospheric zenith delay for FPOL station, Bernese after linear trend removal solution in red (Uji_7)	62
Figure 39: Tropospheric zenith delay for FPOL station, Bernese solution in red (Uji_8)	63
Figure 40: Tropospheric zenith delay for FPOL station, Bernese after linear trend removal solution in red (Uji_8)	65
Figure 41: Tropospheric zenith delay for YUTO station, Bernese solution in red (Uji_9)	67
Figure 42: Tropospheric zenith delay for YUTO station, Bernese after linear trend removal solution in red (Uji_9)	67
Figure 43: Tropospheric zenith delay for YUTO station, Bernese solution in red (Uji_10)	70
Figure 44: Tropospheric zenith delay for YUTO station, Bernese after linear trend removal solution in red (Uji_10)	70
Figure 45: Tropospheric zenith delay for YUTO station, Bernese solution in red (Uji_11)	76
Figure 46: Tropospheric zenith delay for YUTO station, Bernese solution in red (Uji_12)	76
Figure 47: Output example after the estimation of an anomalous campaign (Uji_17)	81

List of Tables

Table 1: Fundamental features of codes	9
Table 2: 1976 US Standard Atmosphere.....	24
Table 3: Settings for the estimation in the different campaigns	40
Table 4: Sample size for Como and Dani stations in the different campaigns	40
Table 5: Mist_5 (with gradient estimation) and Mist_5B (without gradient estimation) coordinate for Como station.....	41
Table 6: Mist_5 (with gradient estimation) and Mist_5B (without gradient estimation) coordinate for Dani station.....	41
Table 7: Mist_5 (with gradient estimation) and Mist_5B (without gradient estimation) total zenith delay statistics estimation for Como station	41
Table 8: Mist_5 (with gradient estimation) and Mist_5B (without gradient estimation) total zenith delay statistics estimation for Dani station	41
Table 9: Mist_6 (with gradient estimation) and Mist_6B (without gradient estimation) coordinate for Como station.....	43
Table 10: Mist_6 (with gradient estimation) and Mist_6B (without gradient estimation) coordinate for Dani station.....	43
Table 11: Mist_6 (with gradient estimation) and Mist_6B (without gradient estimation) total zenith delay statistics estimation for Como station	43
Table 12: Mist_6 (with gradient estimation) and Mist_6B (without gradient estimation) total zenith delay statistics estimation for Dani station	43
Table 13: Mist_7 (with gradient estimation) and Mist_7B (without gradient estimation) total zenith delay statistics estimation for Como station	45
Table 14: Mist_6 (with gradient estimation) and Mist_6B (without gradient estimation) total zenith delay statistics estimation for Dani station	45
Table 15: Mist_7 (with gradient estimation) and Mist_7B (without gradient estimation) total zenith delay statistics estimation for Como station	45
Table 16: Mist_7 (with gradient estimation) and Mist_7B (without gradient estimation) total zenith delay statistics estimation for Dani station	45
Table 17: Como and Dani station coordinates from DD processing.....	47
Table 18: Sample size for Como and Dani stations in the different campaigns and processing techniques (PPP = Precise Point Positioning, DD = Double Differences)	47
Table 19: Mist_11 coordinate results from day 26 th October 2008 (Day of Year, DOY, 300) to 1 st November 2008 (Day of Year, DOY, 306) for Como station	48
Table 20: Mist_11 coordinate results from day 26 th October 2008 (Day of Year, DOY, 300) to 1 st November 2008 (Day of Year, DOY, 306) for Dani station	48
Table 21: Mist_11 total zenith delay for Como station (DD = double differences, PPP = precise point positioning)	48
Table 22: Mist_11 total zenith delay for Dani station (DD = double differences, PPP = precise point positioning)	48
Table 23: Mist_12 coordinate results from day 26 October 2008 (Day of Year, DOY, 300) to 1 November 2008 (Day of Year, DOY, 306) for Como station	50
Table 24: Mist_12 coordinate results from day 26 October 2008 (DOY 300) to 1 November 2008 (DOY 306) for Dani station	50
Table 25: Mist_12 total zenith delay for Como station (DD = double differences, PPP = precise point positioning)	50

Table 26: Mist_12 total zenith delay for Dani station (DD = double differences, PPP = precise point positioning).....	50
Table 27: Mist_13 coordinate results from day 26 October 2008 (Day of year, DOY, 300) to 1 November 2008 (Day of year, DOY, 306) for Como station	52
Table 28: Mist_13 coordinate results from day 26 October 2008 (Day of year, DOY, 300) to 1 November 2008 (Day of year, DOY, 306) for Dani station.....	52
Table 29: Mist_13 total zenith delay for Como station (DD = double differences, PPP = precise point positioning).....	52
Table 30: Mist_13 total zenith delay for Dani station (DD = double differences, PPP = precise point positioning).....	52
Table 31: Minimum, maximum, mean, standard deviation values and the number of estimated parameters for PPP (MIST_18 solution) and the three different EUREF products	54
Table 32: Correlation index between PPP and EUREF products, statistics of the differences	54
Table 33: Basic settings for Uji campaigns.....	56
Table 34: Total zenith delay: Comparison between RTnet and Bernese (Uji_7) solutions	58
Table 35: Total zenith delay: Comparison between RTnet solution and Bernese (Uji_7) after linear trend removal	61
Table 36: Total zenith delay: Comparison between RTnet solution and Bernese (Uji_8).....	64
Table 37: Total zenith delay: Comparison between RTnet solution and Bernese after linear trend removal solution (Uji_8).....	66
Table 38: Total zenith delay: Comparison between RTnet solution and Bernese solution (Uji_9)	68
Table 39: Total zenith delay: Comparison between RTnet solution and Bernese after linear trend removal solution (Uji_9).....	69
Table 40: Total zenith delay: Comparison between RTnet solution and Bernese solution (Uji_10).....	71
Table 41: Total zenith delay: Comparison between RTnet solution and Bernese after linear trend removal solution (Uji_10).....	72
Table 42: Mean correlation coefficient for Uji_7, Uji_8, Uji_9 and Uji_10 campaigns	73
Table 43: Angular coefficient between Uji_7, Uji_8, Uji_9 and Uji_10	73
Table 44: Total zenith delay: Comparison between RTnet solution and Bernese solution (Uji_11).....	74
Table 45: Total zenith delay: Comparison between RTnet solution and Bernese solution (Uji_12).....	75
Table 46: Mean correlation coefficient for Uji_7, Uji_11 and Uji_12 campaigns.....	77
Table 47: Sample size of the different campaigns	78
Table 48: Mean and standard deviation for the differences between Bernese and RTnet solutions.....	78
Table 49: Basic information for Uji time windows solutions	79
Table 50: Coordinate results for time windows solutions	80
Table 51: Minimum, maximum, mean and standard deviation of tropospheric zenith delay....	81
Table 52: Coordinate results for Uji_40 (from midday to midnight) and Uji_41 (from six till eighteen)	82
Table 53: Tropospheric zenith delay results for Uji_40 (from midday to midnight) and Uji_41 (from six till eighteen)	82

List of Equations

Equation 1: Distance computation	2
Equation 2: Euclidean distance	2
Equation 3: L1 and L2 frequencies derivation	8
Equation 4: L1 and L2 wavelengths, c is the speed of light	8
Equation 5: Observed delay	10
Equation 6: Rewritten satellite clock term	10
Equation 7: Satellite clock offset approximation	10
Equation 8: Rewrite of receiver clock term	10
Equation 9: GPS observation equation	10
Equation 10: Pseudorange equation for code	11
Equation 11: Pseudorange equation for carrier	11
Equation 12: Simplified observation equations	12
Equation 13: Ionospheric free combination	13
Equation 14: Polynomial model for the satellite clock correction	14
Equation 15: Single difference equation for code	15
Equation 16: Single difference equation for carrier	16
Equation 17: Double difference equation for code	16
Equation 18: Double difference equation for carrier	16
Equation 19: Gas equation	19
Equation 20: Specific volume	19
Equation 21: Specific gas constant	19
Equation 22: Mixing ratio	20
Equation 23: Partial pressure of water vapor (e) and dry air (P_d)	20
Equation 24: Specific humidity	21
Equation 25: Relative humidity	21
Equation 26: Electro-magnetic distance	22
Equation 27: Geometrical distance	22
Equation 28: Excess path length (Slant Troposphere Delay)	22
Equation 29: Refractivity index	23
Equation 30: Scomposed refractivity index	23
Equation 31: Lapse rate, T is the temperature and h the altitude	24
Equation 32: Isothermal pressure profile	24
Equation 33: Pressure profile, T_0 temperature at the base of the layer [K]	24
Equation 34: Slant tropospheric delay equation	25
Equation 35	26
Equation 36: ZTD and STD relation	26
Equation 37: STD hydrostatic and wet part relationship	26
Equation 38: Hydrostatic and Wet zenith delays	27
Equation 39: GMF general equation	27
Equation 40: ZWD general expression	28
Equation 41: PWV	28
Equation 42: PWV approximated ($k' = 1/6$)	29
Equation 43: Integrated Water Vapor (IWV)	29
Equation 44	30
Equation 45	30

Equation 46	30
Equation 47	30
Equation 48	31
Equation 49	31
Equation 50: Linearised geometric distance.....	34
Equation 51: Gauss-Markov model.....	35
Equation 52: RMS conversion from [sec] to [m].....	38
Equation 53: Linear interpolation	60

List of Graphs

Graph 1: Graphical representation of mean correlation coefficients for Uji_7, Uji_8, Uji_9, and Uji_10	73
Graph 2: Graphical representation of mean correlation coefficients for Uji_7, Uji_11 and Uji_12	77

Abstract

The signals emitted by the Global Navigation Satellite System (GNSS) are hampered by a high numbers of physical phenomena. These cause a delay with respect to the theoretical reception time. At present these phenomena are well understood and corrigible. There are two fundamentals adjustment techniques that are exploited to process the raw GNSS data. They are classified as differential or point positioning. The first combines simultaneous observations from two stations to two satellites eliminating errors common within the satellites and within the receivers. The second uses undifferenced observations and therefore requires accurate modelling and/or estimates of the satellite and receiver related errors. This last is the selected technique for this thesis. Moreover the study is focused on the estimation of the tropospheric zenith delays (ZTD). They can be manipulated in order to obtain a measure of precipitable tropospheric water vapor (PWV), both TZD and PWV are employed in numerical weather prediction models for environmental monitoring.

Keywords: *tropospheric delay, precise point positioning, GNSS, PWV*

Riassunto

I segnali emessi dal Sistema Satellitare Globale di Navigazione (GNSS) sono ostacolati da un elevato numero di fenomeni fisici. Questi sono la causa di ritardi nel tempo di ricezione del segnale rispetto al tempo di ricezione teorico. Questi fenomeni sono stati ampiamente analizzati e corretti. Esistono due tecniche di processamento dei dati GNSS grezzi. Queste possono essere classificate in posizionamento differenziale o assoluto. La prima combina osservazioni simultanee da due stazioni verso due satelliti eliminando così errori comuni legati sia ai satelliti sia ai ricevitori. La seconda prevede l'utilizzo di osservazioni non differenziate e quindi richiede un'esatta modellizzazione e/o stima degli errori legati sia ai satelliti che al ricevitore. Quest'ultima è stata adottata in questo lavoro. Lo studio, in particolare, si è focalizzato sulla stima del ritardo troposferico (TZD). Tale ritardo può essere l'input per la derivazione di un indice di vapore d'acqua atmosferico (PWV), entrambi TZD e PWV possono essere impiegati in modelli di previsione meteorologici per monitoraggio ambientale.

Parole chiave: *ritardo troposferico, TZD, posizionamento puntuale di precisione, PPP, GNSS, PWV*

Introduction

The potentialities of the Global Navigation Satellite System (GNSS) are not only linked to the navigation and positioning problems. Analyzing the effects induced by the physical media on the transmitted signals, GNSS can be useful also for environmental monitoring purposes. This approach is innovative if compared to the use GNSS was designed for.

Another innovative aspect lies in the processing technique adopted to the data processing. The Precise Point Positioning (PPP) is an alternative procedure with respect to the Double Differences (DD), but requires some specific corrections in order to be applied with success. It is preferable because no correlation between stations is introduced in the adjustment and allows for a direct estimate of interesting parameters.

In this thesis the Bernese GPS Software is used for the GNSS data processing. It has been developed at the Astronomical Institute of the University of Bern (AIUB). It is also used by the Center of Orbit Determination in Europe (CODE) for its international and European activities.

The purposes of this work are:

- To understand the Precise Point Positioning (PPP) technique
- To estimate tropospheric zenith delays with PPP
- To make comparisons between the obtained results and external solutions
- To derive water vapor indexes starting from the estimated tropospheric delay

Two different datasets are processed. One refers to a local Lombardy region network, the other is from a Japanese network designed, installed and operated by the Laboratory of Atmospheric Sensing and Diagnosis (Tsuda laboratory) of the Research Institute for Sustainable Humanosphere (<http://www.rish.kyoto-u.ac.jp/English/>). It was possible to obtain these data through a cooperation with the Kyoto University.

This document consists of four chapters:

Chapter 1: the GNSS system is described in general terms for what concerns the operative principles, the design and the two fundamental data processing techniques: Precise Point Positioning (PPP) and Double Difference (DD)

Chapter 2: the physics of the atmosphere is shortly described and the needed formulas to derive water vapor indexes are reported.

Chapter 3: the tropospheric delay is discussed in detail for what concerns the two fundamental models utilized in the adjustment procedures; the Precise Point Positioning is discussed in relation to the estimation procedure implemented in the Bernese software.

Chapter 4: experiments and results are presented for the two datasets.

1 GNSS system

The Global Positioning System (GPS) is a satellite-based navigation system developed by the U.S. Department of Defense (DoD) in the early 1970s. Initially, it had to fulfill U.S. military needs. However, it was later made available to civilians, and is now a dual-use system that can be accessed by both military and civilian users (Ahmed, 2008). It was the first satellite system for global navigation to be operative.

With the term Global Navigation Satellite Systems (GNSS) we refer to all the systems of this type. They are: GLONASS (Global Navigation Satellite System) designed by Russia and permanently operating since 2012, Galileo developed by Europe but, until now, not complete, COMPASS-Beidou provided by China and only there permanently operative, it is announced to be available worldwide in 2020, QZSS in Japan and IRNSS in India.

All these services leverage on different microwave radio signals, transmitted from satellites, to make length observations; by means of those observations analysis it is possible to obtain the coordinates of a receiver on earth. Though this is the GNSS main purpose, such measures may also be used to characterize the state of the atmosphere in order to improve meteorological models. There are different algorithms to derive positions and atmosphere parameters. In this thesis we will use the so called Precise Point Positioning adjustment technique.

In the following sections the basic concepts upon GPS are introduced.

1.1 GPS positioning principle

The starting point is the derivation of a distance from a time measurement, that is the travel time of a microwave radio signal. This is done by means of Equation 1.

$$\text{Distance} = \text{Travel Velocity} \cdot \text{Travel Time}$$

Equation 1: Distance computation

The travel velocity, for example, could be the speed of light (299'792'458 m/s) in the vacuum.

Since the Euclidean distance between two points, 1 and 2, can be expressed with:

$$\text{Distance} = \sqrt{(X_1 - X^2)^2 + (Y_1 - Y^2)^2 + (Z_1 - Z^2)^2}$$

Equation 2: Euclidean distance

Having three measurements of distance between a point of unknown coordinates and three different points of known coordinates one can get the unknown coordinates by solving a system.

From the geometrical point of view this corresponds to locate the unknown point at the intersection of three spheres whose radii (R_1, R_2, R_3) are measured Euclidean distances (Figure 1).

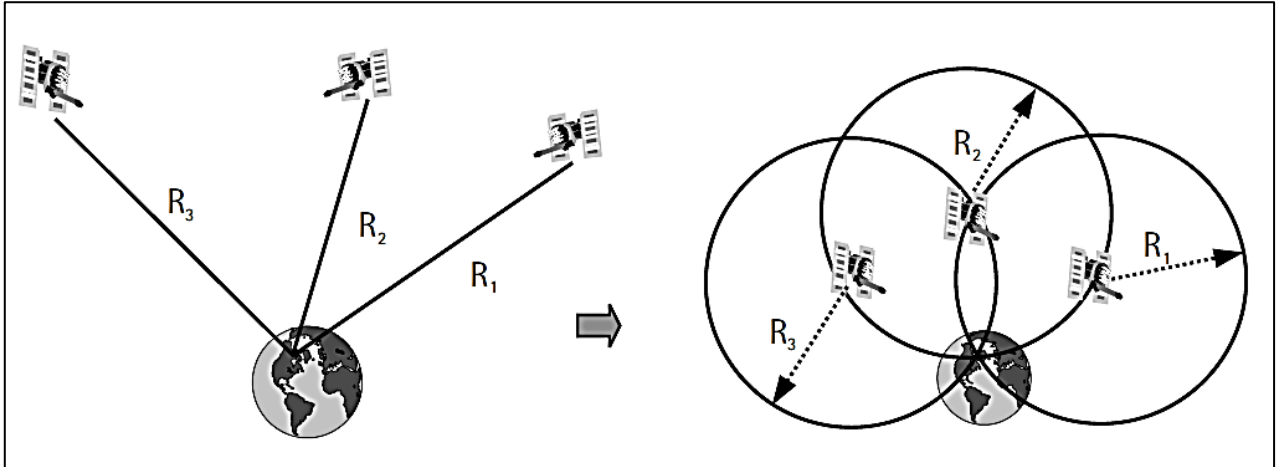


Figure 1: Basic idea of GPS positioning (Ahmed, 2008); 1, 2 and 3 are satellites whose coordinate are known and the receiver is somewhere on the Earth.

It is possible to see from the figure that there are two intersections, so the solution leads to two sets of coordinates. One does not locate the receiver on Earth and therefore is to be discarded. This technique is called trilateration and it is the starting point for the coming discussions.

From the practical point of view a fourth satellite is needed to account for the receiver clock offset (Ahmed, 2008).

1.2 GPS design

The GPS system consists of three macro-blocks (Figure 2) called segments: *Space Segment*, *Control Segment*, *User Segment* (Reguzzoni, 2012).

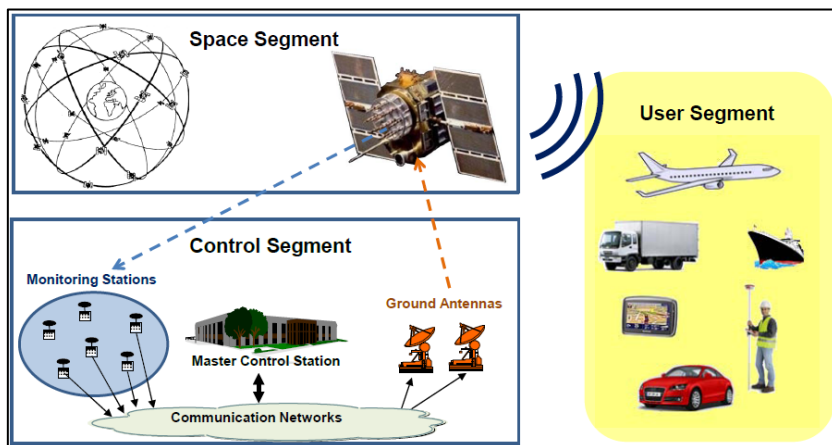


Figure 2: GNSS architecture (Subirana, Zornoza, & Hernandez-Pajares, 2013)

The control segment has the task of satellites monitoring and maintenance. The space segment is the fundamental part of such a system, just like the users.

1.2.1 Space segment

This segment is designed to be made up of 24 satellites plus 4 spare ones orbiting at a height of about 20200 km above the Earth's surface. The constellation consists of 6 orbital planes with an inclination of 55° with respect to the Earth equatorial plane, each orbit contains 4 satellites (Joseph L. Awange & Kiema, 2013).

The orbits are nearly circular and have a semi-major axis of 26560 km. The satellites have a speed of 3,9 km/sec and a nominal period of 12 hours in sidereal time (11 h 58 m 2 s) (Subirana et al., 2013).

With this setup, and an elevation above 15° from the horizon, about 4 to 8 satellites can be observed anywhere on the Earth at anytime. The satellites are made up of solar panels, internal components (atomic clock and radio transmitters) and external components such as antenna. The orientation of the satellite in space is such that the solar panels face the sun, while the antennas face to Earth to transmit and receive radio signals (Joseph L. Awange & Kiema, 2013).

Figure 3 and Figure 4 show the current constellation.

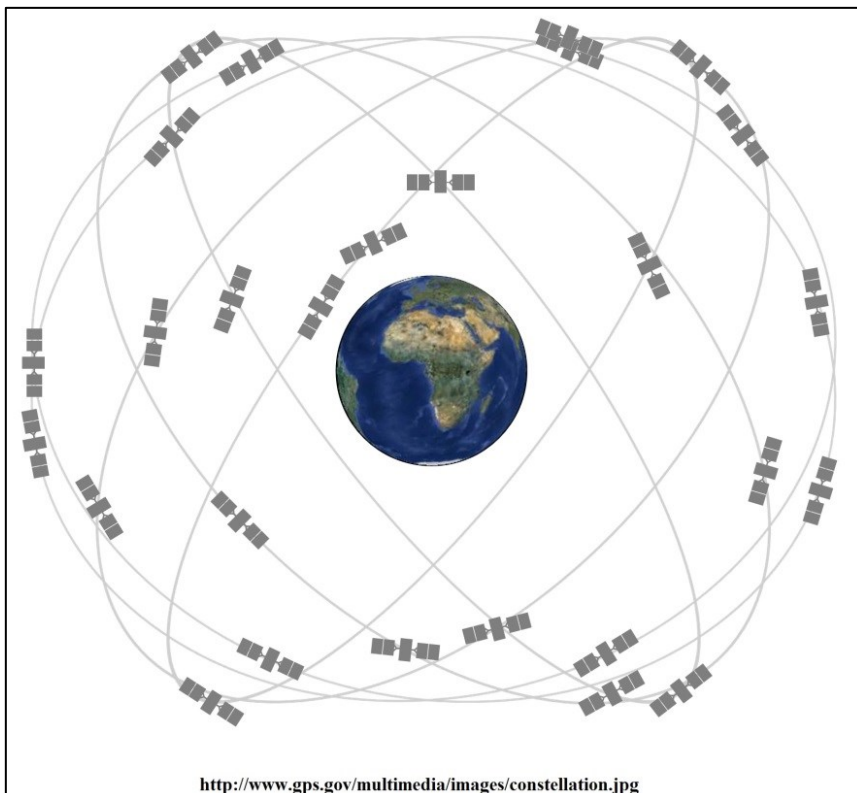


Figure 3: Current GPS space segment

LEGACY SATELLITES			MODERNIZED SATELLITES	
BLOCK IIA	BLOCK IIR	BLOCK IIR(M)	BLOCK IIF	GPS III
3 operational	12 operational	7 operational	9 operational	In production
<ul style="list-style-type: none"> ■ Coarse Acquisition (C/A) code on L1 frequency for civil users ■ Precise P(Y) code on L1 & L2 frequencies for military users ■ 7.5-year design lifespan ■ Launched in 1990-1997 <p>VIEW AIR FORCE FACT SHEET ➔</p>	<ul style="list-style-type: none"> ■ C/A code on L1 ■ P(Y) code on L1 & L2 ■ On-board clock monitoring ■ 7.5-year design lifespan ■ Launched in 1997-2004 <p>VIEW AIR FORCE FACT SHEET ➔</p>	<ul style="list-style-type: none"> ■ All legacy signals ■ 2nd civil signal on L2 (L2C) LEARN MORE ➔ ■ New military M code signals for enhanced jam resistance ■ Flexible power levels for military signals ■ 7.5-year design lifespan ■ Launched in 2005-2009 <p>VIEW AIR FORCE FACT SHEET ➔</p>	<ul style="list-style-type: none"> ■ All Block IIR(M) signals ■ 3rd civil signal on L5 frequency (L5) LEARN MORE ➔ ■ Advanced atomic clocks ■ Improved accuracy, signal strength, and quality ■ 12-year design lifespan ■ Launched since 2010 <p>VIEW AIR FORCE FACT SHEET ➔</p>	<ul style="list-style-type: none"> ■ All Block IIF signals ■ 4th civil signal on L1 (L1C) LEARN MORE ➔ ■ Enhanced signal reliability, accuracy, and integrity ■ No Selective Availability LEARN MORE ➔ ■ Satellites 11+: laser reflectors; search & rescue payload ■ 15-year design lifespan ■ Begins launching in 2016 <p>VIEW AIR FORCE FACT SHEET ➔</p>

Figure 4: Actual satellites

1.2.2 Control segment

The Operational Control System consists of four major subsystems: a Master Control Station (MCS), a Backup Master Control Station (BMCS), a network of four ground antennas (Gas), and a network of globally-distributed monitor stations (MSs).

The master control station (MCS) is located at Schriever Air Force Base, Colorado, and is the central control node for the GPS satellite constellation. Operations are maintained 24 hours a day, seven day a week throughout the year. The MCS is responsible for all aspects of constellation command and control, to include:

- Routine satellite bus and payload status monitoring
- Satellite maintenance and anomaly resolution
- Management of GPS signal in space (SIS) performance in support of all performance standards (Standard positioning service, SPS, and Precise positioning service, PPS)
- Navigational message data upload operations, which are required to sustain performance in accordance with accuracy and integrity standards
- Detecting and responding to GPS signal in space (SIS) failures

The backup master control station (BMC) is located at Gaithersburg, Maryland. (Grimes, 2008)

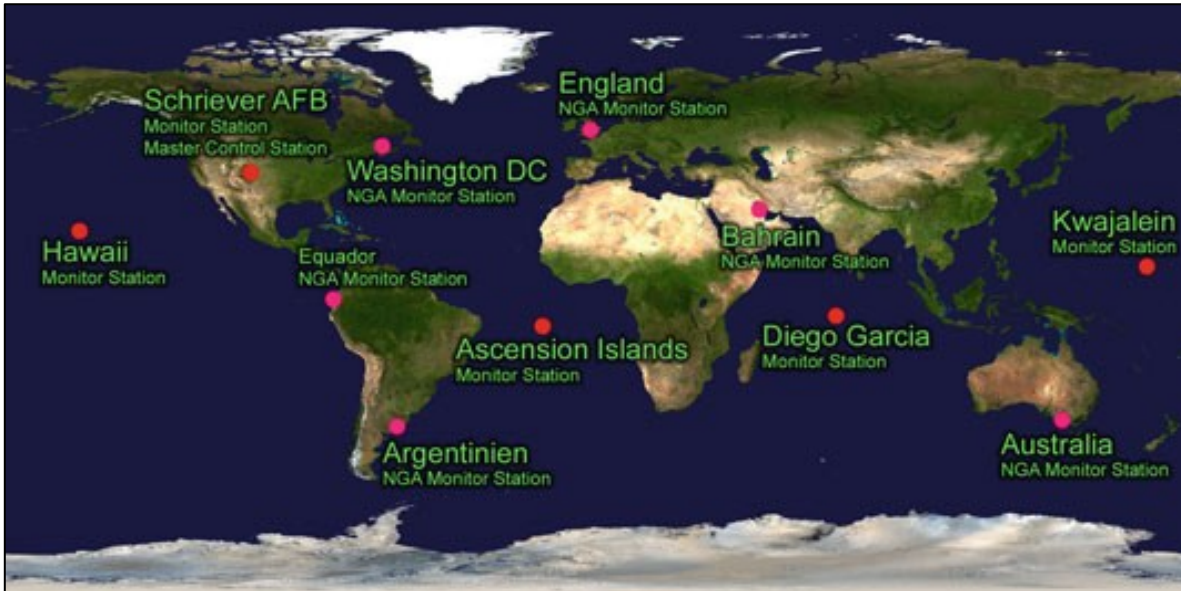


Figure 5: GPS monitoring stations (Jospeh L. Awange, 2011)

The monitoring stations (MSs) are five and are located at Colorado Springs, Ascension Island in the Atlantic Ocean, Hawaii, Diego Garcia in the Indian Ocean, and Kwajalein Island in the Pacific Ocean. In September 2005, six more monitoring stations were added to the network, enabling every satellite to be seen by at least two monitoring stations and thus improving the accuracy of the computed satellite orbital parameters (ephemeris).

Satellite ephemeris consist of the satellite's positions and velocities predicted at given times. These ephemeris records are valid for a maximum of 4h and are updated every hour. These MSs monitor the orbital parameters and send the information to the master station at Colorado Springs. The information obtained from these monitoring stations tracking the satellites are in turn used to control the satellites and predict their orbits. This is done through the processing and analysis of the information by the master station, which computes the satellite ephemeris and clock parameters and transmits them to the satellites (Joseph L. Awange & Kiema, 2013).

There are several ground stations distributed across the world that augment the control system by monitoring and tracking the satellites in space and transmitting correction information to individual satellites through ground antennas. These stations form the International GNSS Service (IGS) network. The ground control network is therefore responsible for tracking and maintaining the satellite constellation by monitoring satellite health and signal integrity, and maintaining satellite orbital configuration (Jospeh L. Awange, 2011).

1.2.3 User segment

The user segment consists of different user categories, receiver types, and various information services. User categories are those of military and civilian users as well as authorized and unauthorized users. Civilian and unauthorized users do not have access to all signals or services of the GNSS. A variety of receiver types is on the market today. One characterization is based on the type of observable signals. Another criterion is the ability to track one, two or even more frequencies. Finally, one has to distinguish between receivers operating for one or more specific GNSS (Hofmann-Wellenhof, Lichtenegger, & Wasle, 2008).

Within the user segment, there are not only portable receivers but also permanent stations; some of these have been grouped by the International GNSS Service (IGS). They perform a control function on the fundamental stations (Reguzzoni, 2012). In Figure 6 IGS stations are reported.

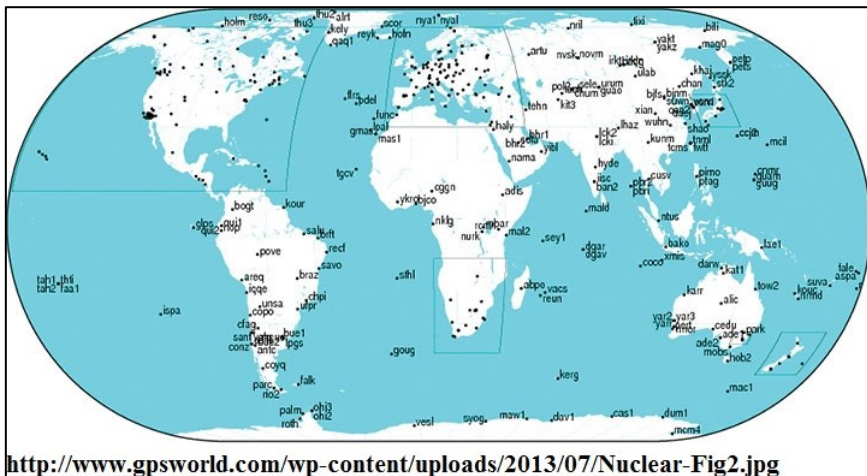


Figure 6: IGS stations

1.2.4 Signals

GNSS are classified as passive one-way downlink ranging systems. This means that only satellites (passive systems) emit signals from space to earth (downlink). The time of transmission to derive ranges and the modelling parameters are included in the signals.

The signals are generated from oscillators (precise atomic clocks) and broadcast through an antenna. These clocks are based on atomic frequency standards which produce the reference frequency by stimulated radiation. The fundamental frequency is 10,23 MHz with a stability over a day in the order of $\Delta f/f = 10^{-12}$ to 10^{-15} .

The final emitted signal is the result of a threefold process, represented in Figure 7.

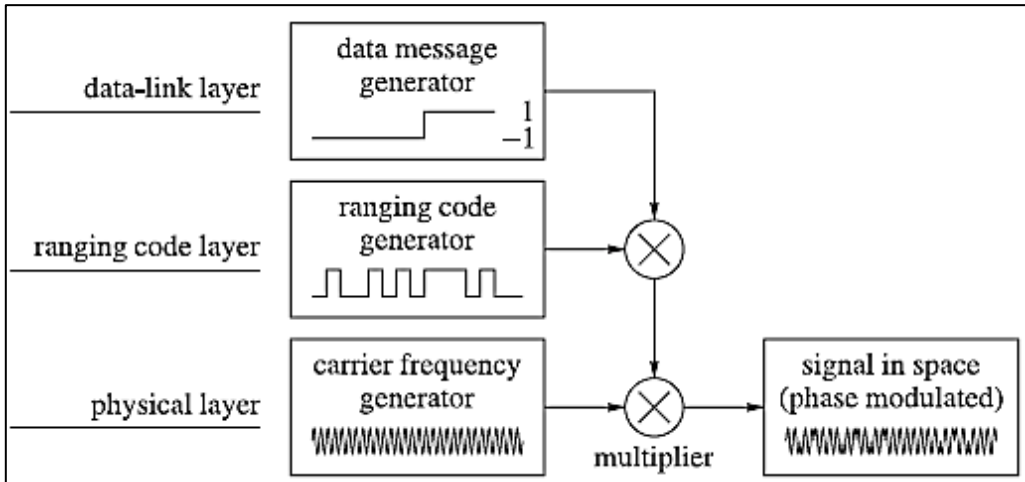


Figure 7: Composition of the signal (Hofmann-Wellenhof et al., 2008)

The physical layer characterizes the physical properties of the transmitted signals. The ranging code layer is based on a continuous but periodically modulated signal exploited within correlation techniques. The periodicity is strictly synchronized to the time system of the satellites and to the data message. The data-link layer commonly contains the time of transmission, satellite ephemerides, etc (Hofmann-Wellenhof et al., 2008).

These signals are generated starting from the following fundamental frequencies:

- L1 and L2 carriers, and L5 (used only for aviation safety services (www.gps.gov))
- Coarse acquisition (C/A), L2C, precise acquisition P(Y) and M codes
- The navigation message (D, navigation data)

The carriers are obtained through integer multiplication:

$$\begin{aligned} L1 &= 154 \cdot f_0 = 1575,42 \text{ MHz} \\ L2 &= 120 \cdot f_0 = 1227,60 \text{ MHz} \end{aligned}$$

Equation 3: L1 and L2 frequencies derivation

Their wavelengths are, respectively:

$$\lambda_1 = \frac{c}{L_1} \cong 19,029 \text{ cm}$$

$$\lambda_2 = \frac{c}{L_2} \cong 24,421 \text{ cm}$$

Equation 4: L1 and L2 wavelengths, c is the speed of light

The codes are sequences of +1 or -1 values impulses that seem to be pseudo random (PRN stands for Pseudo Random Noise). They are modulated onto the carrier frequencies; L1 carries both the C/A and P(Y) codes, while the L2 carries only the P(Y) code.

The fundamental features of these codes are reported in Table 1.

NAME	FREQUENCY [MHz]	WAVELENGTH [m]	NUMBER OF IMPULSES	TOTAL DURATION
C/A	1,023	293,0	1023	1ms
L2C	1,023	293,0	10230	10ms
P(Y)	10,23	29,3	$3,2703264 \cdot 10^{16}$	37 weeks
M	10,23	29,3	unknown	unknown

Table 1: Fundamental features of codes

The public C/A code is different for each satellite and so it is also used by the receiver to identify satellites in view. The P code is more precise than C/A code but it is encrypted (P(Y)) since August 1994, so the US army holds its exclusive use. L2C code is a second civilian ranging code modulated on the L2 carrier frequency but transmitted only from Block IIR-M satellites, as it is reported in Figure 4. The M code is the new encrypted military signal.

The navigation message, D, contains information on the health of the satellite, orbital parameters, generic ionospheric corrections, satellite clock correction parameters, satellite almanac and some information on other satellites. Each message has a 50 Hz frequency and consists of 25 pages and 5 subframes of data. They are composed as follows:

- The first subframe contains GPS week number, satellite accuracy and health, and satellite clock correction terms
- The second and third carry the satellite ephemeris
- The fourth contains ionospheric corrections, satellite health and almanac data for satellites 25-32, special messages, satellite configuration flags, ionospheric and UTC data
- The last subframe contains satellite health and almanac data for satellites 1-24, almanac reference time and week number

The total message length is of 1500 bits.

1.2.5 Operational functioning and observation equations

The positioning principle is explained in section 1.1; one should note that in Equation 1 the travel time is the GPS observed quantity. By knowing three different distances (or times) Equation 2 is resolvable in the stationary receiver coordinates.

More in details the travel time has to be known in a very precise way; this is the reasons of so many signals. These signals are sent by the satellites to the receiver which tries to correlate them with its own internal generated replica. It is possible to compute the signal travel time. In particular, the receiver observes a delay, Equation 5:

$$\Delta T_R^S(t) = T_R(t) - T^S(t - \tau_R^S)$$

T^S = satellite clock when the signal is transmitted
 T_R = receiver clock when the signal is received
 t = GPS temporal scale
 τ_R^S = travel time

Equation 5: Observed delay

The satellite clock term, $T^S(t - \tau_R^S)$, can be rewritten as follows:

$$T^S(t - \tau_R^S) = t - \tau_R^S + dt^S \cdot (t - \tau_R^S)$$

$$dt^S \cdot (t - \tau_R^S) = \text{clock offset}$$

Equation 6: Rewritten satellite clock term

The satellite clock offset can be approximate as in Equation 7:

$$dt^S \cdot (t - \tau_R^S) = dt^S(t)$$

Equation 7: Satellite clock offset approximation

In an analogous way the receiver clock can be treated as in Equation 8:

$$T_R(t) = t + dt_R(t)$$

Equation 8: Rewrite of receiver clock term

The $dt(t)$ terms are the clock biases.

By substituting Equation 6 and Equation 8 in Equation 5 the final observation equation writes:

$$\Delta T_R^S(t) = \tau_R^S + dt_R(t) - dt^S(t)$$

Equation 9: GPS observation equation

In a simplified way code observation equation is obtained by multiplying Equation 9 by the speed of light in vacuum c :

$$P_R^S(t) = c \cdot \Delta T_R^S(t) = c \cdot \tau_R^S + c \cdot (dt_R(t) - dt^S(t))$$

$c \cdot \tau_R^S$ = distance between satellite and receiver

Equation 10: Pseudorange equation for code

The same reasoning is valid also for the carrier observation equation, unless for a term called initial ambiguity, $N_R^S(t)$. It represents the unknown number of cycles between the satellite and the receiver at the signal reception time. The phase pseudo range equation is:

$$L_R^S(t) = c \cdot \Delta T_R^S(t) = c \cdot \tau_R^S + c \cdot (dt_R(t) - dt^S(t)) + \lambda \cdot N_R^S(t)$$

$N_R^S(t)$ = intial ambiguity

Equation 11: Pseudorange equation for carrier

In general code-pseudoranges can achieve an accuracy of about 5-15 m, so they can be used for those environmental applications that do not require higher accuracies such as locating a waste damping site. For accuracies of cm or mm levels, for example monitoring the changing of the sea level, the use of the carrier-phase is necessary (Jospeh L. Awange, 2011).

For a more detailed observation equation, some effects are to be taken into account. In Figure 8 the principal errors and biases affecting GNSS observations are summarized.

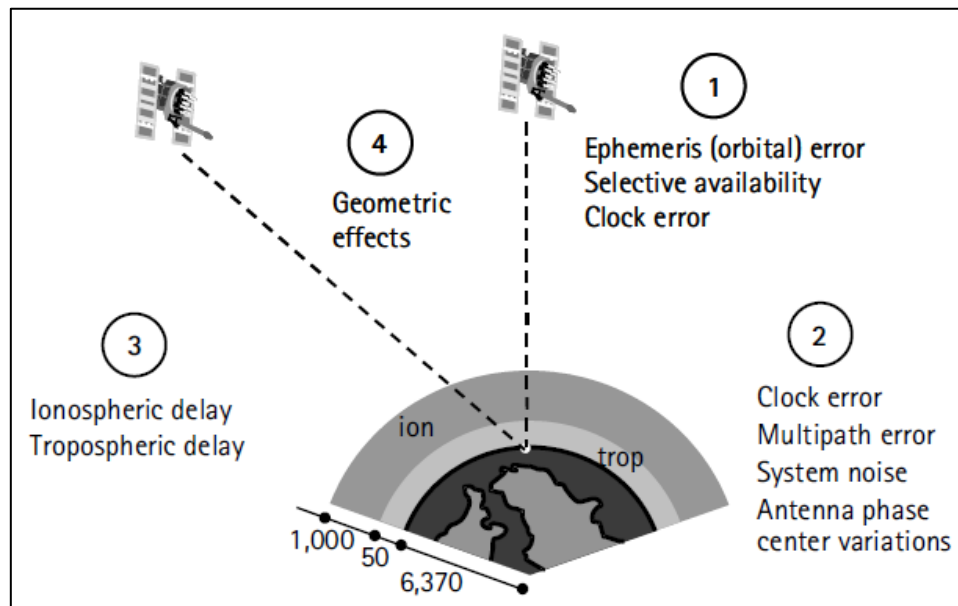


Figure 8 GPS errors and biases (Ahmed, 2008)

These errors can be either systematic or random. For the purposes of this thesis only two systematic errors are discussed. They are the tropospheric and ionospheric delays.

The first is originated in the neutral part of the atmosphere and it is not frequency dependent. So the effect is the same for phase and code measurements. The last is originated in the ionosphere that is a dispersive medium and so this delay is frequency dependent. In particular the ionospheric delay has a different sign for carrier phase and code observations but its absolute value is the same.

Taking into account these two errors, the observation equations are refined and become:

$$\text{code: } P_{1,R}^S(t) = c \cdot \tau_R^S + c \cdot (dt_R(t) - dt^S(t)) + I_{1,R}^S(t) + T_R^S(t)$$

$$\text{code: } P_{2,R}^S(t) = c \cdot \tau_R^S + c \cdot (dt_R(t) - dt^S(t)) + I_{2,R}^S(t) + T_R^S(t)$$

$$\text{phase: } L_{1,R}^S(t) = c \cdot \tau_R^S + c \cdot (dt_R(t) - dt^S(t)) + \lambda_1 \cdot N_{1,R}^S(t) - I_{1,R}^S(t) + T_R^S(t)$$

$$\text{phase: } L_{2,R}^S(t) = c \cdot \tau_R^S + c \cdot (dt_R(t) - dt^S(t)) + \lambda_2 \cdot N_{2,R}^S(t) - I_{2,R}^S(t) + T_R^S(t)$$

Equation 12: Simplified observation equations

where:

$c \cdot \tau_R^S$ = electromagnetic distance between satellite and receiver ($\rho_R^S(t)$)

I_R^S = ionospheric delay in metric term

T_R^S = tropospheric delay in metric term

$dt(t)$ = clock bias

$N_R^S(t)$ = initial ambiguity

λ = carrier wavelength

the subscripts 1 or 2 refers to the correspondent signal frequency of code, or phase,

A detailed discussion about observation equations can be found in (Kleijer, 2004). For the purposes of this thesis work Equation 12 is considered as a reference.

It is possible to relate the ionospheric delays of the two carriers with the following equation:

$$I_{2,R}^S(t) = \frac{f_1^2}{f_2^2} \cdot I_{1,R}^S(t)$$

And so the observation equations become:

$$\text{code: } P_{1,R}^S(t) = c \cdot \tau_R^S + c \cdot (dt_R(t) - dt^S(t)) + I_{1,R}^S(t) + T_R^S(t)$$

$$\text{code: } P_{2,R}^S(t) = c \cdot \tau_R^S + c \cdot (dt_R(t) - dt^S(t)) + \frac{f_1^2}{f_2^2} \cdot I_{1,R}^S(t) + T_R^S(t)$$

$$\text{phase: } L_{1,R}^S(t) = c \cdot \tau_R^S + c \cdot (dt_R(t) - dt^S(t)) + \lambda_1 \cdot N_{1,R}^S(t) - I_{1,R}^S(t) + T_R^S(t)$$

$$\text{phase: } L_{2,R}^S(t) = c \cdot \tau_R^S + c \cdot (dt_R(t) - dt^S(t)) + \lambda_2 \cdot N_{2,R}^S(t) - \frac{f_1^2}{f_2^2} \cdot I_{1,R}^S(t) + T_R^S(t)$$

It is also possible to combine the above equations in order to obtain other ones.
Here the *Ionospheric Free combination* is reported.

$$L_{3,R}^S(t) = \beta_1 \cdot L_{1,R}^S(t) + \beta_2 \cdot L_{2,R}^S(t)$$

$$\beta_1 = \frac{f_1^2}{f_1^2 - f_2^2} = \frac{154^2}{154^2 - 120^2} \cong 2,55$$

$$\beta_2 = -\frac{f_2^2}{f_1^2 - f_2^2} = \frac{120^2}{154^2 - 120^2} \cong -1,55$$

The result is:

$$L_{3,R}^S(t) = c \cdot \tau_R^S + c \cdot (dt_R(t) - dt^S(t)) + \lambda_3 \cdot N_{3,R}^S(t) + T_R^S(t)$$

Equation 13: Ionospheric free combination

This combination remove the ionospheric delay and it is used for the Precise Point Positioning.

1.3 GPS positioning techniques

There are two fundamentals techniques based on the number of GPS receivers involved in the positioning. They are:

- Point, or absolute, positioning, only one receiver is used to determine its position
- Differential, or relative, positioning, in this case two receivers are employed, one of known position, the reference, the other of position to be determined

It is very important to keep in mind the reason why GPS was developed: to determine at an instant the location of a soldier, ship, plane, helicopter, etc. without any equipment other than a single GPS receiver and antenna. This is often referred to as absolute positioning. Without satisfying this requirement, there would be no GPS (Teunissen & Kleusberg, 1998).

GPS relative positioning employs two receivers simultaneously tracking the same satellites. If both receivers track at least four common satellites, a positioning accuracy level of the order of a sub-centimeter to a few meters can be obtained (Ahmed, 2008).

1.3.1 Point positioning

The point positioning can be done both with code and phase measurements. This latter case is called Precise Point Positioning and is discussed in detail in chapter 3.

In this section only few hints are given for point positioning with code measurements.

To determine the receiver position at any time, at least coordinates of four different satellites as well as the corresponding ranges are required (Figure 9).

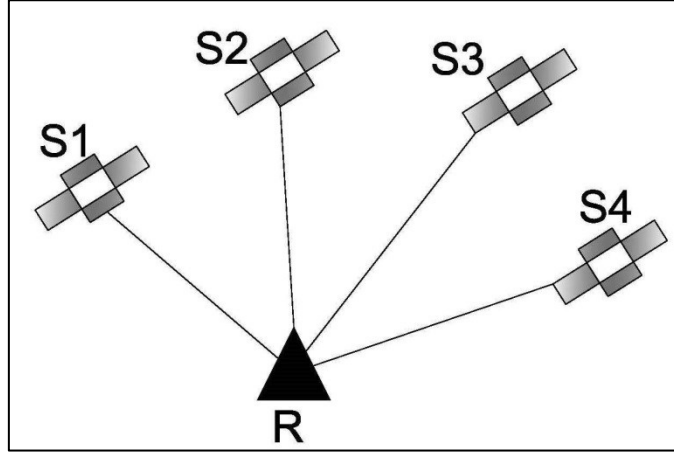


Figure 9: Point positioning

The receiver gets the satellite coordinates through the navigation message, while the pseudo-distances are obtained from either the C/A code or P(Y) code, depending on the receiver type (civilian or military). The measured pseudo-distances are contaminated by both the satellite and receiver clock synchronization errors. Correcting the satellite clock errors may be done by applying the satellite clock correction in the navigation message; the receiver clock error is treated as an additional unknown parameter in the estimation process. This brings the total number of unknown parameters to four: three receiver coordinates and one receiver clock error. This is why least four satellite are needed (Ahmed, 2008).

The reference equation is Equation 12. The ionospheric and tropospheric delays are calculated by a-priori models, so that Equation 12 contains only the geometric distance ($c \cdot \tau_R^S$) and the clock biases.

The satellite clock bias is corrected with a polynomial model of the type showed in Equation 14:

$$dt^S(t) = a_0 + a_1 \cdot (t - t_c) + a_2 \cdot (t - t_c)^2$$

Equation 14: Polynomial model for the satellite clock correction

When the coefficients a_i are transmitted by the satellite in the navigation message with a reference time t_c .

The least squares technique is adopted to solve the system of at least four observations. Note that the balance between the number of equations and the number of unknowns does not guarantee the system solvability. This aspect is discussed in detail in chapter 3.

The worst achievable order of accuracy of point positioning with codes is 22 meter (Ahmed, 2008).

1.3.2 Differential positioning

Differential positioning is a technique where two or more receivers are used. One receiver, usually fixed, is the reference station with (assumed) known coordinates while the remote receivers can be fixed or roving and their coordinates are to be determined (Hofmann-Wellenhof et al., 2008). This situation is represented in Figure 10, where **R1** is the reference station and **R2** the rover.

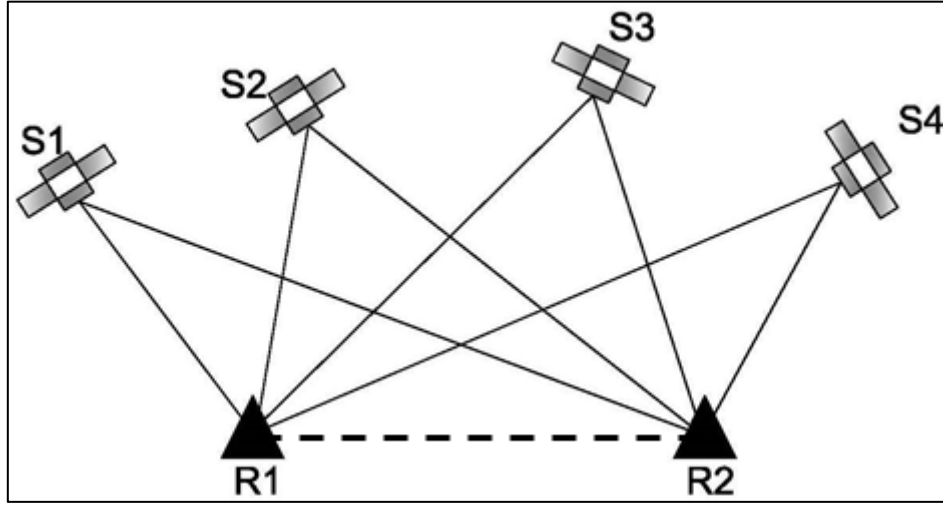


Figure 10: Differential positioning

The double differences method is used to perform a relative positioning. With this technique common systematic errors are eliminated, clock biases of the satellites, or made negligible, for example tropospheric delays if receivers are close enough. Using carrier phase observations for a long period static session, very high accuracies can be achieved by such-technique, even below a millimeter level (Reguzzoni, 2012).

This technique was used to obtain the reference solution explained in section 4.2.2.

Since the purpose of this thesis regards the use of Precise Point Positioning technique, the double differences (DDs) method is not explained in detail but only the basics equations are reported.

The computation of single differences (SDs) is the starting point. The SDs are differences between the observations of receiver 1 (R1) and receiver 2 (R2) to the same satellites. The SDs equations are done both on codes and carriers. So starting from Equation 12 it is possible to write:

$$\begin{aligned}
 P_{R1,R2}^S(t) &= P_{R1}^S(t) - P_{R2}^S(t) \\
 &= \rho_{R1}^S(t) - \rho_{R2}^S(t) + c \cdot (dt_{R1}(t) - dt_{R2}(t)) - c \cdot (dt^S(t) - dt^S(t)) + T_{R1}^S(t) - T_{R2}^S(t) \\
 &\quad + I_{R1}^S(t) - I_{R2}^S(t) \\
 &= \rho_{R1}^S(t) - \rho_{R2}^S(t) + c \cdot (dt_{R1}(t) - dt_{R2}(t)) + T_{R1}^S(t) - T_{R2}^S(t) + I_{R1}^S(t) - I_{R2}^S(t)
 \end{aligned}$$

Equation 15: Single difference equation for code

$$\begin{aligned}
L_{R1,R2}^S(t) &= L_{R1}^S(t) - L_{R2}^S(t) \\
&= \rho_{R1}^S(t) - \rho_{R2}^S(t) + c \cdot (dt_{R1}(t) - dt_{R2}(t)) - c \cdot (dt^S(t) - dt^S(t)) + T_{R1}^S(t) - T_{R2}^S(t) \\
&\quad - I_{R1}^S(t) + I_{R2}^S(t) + \lambda \cdot (N_{R1}^S(t) - N_{R2}^S(t)) \\
&= \rho_{R1}^S(t) - \rho_{R2}^S(t) + c \cdot (dt_{R1}(t) - dt_{R2}(t)) + T_{R1}^S(t) - T_{R2}^S(t) + I_{R1}^S(t) - I_{R2}^S(t) \\
&\quad + \lambda \cdot (N_{R1}^S(t) - N_{R2}^S(t))
\end{aligned}$$

Equation 16: Single difference equation for carrier

These equations have the advantage that many common error sources are eliminated or reduced, the disadvantage is that only relative positions can be estimated. Moreover, the receiver clock bias is still unknown, and very unpredictable. For these reasons it is preferred to use the double difference method. The DDs equations are formed subtracting two SDs measured to two satellites S1 and S2. So starting from Equation 15 and Equation 16 it is possible to write:

$$\begin{aligned}
P_{R1,R2}^{S1,S2}(t) &= P_{R1}^{S1}(t) - P_{R2}^{S2}(t) \\
&= \rho_{R1}^{S1}(t) - \rho_{R2}^{S1}(t) - \rho_{R1}^{S2}(t) + \rho_{R2}^{S2}(t) + T_{R1}^{S1}(t) - T_{R2}^{S1}(t) - T_{R1}^{S2}(t) + T_{R2}^{S2}(t) + I_{R1}^{S1}(t) \\
&\quad - I_{R2}^{S1}(t) - I_{R1}^{S2}(t) + I_{R2}^{S2}(t) + c \cdot (dt_{R1}(t) - dt_{R2}(t)) - c \cdot (dt_{R1}(t) - dt_{R2}(t)) \\
&= \rho_{R1}^{S1}(t) - \rho_{R2}^{S1}(t) - \rho_{R1}^{S2}(t) + \rho_{R2}^{S2}(t) + T_{R1}^{S1}(t) - T_{R2}^{S1}(t) - T_{R1}^{S2}(t) + T_{R2}^{S2}(t) + I_{R1}^{S1}(t) \\
&\quad - I_{R2}^{S1}(t) - I_{R1}^{S2}(t) + I_{R2}^{S2}(t)
\end{aligned}$$

Equation 17: Double difference equation for code

$$\begin{aligned}
L_{R1,R2}^S(t) &= L_{R1}^S(t) - L_{R2}^S(t) \\
&= \rho_{R1}^{S1}(t) - \rho_{R2}^{S1}(t) - \rho_{R1}^{S2}(t) + \rho_{R2}^{S2}(t) + T_{R1}^{S1}(t) - T_{R2}^{S1}(t) - T_{R1}^{S2}(t) + T_{R2}^{S2}(t) - I_{R1}^{S1}(t) \\
&\quad + I_{R2}^{S1}(t) + I_{R1}^{S2}(t) - I_{R2}^{S2}(t) + \lambda \cdot (N_{R1}^{S1}(t) - N_{R2}^{S1}(t) - N_{R1}^{S2}(t) + N_{R2}^{S2}(t)) \\
&\quad + c \cdot (dt_{R1}(t) - dt_{R2}(t)) - c \cdot (dt_{R1}(t) - dt_{R2}(t)) \\
&= \rho_{R1}^{S1}(t) - \rho_{R2}^{S1}(t) - \rho_{R1}^{S2}(t) + \rho_{R2}^{S2}(t) + T_{R1}^{S1}(t) - T_{R2}^{S1}(t) - T_{R1}^{S2}(t) + T_{R2}^{S2}(t) - I_{R1}^{S1}(t) \\
&\quad + I_{R2}^{S1}(t) + I_{R1}^{S2}(t) - I_{R2}^{S2}(t) + \lambda \cdot (N_{R1}^{S1}(t) - N_{R2}^{S1}(t) - N_{R1}^{S2}(t) + N_{R2}^{S2}(t))
\end{aligned}$$

Equation 18: Double difference equation for carrier

In all of these equations the symbols have the same meaning explained in section 1.2.5.

In this method, random errors due to measurement noise and multipath are increased. On the other hand, the motivation for double differencing is to remove clock bias which would create much larger errors. The initial ambiguities remains integer. This technique improve integrity: if a GPS satellite broadcasts bad data, they are detected by the reference station since its position is known.

The following aspects have to be pointed out for this method:

- It is impossible to estimate absolute total zenith delay (TZD) with respect to a specified satellite
- Any systematic effects due to unmodeled atmospheric errors are generally increased, moreover if the meteorological conditions in the two sites are very different the error can increase linearly with the inter-distance between the stations

2 Physics of the atmosphere

In this chapter an overview about atmosphere is given. A particular attention is reserved to the troposphere layer responsible for different kinds of GPS signal delay as explained in chapter 3. So the other atmosphere layers are not discussed in detail.

2.1 Basic concepts

The Earth's atmosphere is quite complex to be modelled and, for this reason, it is useful to divide it into several concentric layers.

According to the variation of temperature with height, the layer from the ground up to about 15 km of altitude, in which the temperature decreases with height, is called troposphere and is bounded above by the tropopause. The layer from the tropopause to about 50 km altitude, in which temperature rises with altitude, is called stratosphere and is bounded above by the stratopause. The layer from the stratopause to about 85-90 km, in which the temperature again falls with altitude, is called the mesosphere and is bounded above by the mesopause. Above the mesopause is the thermosphere, in which the temperature again rises with altitude (Andrews, 2010). In Figure 11 a graphical representation of this temperature behavior is given.

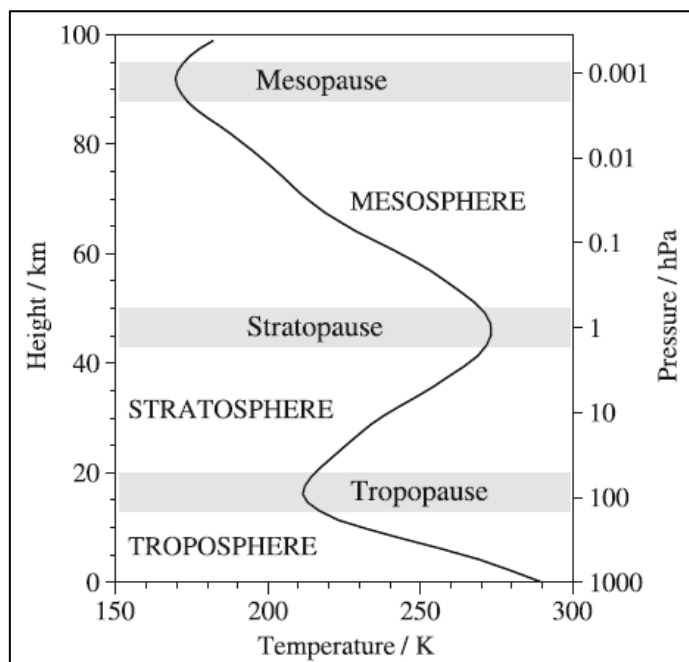


Figure 11: Typical vertical structure of atmospheric temperature (K) in the lowest 100 km of the atmosphere
(Fleming, Chandra, Barnett, & Corney, 1990)

The troposphere is also called the lower atmosphere. It is here that most 'weather' phenomena, such as cyclones, fronts, hurricanes, rain, snow, thunder and lightning, occur. The stratosphere and mesosphere together are called the middle atmosphere. Above the middle atmosphere is the upper atmosphere, or ionosphere, where effects of ionization become dominant in determining the atmospheric structure and the air becomes so rarefied that the assumption that it can be treated as a continuous fluid starts to break down (Andrews, 2010).

From the GPS signals point of view, the earth's atmosphere affects them in three possible ways:

1. A propagation delay is caused
2. A bending of the ray path is caused
3. The signal is absorbed

Basically these phenomena happen in the lower and the upper atmosphere.

The upper atmosphere is a dispersive medium, which means that the propagation delay is frequency dependent. The lower atmosphere is a nondispersive medium, instead. The troposphere is also referred to as a neutral atmosphere to distinguish with its original definition, which is actually based on the characterizing temperature profile (Kleijer, 2004).

In Figure 12 different schemes for the subdivision of the atmosphere are represented and, from the GPS signals point of view, the propagation column is used for the atmosphere classification.

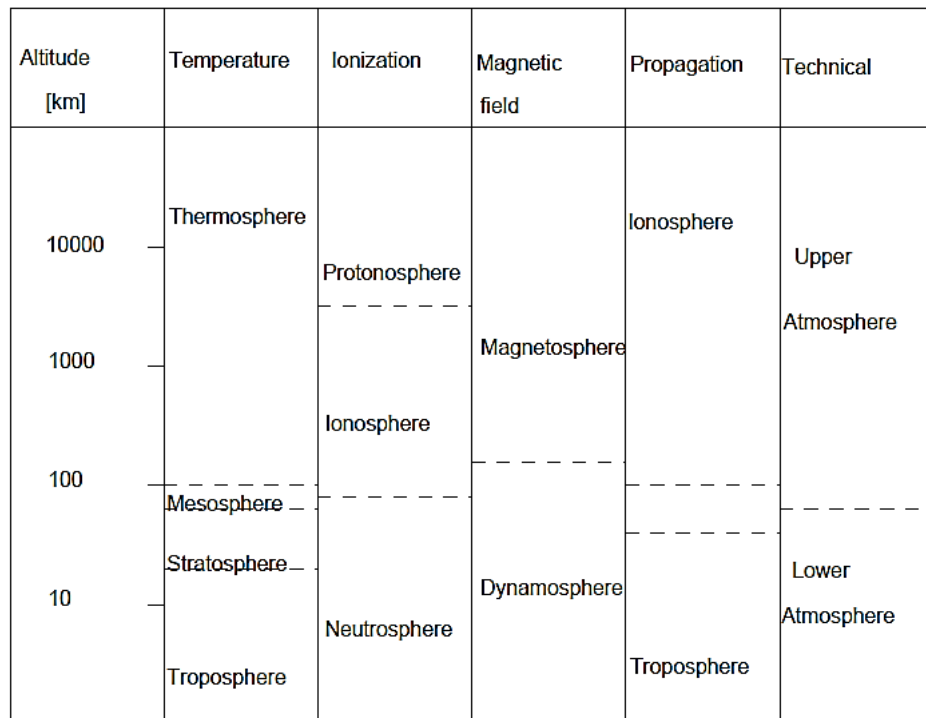


Figure 12: Possible subdivision schemes of the earth's atmosphere (Seeber, 2003)

In the next subsections physical law and equations are given. These laws are useful for the derivation of two indexes: the *Integrated water vapor* (*IWV*), and *Precipitable water vapor* (*PWV*). These are explained in chapter 3.

2.1.1 Equation of state

Starting from the three laws of gases (Champion, 1960), it is possible to define the gas equation or equation of state for perfect ideal gases:

$$\alpha \cdot P = R_i \cdot T$$

Equation 19: Gas equation

with:

$$\alpha = \text{specific volume} \left[\frac{m^3}{kg} \right]$$

$$P = \text{pressure} \left[\frac{N}{m^2} \right]$$

$$R_i = \text{specific gas constant} \left[\frac{J}{kg K} \right]$$

$$T = \text{temperature} [K]$$

The specific volume α is defined as:

$$\alpha \doteq \frac{1}{\rho} \doteq \frac{V}{m}$$

Equation 20: Specific volume

with:

$$\rho = \text{density} \left[\frac{kg}{m^3} \right]$$

$$V = \text{volume} [m^3]$$

$$m = \text{mass} [kg]$$

The specific gas constant R_i (for the i th gas) is related to the universal gas constant by:

$$R_i \cdot M_i \doteq R$$

Equation 21: Specific gas constant

with:

$$M_i = (\text{mean})\text{molecular mass} \left[\frac{kg}{mol} \right]$$

$$R = \text{universal gas constant} \left[8,31434 \frac{J}{mol K} \right]$$

The gases in the troposphere are nearly perfect, although there are no perfect gases. The equation of state doesn't only hold for one specific gas, but also for a mixture of gases. In that case, P is the sum of the partial pressures, R_i is the specific gas constant of the mixture, and M_i is the mean molecular mass of the mixture.

2.1.2 Atmospheric water vapor

The troposphere contains both dry air and water vapor. Dry air has no significant variation in composition with latitude and height (Smith & Weintraub, 1953). The amount of water vapor varies widely, both spatially and temporally. Most of the water vapor is contained in the boundary layer, the lowest 2 km of the troposphere. Water also appears in the troposphere in liquid phase (fog, clouds, rain) and solid form (snow, ice), and is the most important constituent in relation to weather processes, not only because of rain and snowfall but also because large amount of energy are released in the condensation process (Kleijer, 2004).

In the next some water-vapor related indexes are reported.

2.1.2.1 Mixing ratio (w)

The mixture of dry air and water vapor is called moist air. A measure of moisture content is the mixing ration, which is defined as the quotient of water-vapor mass per unit mass dry air (Haltiner & Martin, 1957). The equation is:

$$w \doteq \frac{m_v}{m_d} = \frac{\frac{m_v}{V}}{\frac{m_d}{V}} = \frac{\rho_v}{\rho_d}$$

Equation 22: Mixing ratio

with:

w = mixing ratio [-]

m_v = mass of water vapor [kg]

m_d = mass of dry air [kg]

V = volume [m^3]

ρ_v = density of water vapor $\left[\frac{kg}{m^3}\right]$

ρ_d = density of dry air $\left[\frac{kg}{m^3}\right]$

2.1.2.2 Partial pressure of water vapor and dry air

Applying Equation 19, equation of state, and Equation 20, equation for specific volume, for both water vapor and dry air the following relations are obtained:

$$e = \rho_v \cdot R_v \cdot T$$

$$P_d = P - e = \rho_d \cdot R_d \cdot T$$

Equation 23: Partial pressure of water vapor (e) and dry air (P_d)

where:

$$e = \text{partial pressure of water vapor} \left[\frac{N}{m^2} \right]$$

$$P_d = \text{partial pressure of dry air} \left[\frac{N}{m^2} \right]$$

$$P = \text{total pressure of moist air} \left[\frac{N}{m^2} \right]$$

$$R_v = \text{specific gas constant of water vapor} \left[\frac{J}{kg K} \right]$$

$$R_d = \text{specific gas constant of dry air} \left[\frac{J}{kg K} \right]$$

2.1.2.3 Specific humidity (q)

The specific humidity is defined as the mass of water vapor per unit mass of moist air (Mendes, 1999), as a first approximation the following equation is valid:

$$q = \frac{\rho_v}{\rho_m} \approx w$$

Equation 24: Specific humidity

with:

$$\rho_v = \text{density of water vapor} \left[\frac{kg}{m^3} \right]$$

$$\rho_m = \text{density of moist air} \left[\frac{kg}{m^3} \right]$$

2.1.2.4 Relative humidity (RH)

The relative humidity with respect to water is the ratio (expressed as a percentage) of the actual mixing ratio w of the air to the saturation mixing ratio w_s with respect to a plane surface of pure water at the same temperature and pressure (Wallace & Hobbs, 2006); the equation is:

$$RH = 100 \cdot \frac{w}{w_s} \cong 100 \cdot \frac{e}{e_s}$$

Equation 25: Relative humidity

where:

$$w_s = \frac{m_{vs}}{m_d} = \text{saturation mixing ratio [-]}$$

$$e_s = \text{partial pressure of saturated water vapor} \left[\frac{N}{m^2} \right]$$

$$m_{vs} = \text{mass of saturated water vapor [kg]}$$

2.1.2.5 Refractivity

This is a useful index that allows to define different tropospheric delay as explained in chapter 3.

The total delay of a radio signal caused by the neutral atmosphere depends on the refractivity along the traveled path, and the refractivity depends on pressure and temperature along the path. The basic physical law for the propagation is Fermat's principle: light (or any electro-magnetic wave) will follow the path between two points involving the least travel time. The electro-magnetic distance, between source and receiver, is defined as:

$$S \doteq \int c dt = \int \frac{c}{v} ds = \int_s n(s) ds$$

Equation 26: Electro-magnetic distance

where:

S = electro – magnetic distance [m]

s = electro – magnetic path [m]

c = speed of light in vacuum $\left[\frac{m}{s}\right]$

$v = \frac{ds}{dt}$ = propagation speed $\left[\frac{m}{s}\right]$

$n = \frac{c}{v}$ = refraction index [-]

In general n is considered a complex number. The imaginary part relates to absorption whereas the real part relates to the delay and bending (Hall, Barcley, & Hewitt, 1996). Denoting with L the geometrical distance:

$$L = \int_l dl$$

Equation 27: Geometrical distance

with:

L = geometrical distance [m]

l = geometrical path [m]

The excess path length, called *Slant Troposphere delay*, becomes :

$$S - L = \int_s (n(s) - 1) ds + \left\{ \int_s ds - \int_l dl \right\}$$

Equation 28: Excess path length (Slant Troposphere Delay)

The first term on the right-hand side is the excess path length caused by the propagation delay, whereas the second term (between braces) is the excess path length caused by ray bending. The *Slant Troposphere delay* is evaluated in terms of a distance.

Because the value of the refractive index is close to 1, often the refractivity N (Neper) is used:

$$N = (n - 1) \cdot 10^6$$

Equation 29: Refractivity index

where:

N = refractivity [-]

Usually the range of N in the atmosphere is between 0 and 300.

Since the neutral atmosphere contains both dry air and water vapor, the refractivity can also be split into a dry and a vapor part (Smith & Weintraub, 1953). The expression now becomes:

$$N = N_d + N_w$$

Equation 30: Scomposed refractivity index

where:

N_d = refractivity of dry air [-]

N_w = refractivity of wet air [-]

This makes sense because the mixing ratio of dry-air constituents remains nearly constant in time while the water-vapor content fluctuates widely both spatially and temporally (Kleijer, 2004).

2.1.2.6 Temperature and pressure profiles

The propagation delay depends on the refractivity along the ray path, and the refractivity in turn depends on temperature and pressure. It is important to create a theoretical profile for temperature and pressure that can be used to determine the propagation delay.

Figure 13 shows a model temperature and pressure profile for the neutral atmosphere (Kleijer, 2004). The relationship showed in this figure are also reported in Table 2.

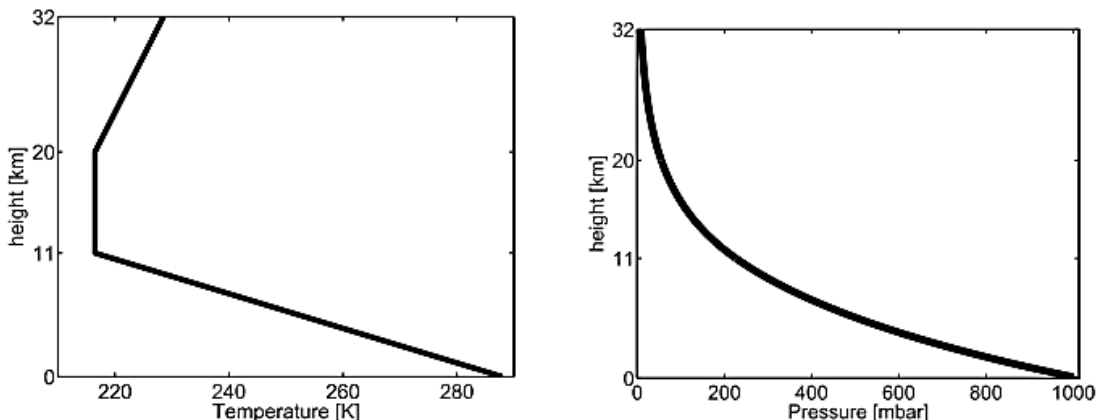


Figure 13: Temperature and dry-air pressure in the 1976 US Standard Atmosphere

The troposphere is characterized by a decreasing temperature. The measure of decrease is called lapse rate and its expression is:

$$\beta \doteq -\frac{dT}{dh}$$

Equation 31: Lapse rate, T is the temperature and h the altitude

The lapse rate varies throughout the atmosphere, but is frequently constant in thick layers (Haltiner & Martin, 1957).

Considering isothermal layers, like tropopause, the pressure profile is given from:

$$P_d = P_{d0} \cdot \exp\left(-\frac{h - h_0}{H}\right)$$

$$H = \frac{R_d \cdot T}{g}$$

Equation 32: Isothermal pressure profile

where:

P_{d0} = pressure of dry air at the base of the layer [mbar]

h = height above msl [km]

h_0 = height above msl at the base of the layer [km]

H = scale height [km]

For the troposphere the assumption of isothermal layer cannot be adopted and so the equation becomes:

$$P_d = P_{d0} \cdot \left(\frac{T}{T_0}\right)^{\mu+1}$$

$$\mu \doteq \frac{g}{R_d \cdot \beta} - 1$$

Equation 33: Pressure profile, T_0 temperature at the base of the layer [K]

Troposphere delay models often use standard values for the temperature and pressure. An example of a standard atmosphere is the 1975 US Standard Atmosphere (Stull, 1995):

Troposphere: $T = 288,15 - 6,5h$	$0 < h < 11 \text{ km}$
Tropopause: $T = 216,65$	$11 < h < 20 \text{ km}$
Stratosphere: $T = 216,65 + h - 20$	$20 < h < 32 \text{ km}$
Troposphere: $P_d = 1013,25(288,15/T)^{-5,255877}$	$0 < h < 11 \text{ km}$
Tropopause: $P_d = 226,32\exp(-0,1568(h-11))$	$11 < h < 20 \text{ km}$
Stratosphere: $P_d = 54,749(216,65/T)^{34,16319}$	$20 < h < 32 \text{ km}$

Table 2: 1976 US Standard Atmosphere

3 Tropospheric delay modelling and Precise Point Positioning

In this chapter are explained in details both the tropospheric delay modelling and Precise Point Positioning performed in the Bernese software.

3.1 Troposphere delay modelling

The lower part of the atmosphere (troposphere) induces delays on GNSS signals that can be estimated during the positioning process. Since most of the atmospheric water vapor is contained in the tropospheric layers, generally within the first 10 km of altitude from the ground, it is possible to estimate the amount of precipitable water vapor (PWV) from the analysis of GNSS tropospheric delays: the estimated signal delay due to the tropospheric refractivity along each receiver-satellite line-of-sight, or slant total (or tropospheric) delay (STD), is mapped to the zenith direction to retrieve the zenith total (or tropospheric) delay (ZTD), which is in turn divided in its hydrostatic and wet components, in order to estimate the PWV over a GNSS station antenna (<http://www.g-red.eu/techniques-methods/gnss-meteorology/>).

Figure 14 shows the situation described above.

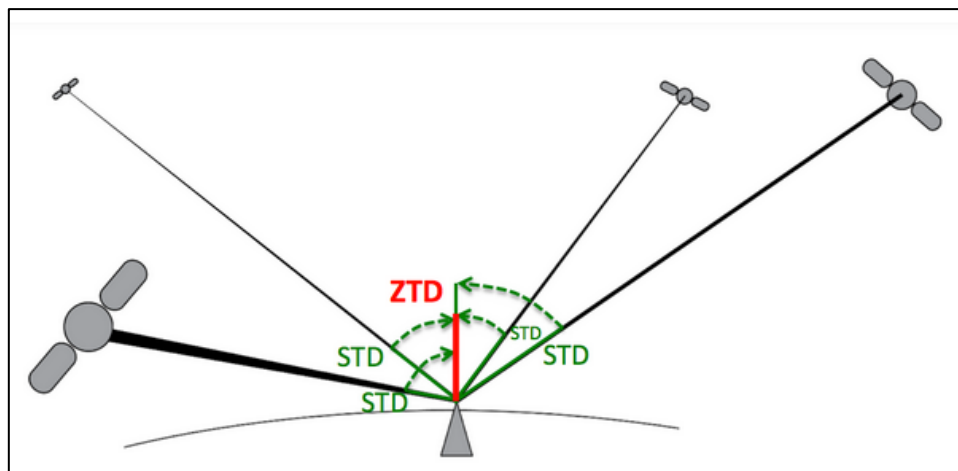


Figure 14 Zenithal troposphere delay modelling (Reguzzoni, 2012)

The slant tropospheric delay (STD) is often modeled as the product of the delay in the zenith direction and a zenith angle dependent mapping function. By neglecting the delay caused by the ray bending and assuming a horizontally layered atmosphere, where the refractivity N is only a function of height, the expression for the slant tropospheric delay (STD), derived from Equation 28 and Equation 29, is:

$$STD = 10^{-6} \int_0^{\infty} N \, ds = 10^{-6} \int_{r_0}^{\infty} N \frac{ds}{dr} \, dr$$

Equation 34: Slant tropospheric delay equation

Referring to Figure 15B:

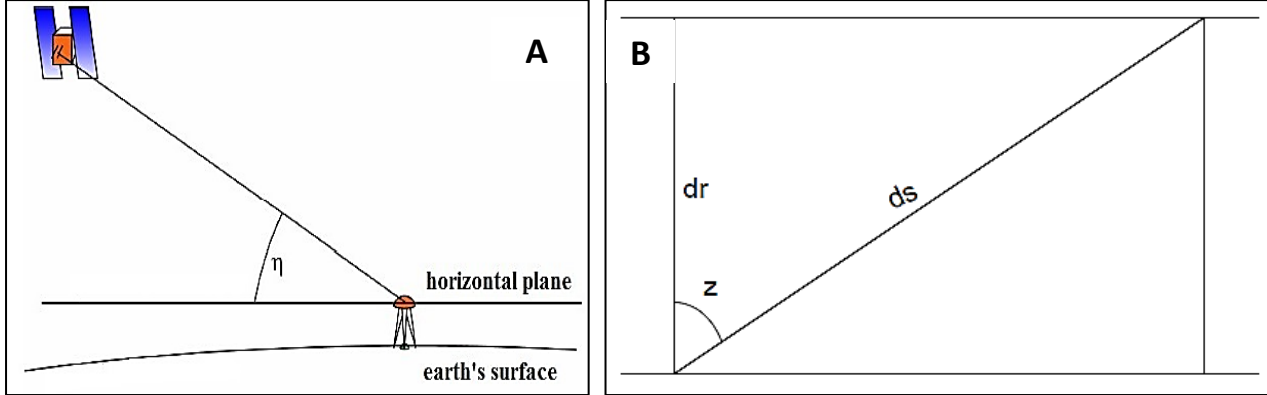


Figure 15 A) Elevation angle η **B)** Relation between radius difference dr , distance difference ds , and zenith angle z ($z=90^\circ - \eta$) (Kleijer, 2004)

for an infinitesimal thin layer the following relationship holds:

$$\frac{ds}{dr} = \frac{1}{\cos(z)} \equiv \sec(z)$$

Equation 35

where:

dr = difference in radius (distance to the center of the earth) of the two layers

z = zenith angle at an arbitrary layer

Because of the curvature of the atmosphere, this zenith angle changes along the ray (Kleijer, 2004). For this reason a function that allows to move from STD, slant tropospheric delay, to ZTD, zenith tropospheric delay, and vice versa is defined. It is called mapping function, mf , and the general relationship between STD and ZTD is:

$$STD(z) = ZTD \cdot mf(z)$$

Equation 36: ZTD and STD relation

Since the total tropospheric delay can be decomposed in a hydrostatic and wet part also the previous equation can be rewritten:

$$STD_{hydr}(z) + STD_{wet}(z) = ZTD \cdot (mf_{hydr}(z) + mf_{wet}(z))$$

Equation 37: STD hydrostatic and wet part relationship

where:

$mf_{hydr}(z)$ = hydrostatic mapping function

$mf_{wet}(z)$ = wet mapping function

The hydrostatic part, often known as the dry delay, follows the laws of ideal gases; the wet part is related to water vapor present in the troposphere. It is the more variable part and it is harder to model (Hopfield, 1969).

The dry part is responsible for a zenith delay of approximately 230 cm at sea level; the wet delay is responsible for up to 40 cm in the zenith direction (Leick, 2004).

The zenith delay can be modelled using the method of Saastamoinen (Saastamoinen, 1959) as given by Davis (Davis & Herrinch, 1985). The expressions are:

$$\text{Hydrostatic Zenith Delay [m]} = \frac{0,002277 \cdot p}{1 - 0,00266 \cdot \cos(2\phi) - 0,0028 \cdot 10^{-3} \cdot h}$$

$$\text{Wet Zenith Delay [m]} = \left(\frac{1255}{T} + 0,05 \right) \cdot \frac{0,002277 \cdot e}{1 - 0,00266 \cdot \cos(2\phi) - 0,0028 \cdot 10^{-3} \cdot h}$$

Equation 38: Hydrostatic and Wet zenith delays

where:

p = atmospheric pressure [mbar]

ϕ = latitude [rad]

h = height [km]

T = temperature [K]

e = partial pressure of water vapor [mbar]

The meteorological measurements required as inputs to the Saastamoinen model can be either obtained from local measurements made at the receiver, or if not available, from a global seasonal temperature and pressure model such as the Global Pressure and Temperature (GPT) model (Boehm, Heinkelmann, & Schuh, 2007).

There are many mapping functions to project the zenith delay to a delay at a given elevation angle. A commonly used example is the Niell Mapping Function (NMF) which uses a continued fraction with tabulated seasonal and latitude dependent coefficients (Niell, 1996). More recently the Vienna Mapping Functions 1 (VMF1) were produced by ray tracking numerical weather models such as the European Centre for Medium-Range Weather Forecasts (ECMWF) global weather model. The Global Mapping Function (GMF) is a spherical harmonic fit to seasonal average VMF1 parameters. Compared to the NMF, the GMF significantly reduces regional height biases and annual errors (Martin, 2013). It is used in the experiments presented in chapter 4.

For the Global Mapping function (Boehm et al., 2007) both the wet and dry mapping functions take the following form:

$$m(\eta) = \frac{1 + \frac{a}{1 + \frac{b}{1 + \frac{c}{\sin(\eta) + \frac{a}{\sin(\eta) + \frac{b}{\sin(\eta) + c}}}}}}{\sin(\eta) + \frac{a}{\sin(\eta) + \frac{b}{\sin(\eta) + c}}}$$

Equation 39: GMF general equation

The dry and wet mapping functions are formed from corresponding sets of parameters for a , b and c designated with indices h , for the hydrostatic part, and w , for the wet.

The precipitable water vapor (PWV) index is obtained starting from the Zenith Wet Delay (ZWD). A mathematical definition of ZWD is reported in Equation 40.

$$ZWD \doteq 10^6 \int_{h_0}^{\infty} N_w(h) dh$$

Equation 40: ZWD general expression

where:

$$N_w \doteq k'_2 \frac{e}{T} + k_3 \frac{e}{T^2}$$

$$k'_2 = \text{constant } \left[\frac{K}{\text{mbar}} \right]$$

$$k_3 = \text{constant } \left[\frac{K^2}{\text{mbar}} \right]$$

N_w = refractivity of water vapor [-]

e = partial pressure of water vapor $\left[\frac{N}{m^2} \right]$

T = temperature [K]

The PWV is obtained from:

$$PWV = k' \cdot ZWD$$

Equation 41: PWV

where:

$$k' = \frac{10^8}{\rho \cdot R_v \cdot \left(\frac{c_3}{T_m} + c'_2 - m \cdot c_1 \right)}$$

$$c_1 = 77,604 \pm 0,014 \left[\frac{K}{hPa} \right]$$

$$c'_2 = 17 \pm 10 \left[\frac{K}{hPa} \right]$$

$$c_3 = 10^5 \cdot (3,776 \pm 0,004) \left[\frac{K}{hPa} \right]$$

m = ratio of molar weight of water vapor to molar weight of dry air = 0,62198 [-]

$$\rho = \text{water density} = 998 \left[\frac{kg}{m^3} \right]$$

$$R_v = \text{specific gas constant for water vapor} = \frac{R \text{ (gas constant)}}{M_w \text{ (molecular weight of water vapor)}}$$

$$= \frac{8,314472 \cdot 10^3 \frac{J}{mol K}}{18,0153 \frac{kg}{mol}}$$

T_m = weighted mean temperature of the atmosphere (obtained by linear regression)[K]

Equation 41 can be approximated by:

$$PWV = \frac{ZWD}{6}$$

Equation 42: PWV approximated ($k'=1/6$)

This is valid only for a quick assessment. The dimensionless quantity k' varies spatially and temporally. Some authors have developed empirical formulas for its evaluation; some references are (Bevis et al., 1992), (Mendes, 1999) and (Emardson & Derk, 1998).

There is also another index called Integrated Water Vapor (IWV), that is used for meteorological applications. It's defined as:

$$IWV \doteq \int_{h_0}^{\infty} \rho_v dh$$

Equation 43: Integrated Water Vapor (IWV)

where:

h_0 = height above mean sea level

ρ_v = density of moist air $\left[\frac{kg}{m^3}\right]$

The use of this index requires approximate tables, not shown here.

3.1.1 Azimuthal asymmetry and gradient parameters

In the section above the atmosphere is considered to be horizontally layered and azimuthal symmetric. Although for most applications the previous model is appropriate, azimuthal asymmetry may introduce significant errors in geodetic measurements where high precision is required.

A way to model the asymmetry is to assume a tilted atmosphere. In a tilted atmosphere the refractivity N index is function of height and horizontal position. The azimuthal variations of tropospheric refraction is taken into account introducing tropospheric gradient parameters (Meindl, Schaer, Hugentobler, & Beutler, 2004).

The Bernese GPS software package offers the possibility to introduce such parameters, north and east gradient, using a model which corresponds to a tilting of the tropospheric mapping function.

Tilting the zenith direction in the mapping function is one possibility to represent tropospheric gradient. Using the so called tropospheric zenith direction, the direction with minimal tropospheric delay, results in a tropospheric zenith angle \tilde{z} which in general is different from the geometrical zenith distance z (Meindl et al., 2004). This is represented in Figure 16.

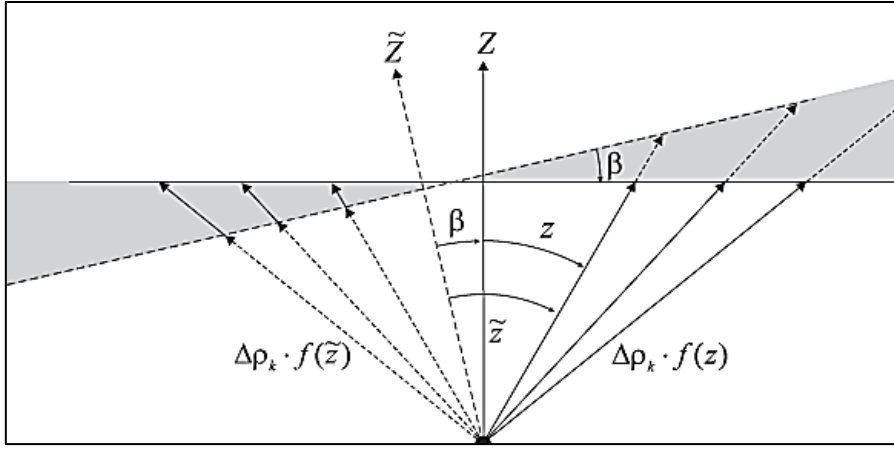


Figure 16: Tilting of the tropospheric zenith by angle β ; $\Delta\rho_k \cdot f(\tilde{z})$ is equivalent to STD (Meindl et al., 2004)

Introducing \tilde{z} as argument for the mapping functions, the slant tropospheric delay STD may be written as:

$$STD(t) = ZTD_{apr} \cdot mf_{apr}(\tilde{z}) + ZTD(t) \cdot mf(\tilde{z})$$

Equation 44

where:

ZTD_{apr} = tropospheric zenith delay according to an a – priori model

$mf_{apr}(\tilde{z})$ = mapping function of the a – priori model

$ZTD(t)$ = time dependent zenith troposphere parameter

$mf(\tilde{z})$ = mapping function used for the zenith parameter

Usually one does not have a priori information on the tropospheric zenith direction. This is why the geometrical zenith is used for the a-priori part of the above equation:

$$STD_R^S(t) = ZTD_{apr} \cdot mf_{apr}(z) + ZTD(t) \cdot mf(\tilde{z})$$

Equation 45

Assuming that an angle β between the tropospheric and the geometrical zenith is small, the two directions can be related to each other by:

$$\tilde{z} = z + \delta z = z + x \cdot \cos(A) + y \cdot \sin(A)$$

Equation 46

where:

x, y = station dependent parameters

A = azimuth of the direction station – satellite

By substituting Equation 46 in the mapping function used for the zenith parameter:

$$ZTD(t) \cdot mf(\tilde{z}) = ZTD(t) \cdot mf(z + \delta z) = ZTD(t) \cdot mf(z + x \cdot \cos(A) + y \cdot \sin(A))$$

Equation 47

Expanding this equation in a Taylor series and truncating the series after first order terms yields:

$$ZTD(t) \cdot mf(\tilde{z}) = ZTD(t) \cdot mf(z) + ZTD(t) \cdot \frac{\partial mf}{\partial z} \cdot x \cdot \cos(A) + ZTD(t) \cdot \frac{\partial mf}{\partial z} \cdot y \cdot \sin(A)$$

Equation 48

Introducing Equation 48 in Equation 45 the final expression becomes:

$$\begin{aligned} STD(t) = ZTD_{apr} \cdot mf_{apr}(z) &+ ZTD^h(t) \cdot mf(z) + ZTD^n(t) \cdot \frac{\partial mf}{\partial z} \cdot \cos(A) + \\ &+ ZTD^e(t) \cdot \frac{\partial mf}{\partial z} \cdot \sin(A) \end{aligned}$$

Equation 49

where:

$ZTD^h(t) = ZTD(t) = \text{zenith delay parameter}$

$ZTD^n(t) = ZTD(t) \cdot x = \text{gradient parameter in north - south direction}$

$ZTD^e(t) = ZTD(t) \cdot y = \text{gradient parameter in east - west direction}$

These terms have to be set up and estimated in the GPS analysis.

3.2 Precise Point Positioning

Precise Point Positioning (PPP) has become more and more popular in recent years. The method as described in (Zumberge, Heflin, Jefferson, Watkins, & Webb, 1997) makes it possible to process large networks and is also useful for GPS users with a single receiver.

The concept of PPP was first introduced in the 1970's by R.R. Anderle, and was characterized as a single station positioning with fixed precise orbit solutions and Doppler satellite observations (Kouba & Heroux, 2001).

This technique allows centimeter-level accuracy to be achieved for static positioning and decimeter level, or better, for kinematic positioning (Jaume, José Miguel Juan, & Manuel, 2013).

It requires the knowledge of the satellite precise clock and orbit corrections. Parameters left to estimate are station clock corrections, coordinates, troposphere parameters and initial phase ambiguities.

The main characteristics are:

- PPP is not a differential technique; the geodetic datum must not be defined by means of any constraint on reference stations;
- Consistency between introduced orbit, earth orientation parameters and satellite clock information is required in order to reach high accuracy.

Since it is not a differential technique no correlation between stations is introduced and is not needed, as well, the acquisition of simultaneous tracking data from a reference station. Moreover, omitting the processing phase devoted to the baseline building reduces the required processing time compared to the network solution.

However, a lot of effects, reduced in the double difference method, have to be treated carefully.

The PPP observation equation is based on the ionospheric-free combination, Equation 13 which is used to eliminate the ionospheric delay term but other error sources has to be taken into account. They can be grouped under *Satellite Attitude*, *Receiver Specific Corrections* and *Signal Propagation Errors* (Kouba & Heroux, 2001).

Using the ionospheric-free combination the category *Signal Propagation Errors* is, essentially, composed by the tropospheric delay, described in 3.1.

The category *Satellite Attitude* consists of the following effects:

- Satellite antenna phase center offset and variation
- Phase wind-up
- Relativistic effects

The correction for satellite antenna phase center offset and variation is necessary in order to relate the satellite center of mass coordinates and the satellite antenna coordinates, that represents the starting point of the signals. The precise ephemeris provides the satellite coordinates referred to its mass center, while the geometrical distance between satellite and receiver is referred to their antenna phase centers. The distance between the satellite antenna phase center and its center of mass should be known, otherwise an error may occur (Chatzinikos, Fotiou, & Pikridas, 2009). For each satellites are available the antenna phase center offset and variation. These informations are accounted for in the calculation by introducing the so called ANTEX file. The detailed description can be found on the IGS website (<https://igscb.jpl.nasa.gov/igscb/station/general/antex14.txt>).

The phase wind-up effect impacts on the carrier phase measurements due to the change in the relative orientation between the transmitting and the receiving antennas. It is composed of two parts: the geometric part and satellite attitude (*Bernese GPS Software version 5.0, user manual*, 2007). The second part is fully absorbed by the satellite clocks corrections. The first is corrected including the nominal attitude motion of the satellites. This correction is particularly important for the PPP. The final clocks generates at the Center for Orbit Determination in Europe (CODE) in the operational series includes the geometrical part of the phase clocks since September 14th, 2003 (Day of Year 257 of 2003) and the full effect since November 5th, 2006 (Day of Year 309 of 2006).

The relativistic effects affect the time transfer between satellite and ground receivers. They are linked to the concept of General and Special Relativity, to the Sagnac effect and to the so called Shapiro effect. Since the purpose of this work is another, these effects are only mentioned. Details about them can be found in (Ashby, 2003). These effects are taken into account in the receiver software.

The category *Receiver Specific Corrections* consists essentially of site displacements effects. These are related to the Earth's crust deformation caused by:

- Solid earth tides
- Ocean loading
- Atmospheric loading

All of these effects have to be taken into account to achieve the higher precision and accuracy during the PPP adjustment. For example neglecting the solid earth tides this induces a systematic position errors of up to 12,5 cm in the radial direction and 5 cm in the north direction (Kouba & Heroux, 2001).

These systematic effects have their own models whose parameters can be obtained outside, via a web service, or inside, through a special sub-routine, the Bernese GPS Software. Since the purpose of this thesis is the estimation of the total zenith delay these effects and their related model are not discussed in detail; only general information are given here.

The solid Earth is pliable enough to respond to the gravitational forces caused by the Moon and Sun. The periodic vertical and horizontal site displacements are represented by a spherical harmonic expansion scaled by two numbers namely *Love* and *Shida* numbers (Kouba & Heroux, 2001). The total displacement is the sum of the displacement induced by the Moon and the

displacement induced by the Sun. In the Bernese GPS Software the model proposed by IERS is implemented (*Bernese GPS Software version 5.0, user manual*, 2007).

The change in mass distribution induced by the ocean tides is another cause of site displacement due to the crustal deformation. Its effect is more localized near the coast lines and can induce deformations in the vertical component up to 30 mm (Schuh & Estermann, 2002). The Bernese GPS Software requires the loading coefficients, relative to the processed stations, obtained from a free service available at (<http://holt.oso.chalmers.se/loading/>). A file with BLQ extension is produced and used in the software.

Similarly to the ocean loading, in the case of the atmosphere loading a site displacement is caused by the variation of the atmospheric pressure with respect to reference pressure. This variation implies a response of the Earth's surface. This effect could induce an error up to 18 mm in the vertical component (Tregoning & van Dam, 2005). In the Bernese GPS software a model to handle this effect is implemented. The sub-routine *GRDS1S2* generates a file with ATL extension that contains the needed coefficients.

Also the tectonic plate motion has to be taken into account. This effect is not included in the *Receiver Specific Corrections* since it is considered also in a double difference adjustment. During the analysis, the propagation of station coordinates at a reference epoch is a common practice and it is performed considering the plate to which a station belongs.

3.2.1 Parameter estimation in the Bernese GPS Software

The estimation of the unknown parameters is based on a linearized version of the ionospheric-free observation equation.

The linearized term is the geometric distance between satellite and receiver. It takes this form:

$$\rho_R^S(t)^{lin.} = \frac{\tilde{X}_R - \tilde{X}^S(t)}{\tilde{\rho}_R^S(t)} \cdot (X_R(t) - \tilde{X}_R) + \frac{\tilde{Y}_R - \tilde{Y}^S(t)}{\tilde{\rho}_R^S(t)} \cdot (Y_R(t) - \tilde{Y}_R) + \frac{\tilde{Z}_R - \tilde{Z}^S(t)}{\tilde{\rho}_R^S(t)} \cdot (Z_R(t) - \tilde{Z}_R) + \tilde{\rho}_R^S(t)$$

Equation 50: Linearised geometric distance

where:

$$\tilde{\rho}_R^S(t) = \text{approximate geometric distance} = \sqrt{(\tilde{X}_R - \tilde{X}^S)^2 + (\tilde{Y}_R - \tilde{Y}^S)^2 + (\tilde{Z}_R - \tilde{Z}^S)^2}$$

$\tilde{X}_R, \tilde{Y}_R, \tilde{Z}_R$ = *a priori* receiver coordinates

X_R, Y_R, Z_R = receiver coordinates to be estimated

$\tilde{X}^S, \tilde{Y}^S, \tilde{Z}^S$ = satellite coordinates, assumed known

The a priori receiver coordinates, at the first step, are obtained from the RINEX observation files. Then some iterative procedures are necessary to improve the final estimation.

In the Bernese GPS Software a *Gauss-Markoff* model is implemented. Its general form is:

$$E(y) = A \cdot p$$

$$D(y) = \sigma^2 \cdot P^{-1}$$

Equation 51: Gauss-Markov model

Indicating with n the number of observations and u the number of unknowns the equations terms are:

$A_{n \times u}$ = matrix of coefficients, or design matrix

$p_{u \times 1}$ = vector of unknowns

$y_{n \times 1}$ = vector of observations

$P_{n \times n}$ = positive defined weight matrix

$E(\cdot)$ = operator of expectation

$D(\cdot)$ = operator of dispersion

σ^2 = variance of unit weight

The solving formula is:

$$\frac{d\Omega(p)}{dp} = 0$$

$$\Omega(p) = \frac{1}{\sigma^2} (y - Ap)^t P (y - Ap)$$

that corresponds to find a minimum values for the target function $\Omega(p)$. This permits to write the so called normal equations:

$$N\hat{p} = A^t Py$$

where:

$$N = A^t PA = \text{normal matrix}$$

The vector of unknowns is obtained from:

$$\hat{p} = (N)^{-1} A^t Py$$

Then, it is possible to compute:

$$D(\hat{p}) = \hat{\sigma}^2 (N)^{-1} = \text{parameter covariance matrix}$$

$$\hat{v} = A\hat{p} - y = \text{vector of residuals}$$

$$\hat{\sigma}^2 = \frac{y^t Py - y^t PA\hat{p}}{n - u} = \text{a posteriori variance of unit weight}$$

This model can suffer numerical instability in the inversion process of the normal matrix N . This problem arises in the PPP adjustment and it is caused, basically, by the satellites geometry (Figure 17). This brings rows and columns linearly dependent and so the normal matrix is not full rank and not invertible.

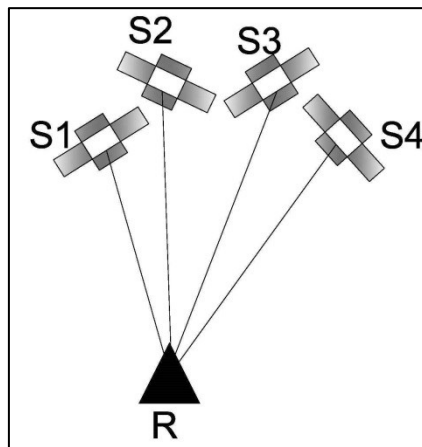


Figure 17: Poor satellite configuration

Only introducing pseudo-observations, constraints or regularization conditions this problem can be overcome.

In this case the system becomes:

$$(N + H^t P_h H) \hat{p} = A^t P y + H^t P_h h$$

Indicating with $r < u$ the number of constraining equations the above system terms are:

$H_{r \cdot u}$ = matrix with given coefficients of rank equal to r

$P_{h,r \cdot r}$ = dispersion matrix of the introduced constraining equations

The constraint equation is of the following form:

$$H p = h + \nu_h$$

$$D(h) = \sigma^2 P_h^{-1}$$

Constraints may be introduced for:

- Coordinates
- Velocities
- Kinematic coordinates
- Troposphere
- Global ionosphere models
- Stochastic ionosphere parameters
- Differential code biases
- Orbit
- Geocenter coordinates
- Earth orientation parameters
- Receiver and satellite antenna offsets and patterns

The constraints can be:

- Absolute
- Relative
- With a zero mean

The first type is used for station coordinates, the second for troposphere zenith delay and gradient parameters and the last for realizing an ensemble of reference clocks.

In chapter 4, in particular some experiments are based on varying the so called *Relative a priori sigma parameter*, thus introducing a regularization condition. It is needed to set the constraint condition in the equation reported above.

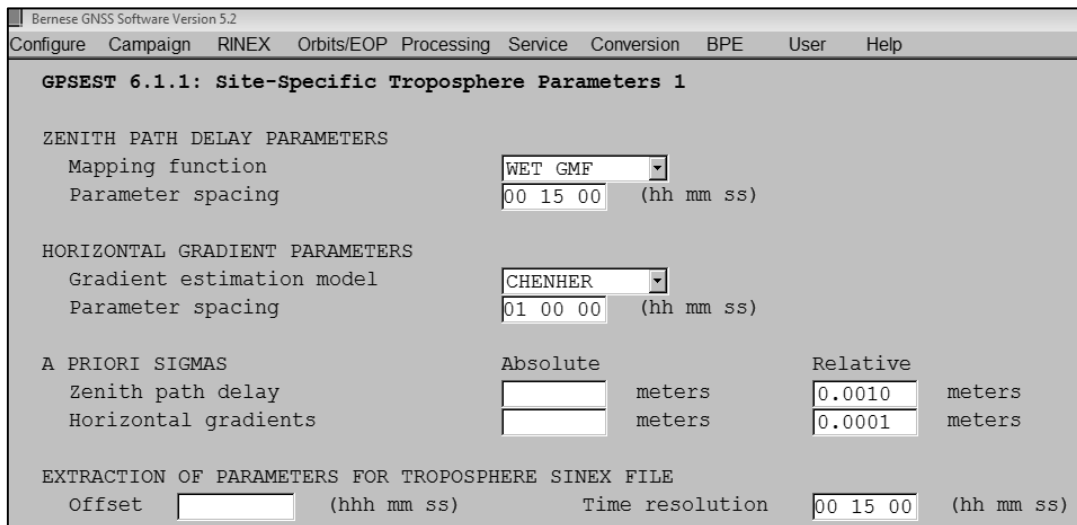


Figure 18: BSW screenshot about the so called *Relative a priori sigma parameter*

4 Experiments and results

In this chapter the different experiments made and the results obtained during the thesis are analyzed. Some of the experiments have been carried out with the aim of understanding how the Bernese PPP works; some others to assess the quality of the resulting zenith delays in comparison with different adjustment strategies.

4.1 Case study data

Two different datasets are used. For all of the next experiments some statistics are reported. In particular the rms (root mean square) latitude and longitude errors are reported both in the original measurement unit, seconds, and in metric term. This last is obtained using the formula in Equation 52.

$$RMS [m] = \frac{RMS [sec]}{3600} \cdot \frac{\pi}{180} \cdot R$$

$$R = \text{earth radius} = 6371005,076123 \text{ m}$$

Equation 52: RMS conversion from [sec] to [m]

Pearson's linear correlation coefficient is also reported and it is indicated as *correlation index*.

4.1.1 Mist dataset

The first one, MisT (Misure Troposferiche) data, was collected from a network of nine GNSS stations located in Lombardy region in the neighborhood of Como. It is used to evaluate the results of a PPP adjustment performed by the *Bernese5.2 Software* both in terms of coordinates and troposphere delays parameters by comparison with the results obtained from a Double Difference adjustment of the same data with *Bernese 5.0 Software*. To assess the PPP results, two stations of this network are used. They are Como and Dani stations, placed at a distance of about 9 km one from the other; the processed data cover seven days, from October 26th, 2008 to November 1th, 2008.

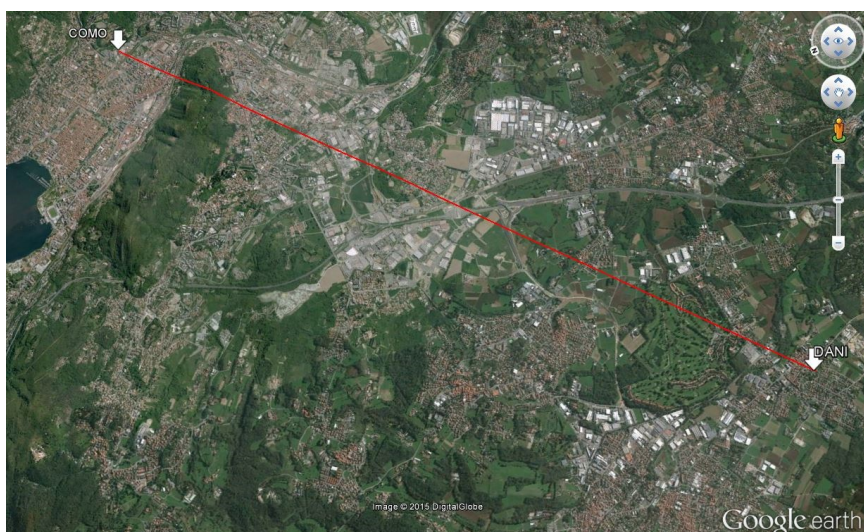


Figure 19: Como and Dani stations (inter-distance of 9.14km - red line)

The period of operation of this network includes about half a year, from about May to November of 2008. The antenna and the receivers are the same for all stations, apart from Como one, which is part of the European Permanent Network. This station was used as reference in the MisT network adjustment. Its tropospheric zenith delay is assumed to be fixed in order to perform the double difference processing technique. This reference value was obtained from a regional network adjustment, in particular the GPSLombardia network was used. This network is composed by 16 permanent stations located in Lombardy. Moreover the GPSLombardia network adjustment is performed by including some stations of the International GNSS Service (IGS). These IGS stations are located in Cagliari, Grasse, Graz, Matera, Medicina, Padova, Wettzell and Zimmerwald (Reguzzoni, 2012).

4.1.2 Uji dataset

The second dataset, UJI data, was collected from a network of fifteen GNSS stations located in Japan in the Kyoto district. This local network was designed, installed and operated by the Laboratory of Atmospheric Sensing and Diagnosis (Tsuda laboratory) of the Research Institute for Sustainable Humanosphere (<http://www.rish.kyoto-u.ac.jp/English/>) (Reguzzoni, 2012). As for the MisT data, the scope is to evaluate the results of *Bernese Precise Point Positioning*, in comparison with a precise point positioning solution obtained from another software called *RTNet*. This is considered as reference solution as it is in agreement with the precipitable water vapor (PWV) obtained by independent radiosondes and radiometer (Realini, Tsuda, Sato, Oigawa, & Iwaki, 2012). The processed data refer only to July 26th, 2012.

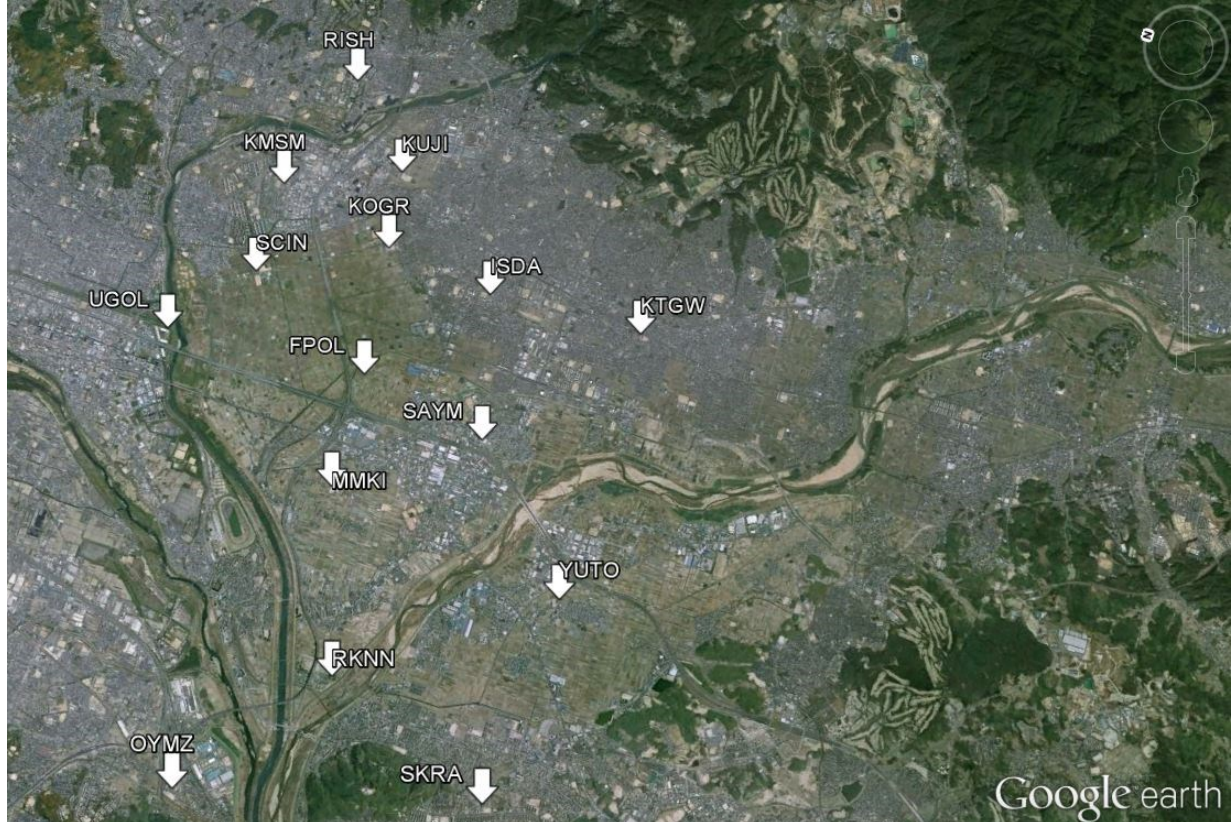


Figure 20: UJI Network, the dense network of 15 stations covered an area of 67km² with a maximum inter-distance of about 10km

4.2 MisT data processing

In this section the results of MisT data processing are reported. Nine different adjustments were performed each referred to with a different campaign name. For each campaign in Table 3 the total zenith delay estimation rate and the troposphere modeling adopted are reported. The models are or isotropic, no gradient applied, or anisotropic, with gradients applied.

Campaign name	Gradient model	ZTD Estimation rate
MIST_5	Applied (CHENHER model)	15 min
MIST_5B	Not applied	15 min
MIST_6	Applied (CHENHER model)	30 min
MIST_6B	Not applied	30 min
MIST_7	Applied (CHENHER model)	60 min
MIST_7B	Not applied	60 min
MIST_11	Not applied	60 min
MIST_12	Not applied	60 min
MIST_13	Not applied	60 min
MIST_18	Not applied	60 min

Table 3: Settings for the estimation in the different campaigns

4.2.1 Effect of troposphere anisotropic model and estimation rate

In Table 4 the sample size for Como and Dani stations is reported.

Campaign name	Sample size for COMO station	Sample size for DANI station
MIST_5	97	97
MIST_5B	97	97
MIST_6	49	49
MIST_6B	49	49
MIST_7	24	24
MIST_7B	24	24

Table 4: Sample size for Como and Dani stations in the different campaigns

In the first experiment the effect of the troposphere anisotropic model is evaluated. The MisT data of October 26th, 2008 were processed with and without the gradients estimation, MIST_5 and MIST_5B campaigns respectively.

The troposphere parameters are estimated every 15 minutes.

In Table 5 and Table 6 coordinate results for Como and Dani stations are shown.

MIST_5

HEIGHT [m]	292,281	With rms error [m]	0,0008	
LATITUDE	45°48'7,789"	With rms error	0,0002 sec	0,006 m
LONGITUDE	9°5'44,244"	With rms error	0,0005 sec	0,015 m

MIST_5B

HEIGHT [m]	292,282	With rms error [m]	0,0004	
LATITUDE	45°48'7,789"	With rms error	0,0001 sec	0,003 m
LONGITUDE	9°5'44,244"	With rms error	0,0002 sec	0,006 m

Table 5: Mist_5 (with gradient estimation) and Mist_5B (without gradient estimation) coordinate for Como station

MIST_5

HEIGHT [m]	373,029	With rms error [m]	0,0014	
LATITUDE	45°44'50,23"	With rms error	0,0005 sec	0,015 m
LONGITUDE	9°0'30,643"	With rms error	0,0009 sec	0,028 m

MIST_5B

HEIGHT [m]	373,028	With rms error [m]	0,0006	
LATITUDE	45°44'50,23"	With rms error	0,0002 sec	0,006 m
LONGITUDE	9°0'30,643"	With rms error	0,0004 sec	0,012 m

Table 6: Mist_5 (with gradient estimation) and Mist_5B (without gradient estimation) coordinate for Dani station

For what concerns the total zenith delay estimation, some statistics are reported in Table 7 and Table 8, a graphical representation is in Figure 21 and Figure 22.

	MIST_5	MIST_5B	MIST_5 vs MIST_5B	
min [m]	2,361	2,358	correlation index	99,581%
max [m]	2,394	2,395	max difference [m]	0,003
mean [m]	2,372	2,371	min difference [m]	-0,001
std [m]	0,009	0,010		

MIST_5 minus MIST_5B

mean [m]	0,0010
std [m]	0,0012

Table 7: Mist_5 (with gradient estimation) and Mist_5B (without gradient estimation) total zenith delay statistics estimation for Como station

	MIST_5	MIST_5B	MIST_5 vs MIST_5B	
min [m]	2,33	2,328	correlation index	99,531%
max [m]	2,366	2,372	max difference [m]	0,003
mean [m]	2,344	2,343	min difference [m]	-0,006
std [m]	0,009	0,01		

MIST_5 minus MIST_5B

mean [m]	0,0000
std [m]	0,0016

Table 8: Mist_5 (with gradient estimation) and Mist_5B (without gradient estimation) total zenith delay statistics estimation for Dani station

The estimates of total zenith delay parameter are statistically equivalent.

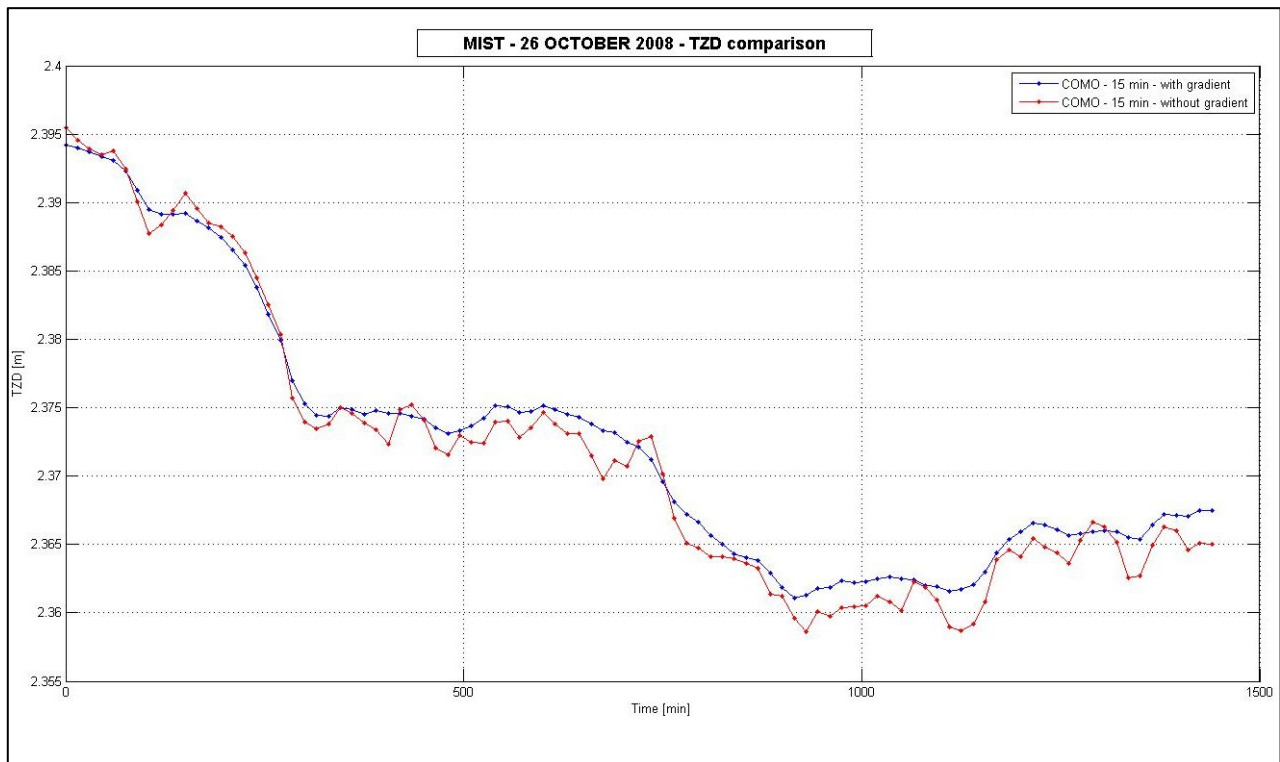


Figure 21: Total zenith delay for Como station, 26th October 2008

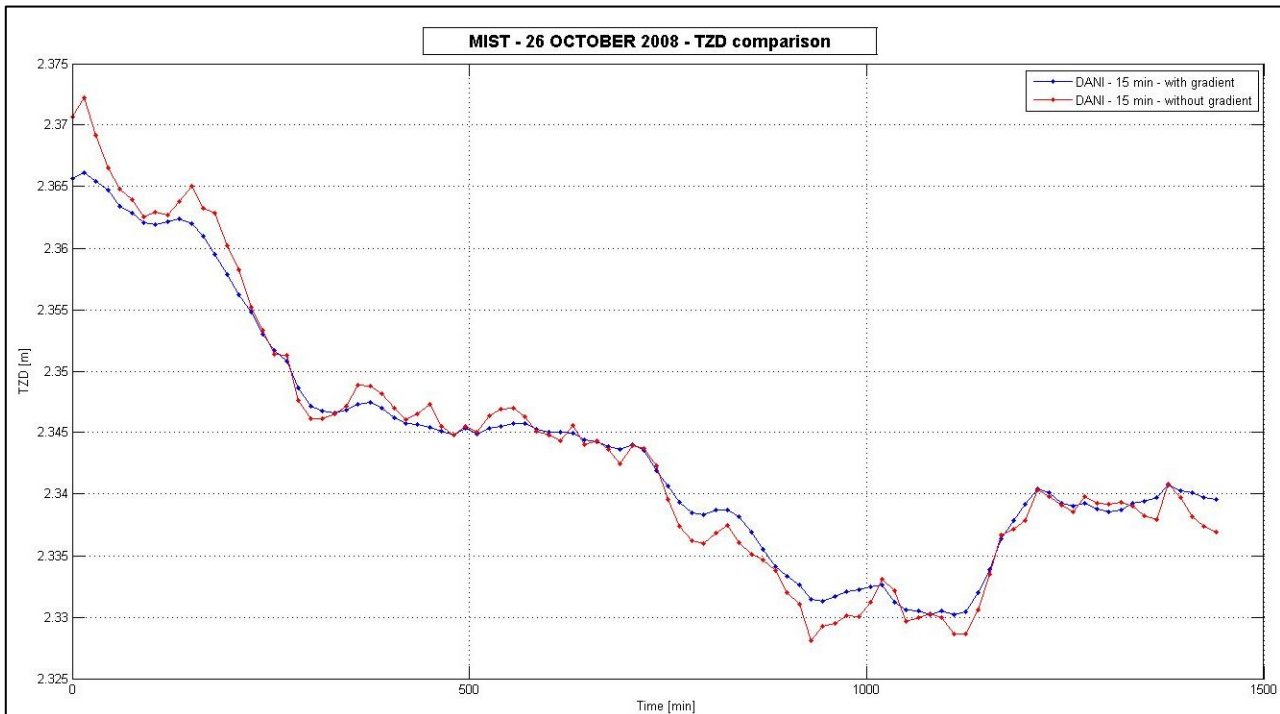


Figure 22: Total zenith delay for Dani station, 26th October 2008

The same trend is evident but in the case of gradient estimation the estimated TZD is smoother.

In the second set of campaigns, namely MIST_6 and MIST_6B, differs from the previous MIST_5 and MIST_5B only for troposphere parameters estimation rate, that here is equal to 30 minutes. In Table 9 and Table 10 the estimated coordinates of Como and Dani station are shown.

MIST_6

HEIGHT [m]	292,281	With rms error [m]	0,0004	
LATITUDE	45°48'7,789"	With rms error	0,0001 sec	0,0031 m
LONGITUDE	9°5'44,244"	With rms error	0,0002 sec	0,0062 m

MIST_6B

HEIGHT [m]	292,282	With rms error [m]	0,0003	
LATITUDE	45°48'7,789"	With rms error	0,0001 sec	0,0031 m
LONGITUDE	9°5'44,244"	With rms error	0,0002 sec	0,0062 m

Table 9: Mist_6 (with gradient estimation) and Mist_6B (without gradient estimation) coordinate for Como station

MIST_6

HEIGHT [m]	373,023	With rms error [m]	0,0007	
LATITUDE	45°44'50,23"	With rms error	0,0002 sec	0,0062 m
LONGITUDE	9°0'30,643"	With rms error	0,0004 sec	0,0124 m

MIST_6B

HEIGHT [m]	373,028	With rms error [m]	0,0006	
LATITUDE	45°44'50,230"	With rms error	0,0002 sec	0,0062 m
LONGITUDE	9°0'30,643"	With rms error	0,0004 sec	0,0124 m

Table 10: Mist_6 (with gradient estimation) and Mist_6B (without gradient estimation) coordinate for Dani station

The statistics of the estimated total zenith delays are reported in Table 11 and Table 12. A representation of the obtained TZD time series is given in Figure 23 and Figure 24.

	MIST_6	MIST_6B	MIST_6 vs MIST_6B	
min [m]	2,36	2,359	correlation index	99,647%
max [m]	2,393	2,395	max difference [m]	0,003
mean [m]	2,372	2,371	min difference [m]	-0,001
std [m]	0,009	0,01		

MIST_6 minus MIST_6B

mean [m]	0,0011
std [m]	0,0011

Table 11: Mist_6 (with gradient estimation) and Mist_6B (without gradient estimation) total zenith delay statistics estimation for Como station

	MIST_6	MIST_6B	MIST_6 vs MIST_6B	
min [m]	2,329	2,329	correlation index	99,773%
max [m]	2,367	2,371	max difference [m]	0,0008
mean [m]	2,345	2,344	min difference [m]	-0,0035
std [m]	0,01	0,01		

MIST_6 minus MIST_6B

mean [m]	-0,0005
std [m]	0,0009

Table 12: Mist_6 (with gradient estimation) and Mist_6B (without gradient estimation) total zenith delay statistics estimation for Dani station

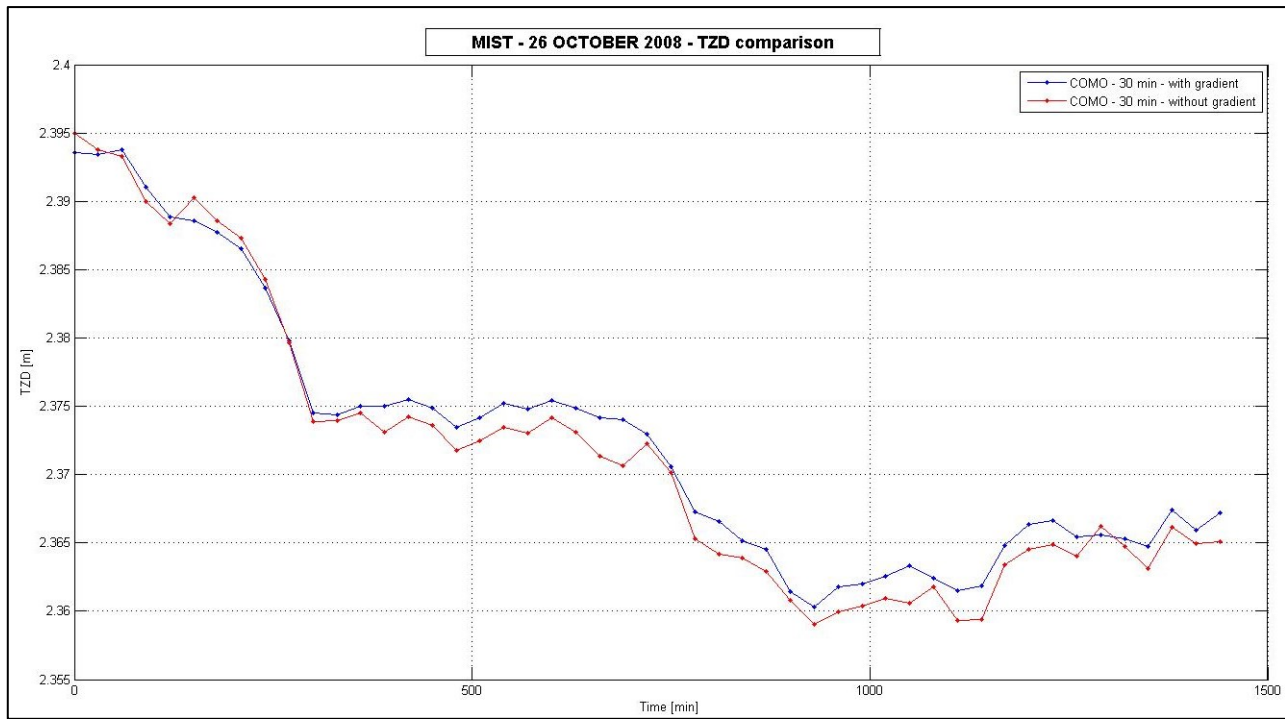


Figure 23: Total zenith delay for Como station, 26th October 2008

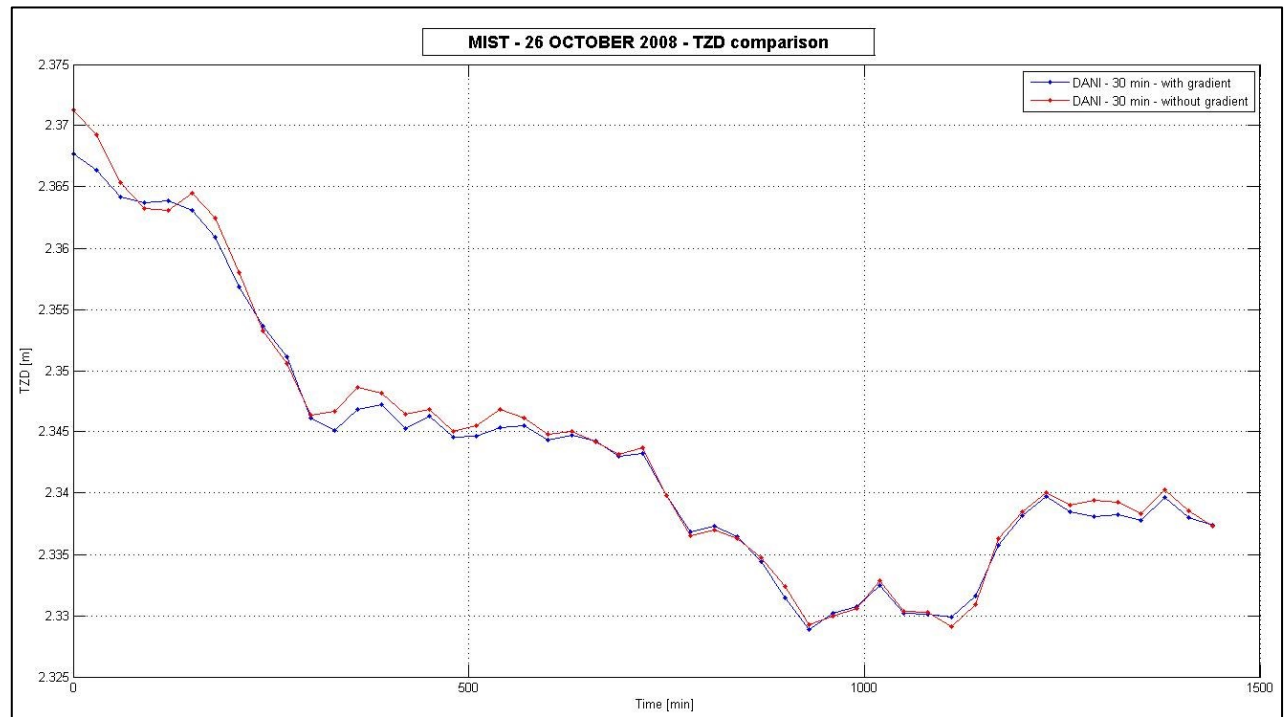


Figure 24: Total zenith delay for Dani station, 26th October 2008

As for the previous set it is noticeable the same trend for the two solutions. In this case the smoothing effect for the gradient model is less evident due to the rate of estimation.

In the third set of campaigns, namely MIST_7 and MIST_7B, the total zenith delay estimation rate is 60 minutes, the evaluation was done only for October 26th, 2008. In Table 13 and Table 14 resulting coordinates for Como and Dani station are shown.

MIST_7

HEIGHT [m]	292,281	With rms error [m]	0,0003	
LATITUDE	45°48'7,789"	With rms error	0,0001 sec	0,0031 m
LONGITUDE	9°5'44,244"	With rms error	0,0002 sec	0,0062 m

MIST_7B

HEIGHT [m]	292,282	With rms error [m]	0,0003	
LATITUDE	45°48'7,789"	With rms error	0,0001 sec	0,0031 m
LONGITUDE	9°5'44,244"	With rms error	0,0002 sec	0,0062 m

Table 13: Mist_7 (with gradient estimation) and Mist_7B (without gradient estimation) total zenith delay statistics estimation for Como station

MIST_7

HEIGHT [m]	373,029	With rms error [m]	0,0006	
LATITUDE	45°44'50,23"	With rms error	0,0002 sec	0,0062 m
LONGITUDE	9°0'30,643"	With rms error	0,0004 sec	0,0124 m

MIST_7B

HEIGHT [m]	373,028	With rms error [m]	0,0006	
LATITUDE	45°44'50,230"	With rms error	0,0002 sec	0,0062 m
LONGITUDE	9°0'30,643"	With rms error	0,0004 sec	0,0124 m

Table 14: Mist_6 (with gradient estimation) and Mist_6B (without gradient estimation) total zenith delay statistics estimation for Dani station

In Table 15 and Table 16 the troposphere result are reported and a representation is in Figure 25 and Figure 26.

	MIST_7	MIST_7B	MIST_7 vs MIST_7B	
min [m]	2,362	2,36	correlation index	99,799%
max [m]	2,393	2,395	max difference [m]	0,0029
mean [m]	2,373	2,372	min difference [m]	-0,001
std [m]	0,009	0,01		

MIST_7 minus MIST_7B

mean [m]	0,0011
std [m]	0,0010

Table 15: Mist_7 (with gradient estimation) and Mist_7B (without gradient estimation) total zenith delay statistics estimation for Como station

	MIST_7	MIST_7B	MIST_7 vs MIST_7B	
min [m]	2,33	2,33	correlation index	99,827%
max [m]	2,367	2,37	max difference [m]	0,0005
mean [m]	2,344	2,344	min difference [m]	-0,003
std [m]	0,01	0,01		

MIST_7 minus MIST_7B

mean [m]	-0,0005
std [m]	0,0008

Table 16: Mist_7 (with gradient estimation) and Mist_7B (without gradient estimation) total zenith delay statistics estimation for Dani station

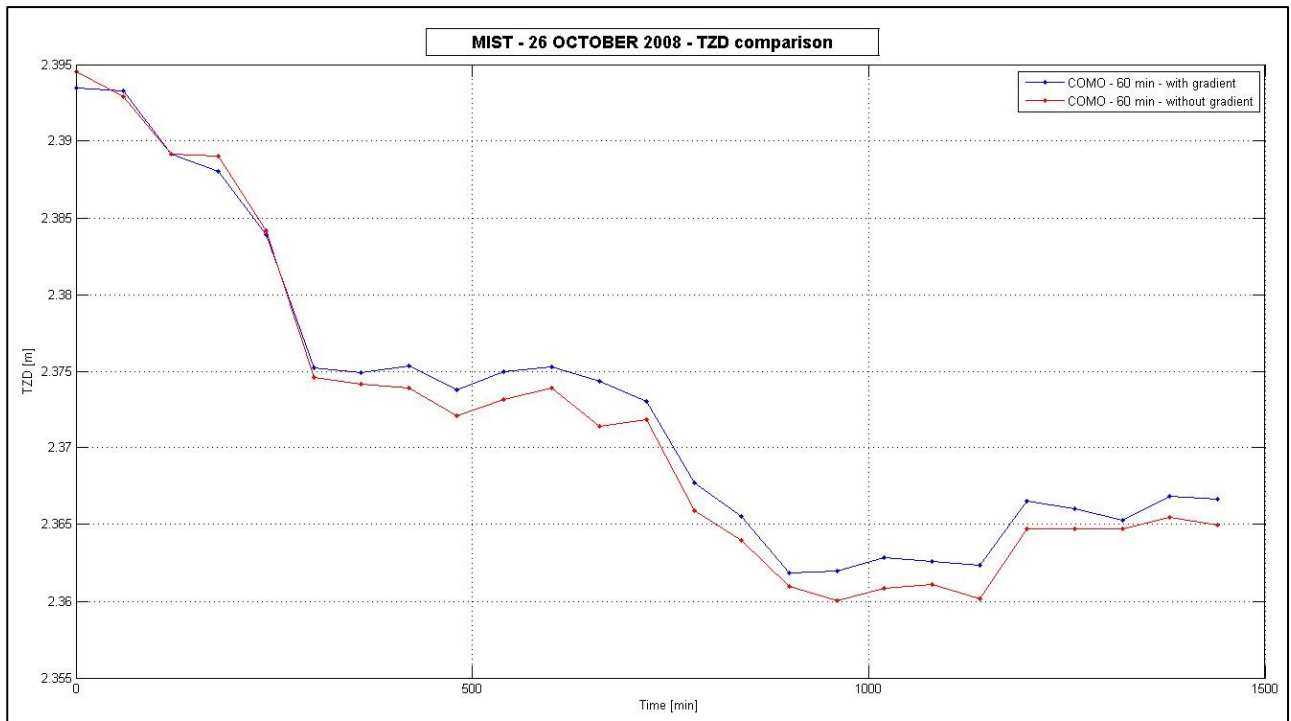


Figure 25: Total zenith delay for Como station, 26th October 2008

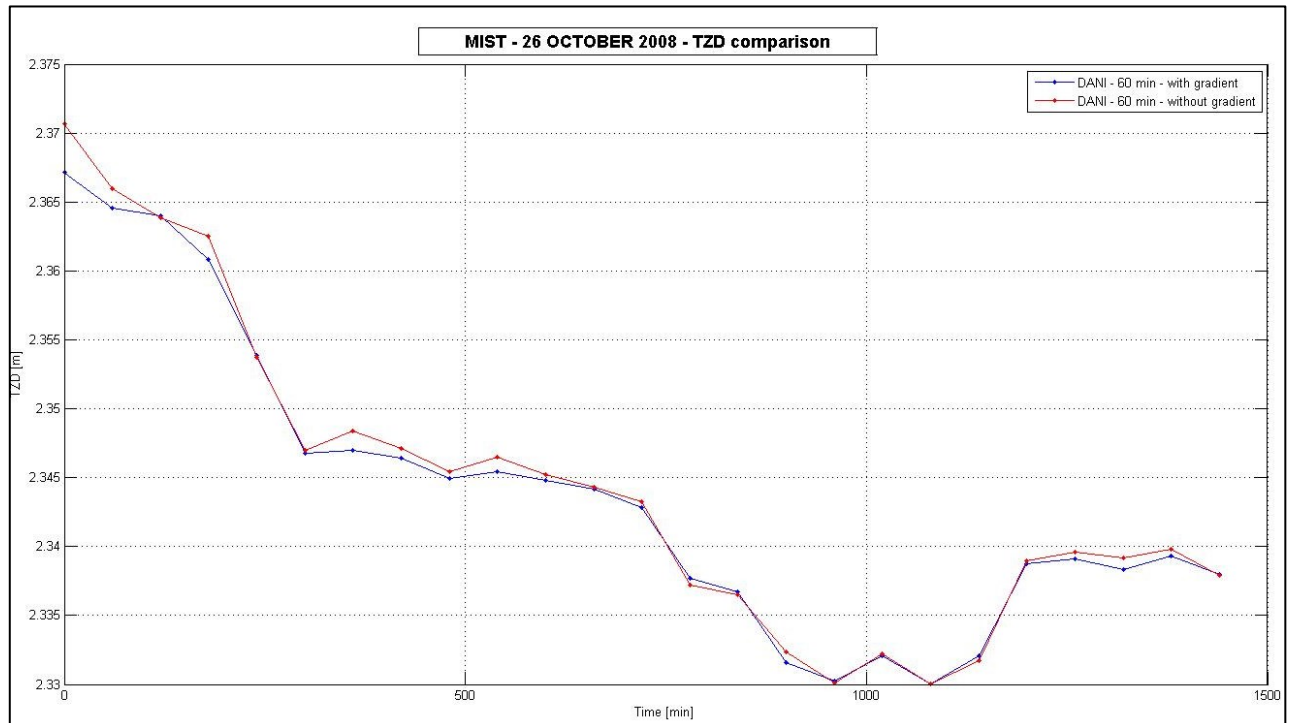


Figure 26: Total zenith delay for Dani station, 26th October 2008

4.2.2 Weekly estimation for Mist data

In this section the results obtained from the analysis of the data collocated from October 26th, 2008 to November 1th, 2008 are reported. The results of the Precise Point Positioning adjustment are compared with those of the Double Difference (DD) adjustment for the Como and the Dani stations. Since the Como station is part of EUREF Permanent Network also this third solution is compared in terms of tropospheric delay. The total zenith delay of the Como station are also compared with the ZTD time series provided by EUREF. These are obtained from a general adjustment of the European Permanent Network (EPN) to which the Como station belongs.

These products can be downloaded from http://igs.bkg.bund.de/root_ftp/EUREF/products/1503/. It is important to note that they are obtained with different procedure and settings. The troposphere parameters are estimated at a rate of 1h starting from half past midnight. The ASI (*Agenzia Spaziale Italiana*) products are obtained using the Niell Mapping Function and an elevation cutoff angle of 15°; the estimation is performed with *Microcosm* (<http://www.vmsi-microcosm.com/index.html>) operating in double difference. Further details can be found in (Ferraro & Nardi, 1996). For what concerns the BEK (*Bayerische Kommission fuer die Int. Erdmessung*) products, the elevation cutoff angle is set to 3° and also a Niell Mapping Function is used. In this case the used software is *Bernese GPS Software 5.0*. The last product is, called EUR (*Weekly combination of trop estimates of EUREF Analysis Centers*), a combination of different solutions. Details about these can be found in http://igs.bkg.bund.de/root_ftp/EUREF/products/1503/eur15037.tsu.Z.

An elevation cutoff angle of 10° is chosen for the precise point positioning elaboration. The gradient model is not estimated. Imposed these settings now makes sense to vary a parameter called *Relative a priori sigma for zenith path delay*, according to Bernese software notation.

In Table 17 the coordinates of Como and Dani station according to a double differences process are reported.

STATION	HEIGHT [m]	LATITUDE	LONGITUDE
COMO	292,294	45°48'7,789	9°5'44,243
DANI	373,036	45°44'50,23	9°0'30,643

Table 17: Como and Dani station coordinates from DD processing

In Table 18 the sample size is reported for Como and Dani stations for each campaign and adjustment process.

Campaign name	Sample size for COMO station		Sample size for DANI station	
	PPP [#]	DD [#]	PPP [#]	DD [#]
MIST_11	169	169	165	169
MIST_12	169	169	165	169
MIST_13	169	169	165	169

Table 18: Sample size for Como and Dani stations in the different campaigns and processing techniques (PPP = Precise Point Positioning, DD = Double Differences)

In the first campaign, namely MIST_11, the aforementioned parameter is set to 0,0005 meters/hour. In the following tables the resulting coordinates for Como and Dani stations are reported.

DOY	HEIGHT [m]	RMS [m]	LATITUDE	RMS [sec]	RMS [m]	LONGITUDE	RMS [sec]	RMS [m]
300	292,282	0,0004	45°48'7,789"	0,0001	0,0031	9°5'44,244"	0,0002	0,0062
301	292,289	0,0005	45°48'7,789"	0,0001	0,0031	9°5'44,244"	0,0003	0,0093
302	292,289	0,0006	45°48'7,789"	0,0001	0,0031	9°5'44,243"	0,0003	0,0093
303	292,284	0,0006	45°48'7,789"	0,0001	0,0031	9°5'44,243"	0,0003	0,0093
304	292,287	0,0006	45°48'7,789"	0,0001	0,0031	9°5'44,243"	0,0003	0,0093
305	292,281	0,0005	45°48'7,789"	0,0001	0,0031	9°5'44,243"	0,0003	0,0093
306	292,283	0,0004	45°48'7,789"	0,0001	0,0031	9°5'44,243"	0,0002	0,0062

Table 19: Mist_11 coordinate results from day 26th October 2008 (Day of Year, DOY, 300) to 1st November 2008 (Day of Year, DOY, 306) for Como station

DOY	HEIGHT [m]	RMS [m]	LATITUDE	RMS [sec]	RMS [m]	LONGITUDE	RMS [sec]	RMS [m]
300	373,03	0,0007	45°44'50,23"	0,0002	0,0062	9°0'30,643"	0,0004	0,0124
301	373,036	0,0008	45°44'50,23"	0,0002	0,0062	9°0'30,643"	0,0004	0,0124
302	373,041	0,0009	45°44'50,23"	0,0002	0,0062	9°0'30,643"	0,0005	0,0154
303	373,043	0,0009	45°44'50,231"	0,0002	0,0062	9°0'30,643"	0,0005	0,0154
304	373,041	0,0008	45°44'50,231"	0,0002	0,0062	9°0'30,643"	0,0005	0,0154
305	373,049	0,0008	45°44'50,231"	0,0002	0,0062	9°0'30,643"	0,0005	0,0154
306	373,041	0,0007	45°44'50,231"	0,0002	0,0062	9°0'30,643"	0,0004	0,0124

Table 20: Mist_11 coordinate results from day 26th October 2008 (Day of Year, DOY, 300) to 1st November 2008 (Day of Year, DOY, 306) for Dani station

The coordinate results are statistically equivalent for the two solutions.

Some statistics for the troposphere estimation are reported in Table 21 and in Table 22. Graphical representations are in Figure 27 and Figure 28.

	Como DD	Como PPP	Como DD vs Como PPP	
min [m]	2,263	2,279	correlation index	97,96%
max [m]	2,419	2,411	max difference [m]	0,017
mean [m]	2,369	2,369	min difference [m]	-0,022
std [m]	0,033	0,031		

Como DD minus Como PPP

mean [m]	0
std [m]	0,007

Table 21: Mist_11 total zenith delay for Como station (DD = double differences, PPP = precise point positioning)

	Dani DD	Dani PPP	Como DD vs Como PPP	
min [m]	2,207	2,255	correlation index	97,74%
max [m]	2,394	2,383	max difference [m]	0,019
mean [m]	2,34	2,341	min difference [m]	-0,023
std [m]	0,038	0,031		

Dani DD minus Dani PPP

mean [m]	0,001
std [m]	0,007

Table 22: Mist_11 total zenith delay for Dani station (DD = double differences, PPP = precise point positioning)

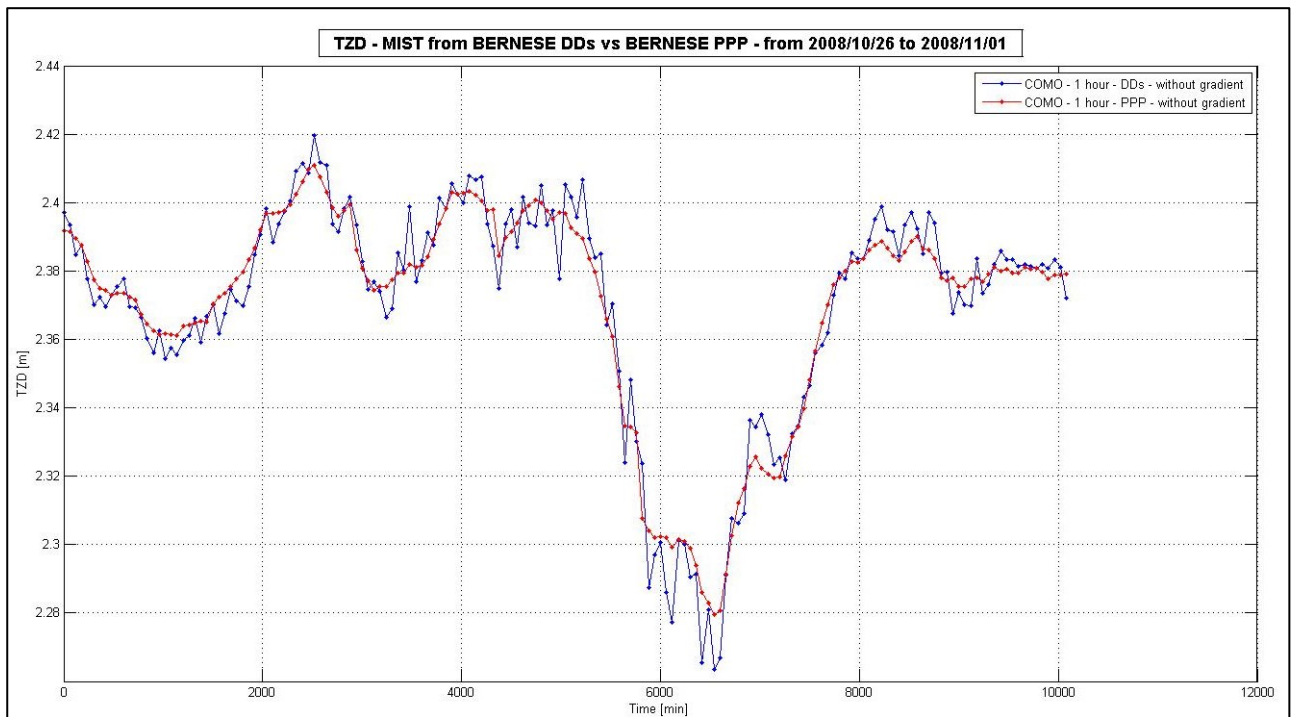


Figure 27: Total zenith delay for Como station, from 26th October 2008 to 1st November 2008 (Mist_11)

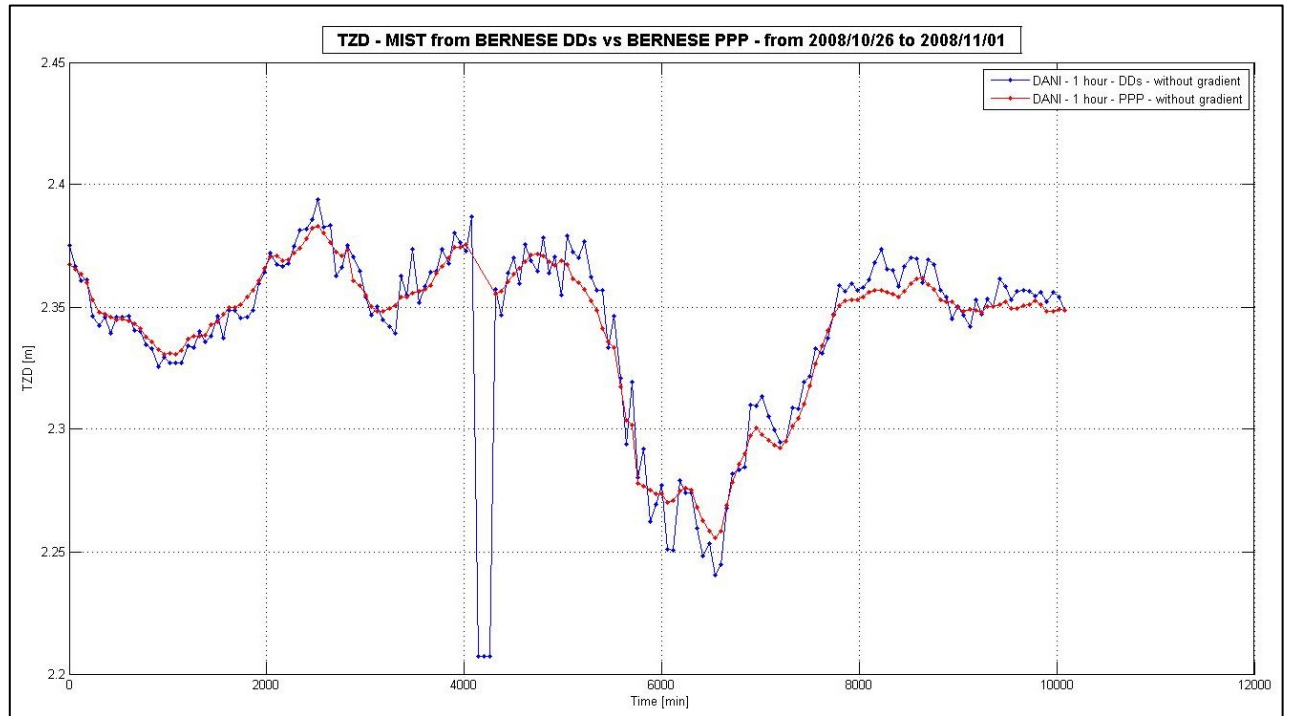


Figure 28: Total zenith delay for Dani station, from 26th October 2008 to 1st November 2008 (Mist_11)

The double differences solution shows variability larger than the Precise Point Positioning one for both stations. As can be seen in Figure 28, the DD solution for the third day (4000 min) shows a strange behavior, probably due to the fact that the program is not able to estimate the wet component of the delay and so only the a priori value is considered as the total. In the same epoch

the PPP solution doesn't provide any solution (note the lack of homologues three blue dots in the red line).

In the second campaign, namely MIST_12, the sigma parameter is set to 0.001 meters/hour. In the following tables the coordinate results for the entire week are reported.

DOY	HEIGHT [m]	RMS [m]	LATITUDE	RMS [sec]	RMS [m]	LONGITUDE	RMS [sec]	RMS [m]
300	292,282	0,0004	45°48'7,789"	0,0001	0,0031	9°5'44,244"	0,0002	0,0062
301	292,289	0,0005	45°48'7,789"	0,0001	0,0031	9°5'44,244"	0,0003	0,0093
302	292,29	0,0005	45°48'7,789"	0,0001	0,0031	9°5'44,243"	0,0003	0,0093
303	292,286	0,0006	45°48'7,789"	0,0001	0,0031	9°5'44,243"	0,0003	0,0093
304	292,287	0,0005	45°48'7,789"	0,0001	0,0031	9°5'44,243"	0,0003	0,0093
305	292,281	0,0005	45°48'7,789"	0,0001	0,0031	9°5'44,243"	0,0003	0,0093
306	292,284	0,0004	45°48'7,789"	0,0001	0,0031	9°5'44,243"	0,0002	0,0062

Table 23: Mist_12 coordinate results from day 26 October 2008 (Day of Year, DOY, 300) to 1 November 2008 (Day of Year, DOY, 306) for Como station

DOY	HEIGHT [m]	RMS [m]	LATITUDE	RMS [sec]	RMS [m]	LONGITUDE	RMS [sec]	RMS [m]
300	373,029	0,0007	45°44'50,23"	0,0002	0,0062	9°0'30,643"	0,0004	0,0124
301	373,036	0,0008	45°44'50,23"	0,0002	0,0062	9°0'30,643"	0,0004	0,0124
302	373,042	0,0009	45°44'50,23"	0,0002	0,0062	9°0'30,643"	0,0005	0,0154
303	373,045	0,0009	45°44'50,231"	0,0002	0,0062	9°0'30,643"	0,0005	0,0154
304	373,041	0,0008	45°44'50,231"	0,0002	0,0062	9°0'30,643"	0,0005	0,0154
305	373,05	0,0008	45°44'50,231"	0,0002	0,0062	9°0'30,643"	0,0005	0,0154
306	373,041	0,0007	45°44'50,231"	0,0002	0,0062	9°0'30,643"	0,0004	0,0124

Table 24: Mist_12 coordinate results from day 26 October 2008 (DOY 300) to 1 November 2008 (DOY 306) for Dani station

In Table 25 and in Table 26 some statistics for the troposphere estimation are reported and in Figure 29 and in Figure 30 the graphical representations.

	Como DD	Como PPP	Como DD vs Como PPP	
min [m]	2,263	2,276	correlation index	98,12%
max [m]	2,419	2,413	max difference [m]	0,0163
mean [m]	2,369	2,369	min difference [m]	-0,02
std [m]	0,033	0,031		

Como DD minus Como PPP

mean [m]	0,000
std [m]	0,007

Table 25: Mist_12 total zenith delay for Como station (DD = double differences, PPP = precise point positioning)

	Dani DD	Dani PPP	Como DD vs Como PPP	
min [m]	2,207	2,252	correlation index	97,89%
max [m]	2,394	2,385	max difference [m]	0,019
mean [m]	2,34	2,341	min difference [m]	-0,019
std [m]	0,038	0,031		

Dani DD minus Dani PPP

mean [m]	0,001
std [m]	0,007

Table 26: Mist_12 total zenith delay for Dani station (DD = double differences, PPP = precise point positioning)

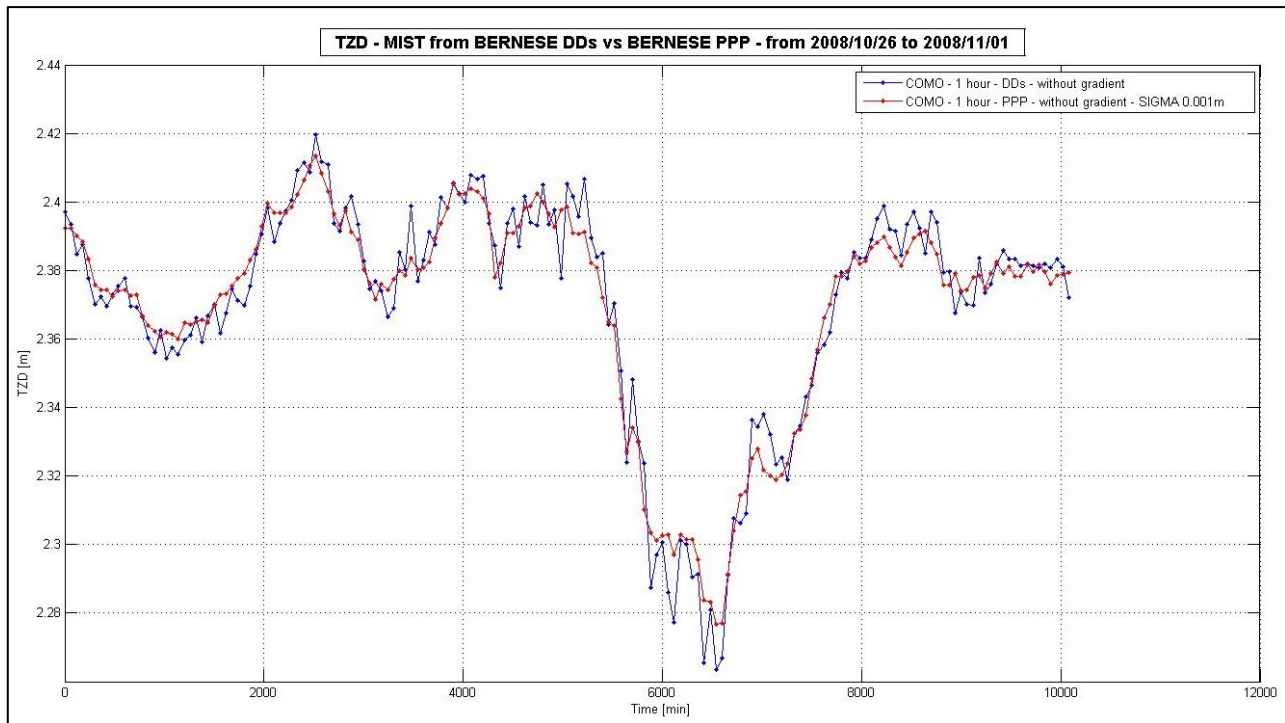


Figure 29: Total zenith delay for Como station, from 26th October 2008 to 1st November 2008 (Mist_12)

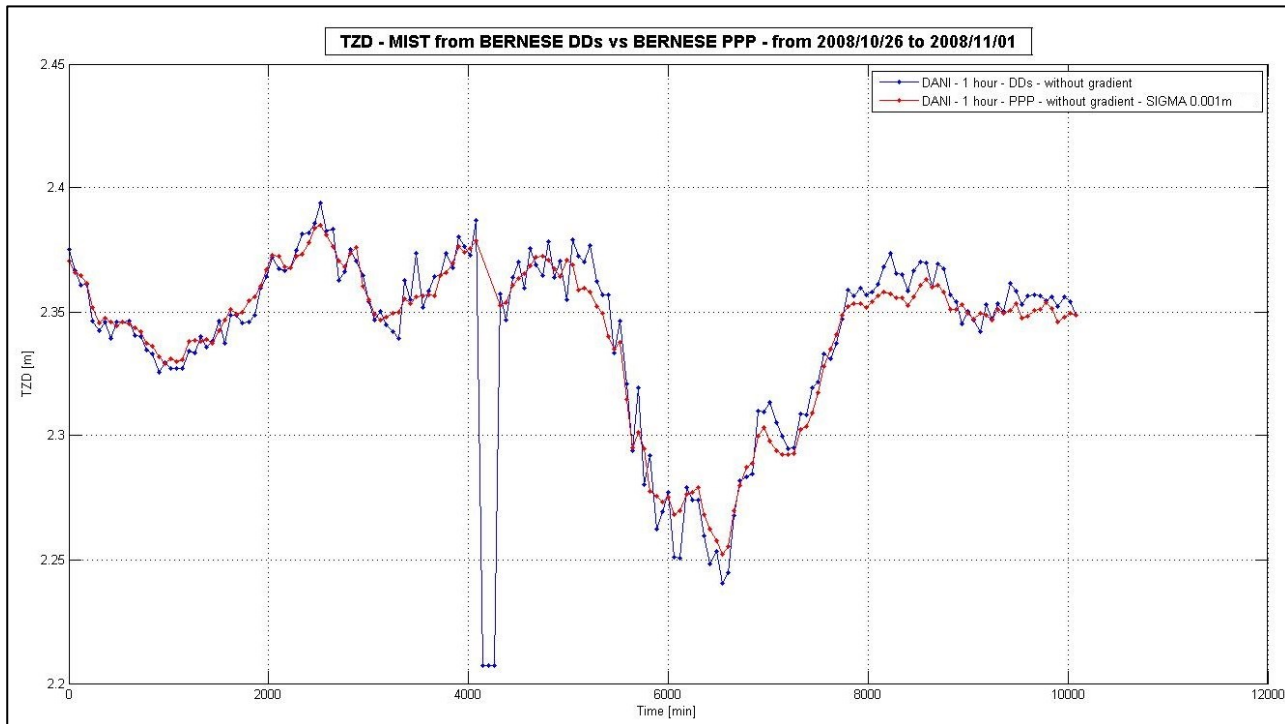


Figure 30: Total zenith delay for Dani station, from 26th October 2008 to 1st November 2008 (Mist_12)

A larger sigma of the relative constrain between TZDs of two consecutive epochs doesn't significantly affect the estimated time series variability.

Increasing the sigma parameter has as a consequence a solution more correlated than the previous case and also more pronounced peaks. The same strange behavior of Mist_11 campaign's is present for Dani station.

In the third campaign, namely Mist_13, the sigma parameter is set to 0,01 meter/hour, of an order of magnitude higher than Mist_12. In the following tables the coordinate results for the entire week are reported.

DOY	HEIGHT [m]	RMS [m]	LATITUDE	RMS [sec]	RMS [m]	LONGITUDE	RMS [sec]	RMS [m]
300	292,282	0,0004	45°48'7,789"	0,0001	0,0031	9°5'44,244"	0,0002	0,0062
301	292,28	0,0005	45°48'7,789"	0,0001	0,0031	9°5'44,244"	0,0003	0,0093
302	292,289	0,0005	45°48'7,789"	0,0001	0,0031	9°5'44,243"	0,0003	0,0093
303	292,288	0,0006	45°48'7,789"	0,0001	0,0031	9°5'44,243"	0,0003	0,0093
304	292,286	0,0005	45°48'7,789"	0,0001	0,0031	9°5'44,243"	0,0003	0,0093
305	292,281	0,0005	45°48'7,789"	0,0001	0,0031	9°5'44,243"	0,0003	0,0093
306	292,284	0,0004	45°48'7,789"	0,0001	0,0031	9°5'44,243"	0,0002	0,0062

Table 27: Mist_13 coordinate results from day 26 October 2008 (Day of year, DOY, 300) to 1 November 2008 (Day of year, DOY, 306) for Como station

DOY	HEIGHT [m]	RMS [m]	LATITUDE	RMS [sec]	RMS [m]	LONGITUDE	RMS [sec]	RMS [m]
300	373,03	0,0007	45°44'50,23"	0,0002	0,0062	9°0'30,643"	0,0004	0,0124
301	373,037	0,0008	45°44'50,23"	0,0002	0,0062	9°0'30,643"	0,0004	0,0124
302	373,042	0,0009	45°44'50,23"	0,0002	0,0062	9°0'30,643"	0,0005	0,0154
303	373,047	0,0009	45°44'50,23"	0,0002	0,0062	9°0'30,643"	0,0005	0,0154
304	373,041	0,0008	45°44'50,23"	0,0002	0,0062	9°0'30,643"	0,0005	0,0154
305	373,05	0,0008	45°44'50,23"	0,0002	0,0062	9°0'30,643"	0,0005	0,0154
306	373,041	0,0008	45°44'50,23"	0,0002	0,0062	9°0'30,643"	0,0004	0,0124

Table 28: Mist_13 coordinate results from day 26 October 2008 (Day of year, DOY, 300) to 1 November 2008 (Day of year, DOY, 306) for Dani station

Some statistics for the troposphere estimation are reported in Table 29 and Table 30. Graphical representations are in Figure 31 and Figure 32.

	Como DD	Como PPP	Como DD vs Como PPP	
min [m]	2,263	2,274	correlation index	98,04%
max [m]	2,419	2,416	max difference [m]	0,0183
mean [m]	2,369	2,369	min difference [m]	-0,021
std [m]	0,033	0,032		

Como DD minus Como PPP

mean [m]	0,000
std [m]	0,007

Table 29: Mist_13 total zenith delay for Como station (DD = double differences, PPP = precise point positioning)

	Dani DD	Dani PPP	Dani DD vs Dani PPP	
min [m]	2,207	2,249	correlation index	97,85%
max [m]	2,394	2,386	max difference [m]	0,019
mean [m]	2,34	2,341	min difference [m]	-0,018
std [m]	0,038	0,031		

Dani DD minus Dani PPP

mean [m]	0,002
std [m]	0,007

Table 30: Mist_13 total zenith delay for Dani station (DD = double differences, PPP = precise point positioning)

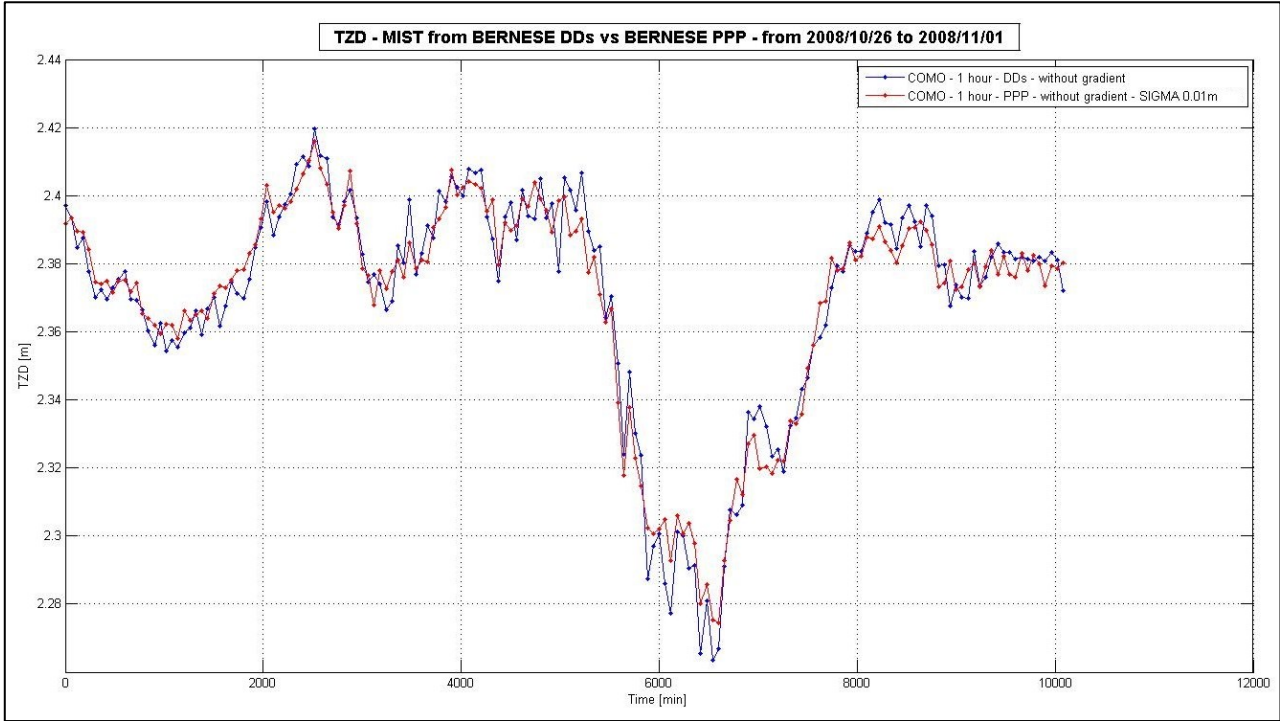


Figure 31: Total zenith delay for Como station, from 26th October 2008 to 1st November 2008 (Mist_13)

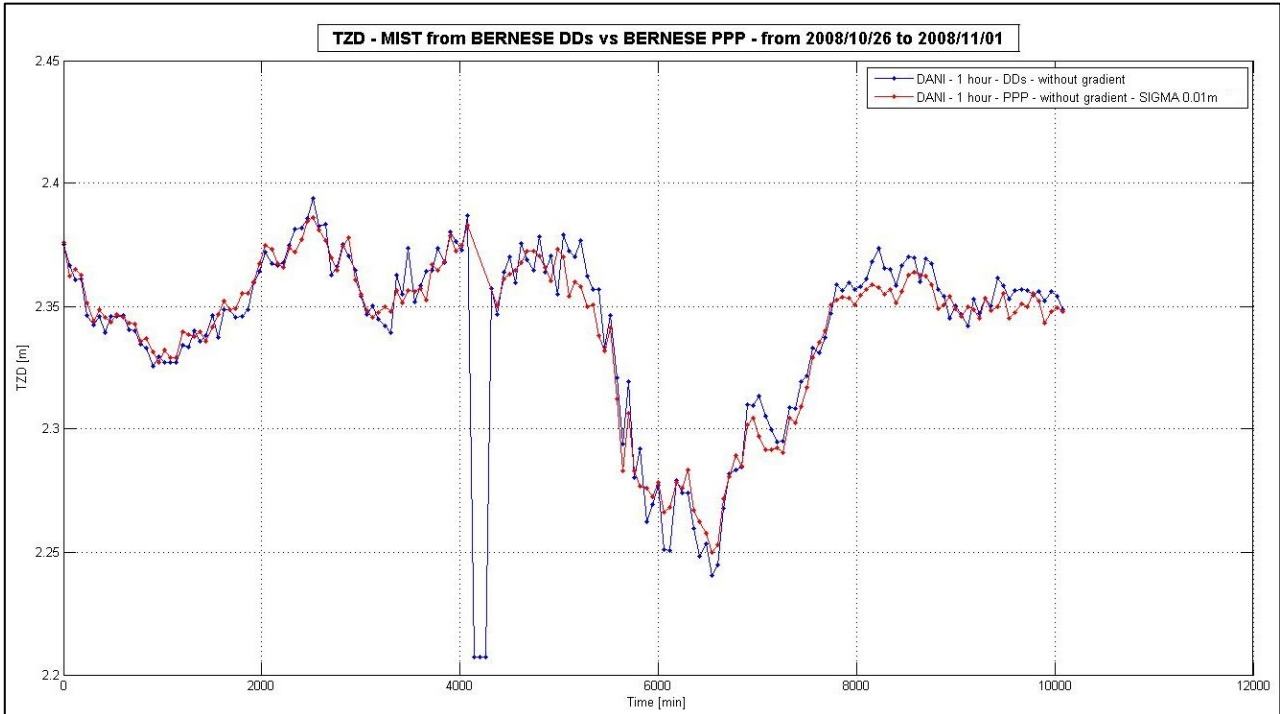


Figure 32: Total zenith delay for Dani station, from 26th October 2008 to 1st November 2008 (Mist_13)

The deviations are now more pronounced and the correlation is increased with respect to the previous campaigns. Here it is now redundant to point out the strange behavior of Dani station.

In order to compare the EUREF results a new campaign was performed, MIST_18. The tropospheric estimation rate is one hour but starting from half past midnight, the elevation cutoff is set to 10°. In the MIST_18 campaign is not introduced a constraint on the tropospheric parameters. The EUREF comparisons are between the three different solutions provided by EUREF and only the PPP solution obtained in MIST_18 campaign.

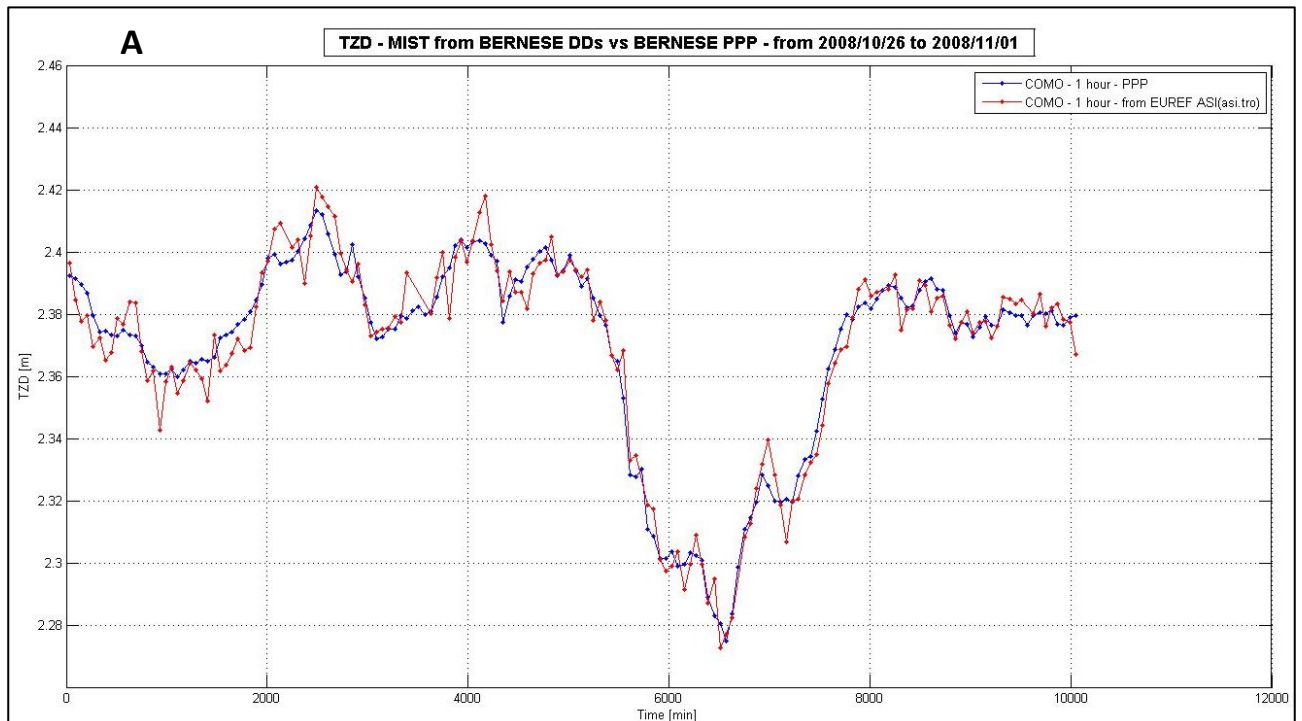
In Table 31 and Table 32 some statistics are reported for the original solutions and the differences between them. A graphical representation is given in Figure 33.

	COMO PPP	COMO ASI	COMO EUREF	COMO BEK
min [m]	2,275	2,273	2,278	2,278
max [m]	2,413	2,421	2,418	2,416
mean [m]	2,369	2,369	2,371	2,371
std [m]	0,032	0,032	0,032	0,032
sample size	168	160	168	168

Table 31: Minimum, maximum, mean, standard deviation values and the number of estimated parameters for PPP (MIST_18 solution) and the three different EUREF products

	PPP vs ASI	PPP vs EUREF	PPP vs BEK
correlation index	97,872%	99,611%	99,713%
Differences: max [m]	0,018	0,005	0,007
Differences: min [m]	-0,015	-0,009	-0,009
Differences: mean [m]	0,000	-0,001	-0,002
Differences: std [m]	0,007	0,003	0,002
Differences: sample size	160	168	168

Table 32: Correlation index between PPP and EUREF products, statistics of the differences



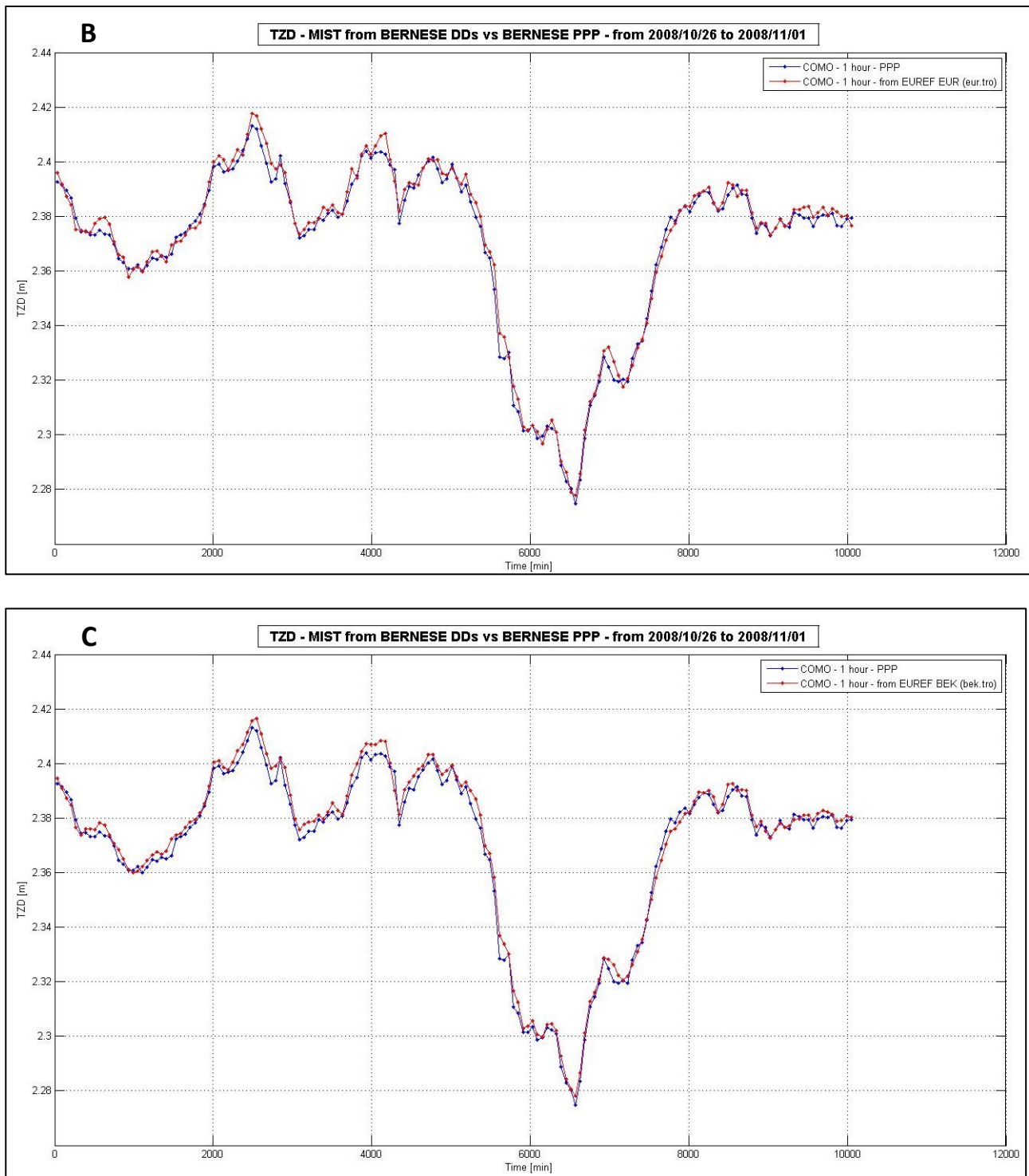


Figure 33: Total zenith delay solution comparison: A) PPP vs ASI; B) PPP vs EUREF; C) PPP vs BEK

4.3 UJI data processing

In this section the UJI tropospheric delays obtained with the software RTnet are compared with different solutions obtained with Bernese PPP. Bernese PPP batch solution is compared with the RTnet kalman one to evaluate the effect of the a priori sigma given to the constraints on two consecutive zenith delay values. Details about constraints are reported in section 3.2.1.

4.3.1 Comparison with respect to RTnet solution

As for Mist data processing, the following table summarizes basics settings applied in different campaigns.

Campaign name	Gradient model	ZTD Estimation rate	Sigma Parameter [m/min]
UJI_7	Not applied	1 min	0,001
UJI_8	Not applied	1 min	0,003
UJI_9	Not applied	1 min	0,005
UJI_10	Not applied	1 min	0,009
UJI_11	Not applied	1 min	0,0001
UJI_12	Not applied	1 min	0,0005

Table 33: Basic settings for Uji campaigns

4.3.1.1 Notes about RTnet solution

As written in section 4.1, the reference case is a solution provided by RTnet software only in terms of total zenith delay. These delays are estimated at a 30 seconds rate and without the gradient model. Since the Bernese software allows a maximum temporal resolution of 1 minute, this is chosen for the following elaborations. In order to be consistent with RTnet solution, the gradient model is not applied as well.

Another aspect to be pointed out for RTnet is that the program needs about 25 epochs to reach a reasonable solution. This is due to the implemented Kalman filter method. This behavior is well explained by Figure 34, reported as an example. These initial epochs, common to the entire set of Uji stations, were removed before comparing the Uji results with the Bernese ones.

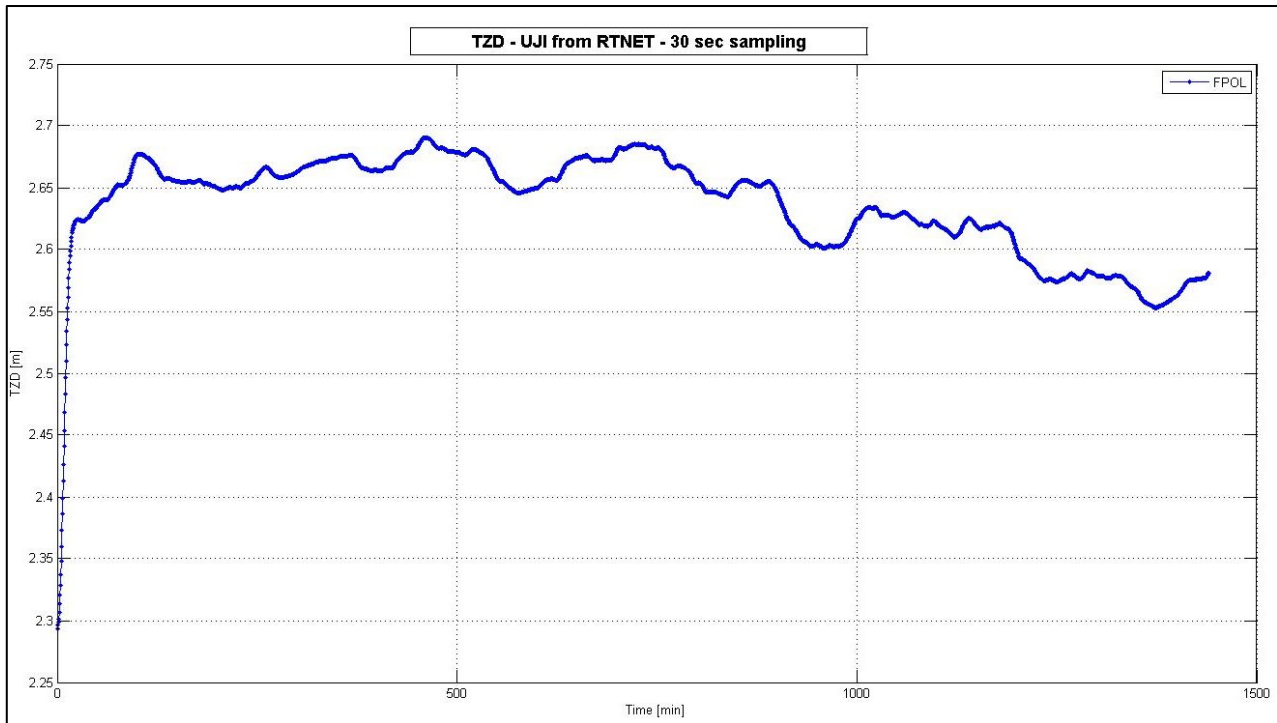


Figure 34: Total zenith delay RTnet solution for FPOL station, 26th July 2012. Note the behavior in the first minutes.

4.3.1.2 Solution details

The presented experiments are characterized by different values of the sigma parameter from 0,0001 to 0,009 m/min. In Table 34 correlation, maximum and minimum differences between the RTnet and Bernese solution are reported. Also minimum, maximum, mean and standard deviation are reported.

By looking at Table 34, one notices that MMKI (5th station) shows the lowest correlation value. This behavior is well explained by looking to Figure 35. For sure some technical problems occurred in that day until midday.

Considering only the data from 1000th minute, the correlation index increases up to 91,475%.

In the next tables the MMKI solutions are reported but it is excluded in the solution comparisons graphs reported at the end of each set of experiments.

Sigma = 0,001 m/min											
	UJI_7 vs UJI RTnet			UJI_7				UJI RTnet			
STATION	CORRELATION INDEX [-]	MAXIMUM DIFFERENCE [m]	MINIMUM DIFFERENCE [m]	Min [m]	Max [m]	Mean [m]	Std [m]	Min [m]	Max [m]	Mean [m]	Std [m]
FPOL	95,567%	0,040	-0,014	2,546	2,684	2,628	0,033	2,553	2,690	2,638	0,036
KUJI	95,838%	0,045	-0,012	2,539	2,677	2,624	0,033	2,545	2,695	2,638	0,036
SAYM	94,418%	0,043	-0,020	2,537	2,685	2,624	0,036	2,547	2,691	2,637	0,040
ISDA	95,211%	0,041	-0,029	2,548	2,682	2,625	0,032	2,548	2,690	2,638	0,036
MMKI	86,592%	0,049	-0,079	2,543	2,691	2,623	0,030	2,544	2,680	2,615	0,033
SCIN	94,097%	0,047	-0,011	2,541	2,657	2,599	0,027	2,551	2,694	2,613	0,033
KMSM	95,623%	0,040	-0,026	2,544	2,682	2,624	0,033	2,543	2,693	2,635	0,037
OYMZ	94,545%	0,054	-0,016	2,539	2,681	2,631	0,033	2,553	2,696	2,642	0,035
SKRA	94,674%	0,049	-0,021	2,532	2,676	2,620	0,033	2,544	2,684	2,632	0,034
KOGR	95,624%	0,039	-0,029	2,545	2,682	2,626	0,033	2,547	2,691	2,637	0,037
RISH	95,924%	0,030	-0,024	2,533	2,674	2,619	0,034	2,538	2,680	2,627	0,037
UGOL	94,157%	0,048	-0,020	2,541	2,678	2,625	0,033	2,547	2,689	2,641	0,036
KTGW	94,555%	0,057	-0,018	2,543	2,681	2,625	0,034	2,549	2,693	2,633	0,036
RKNN	95,952%	0,041	-0,020	2,531	2,674	2,626	0,035	2,538	2,689	2,634	0,036
YUTO	94,786%	0,054	-0,019	2,538	2,683	2,627	0,035	2,550	2,692	2,638	0,035

Table 34: Total zenith delay: Comparison between RTnet and Bernese (Uji_7) solutions

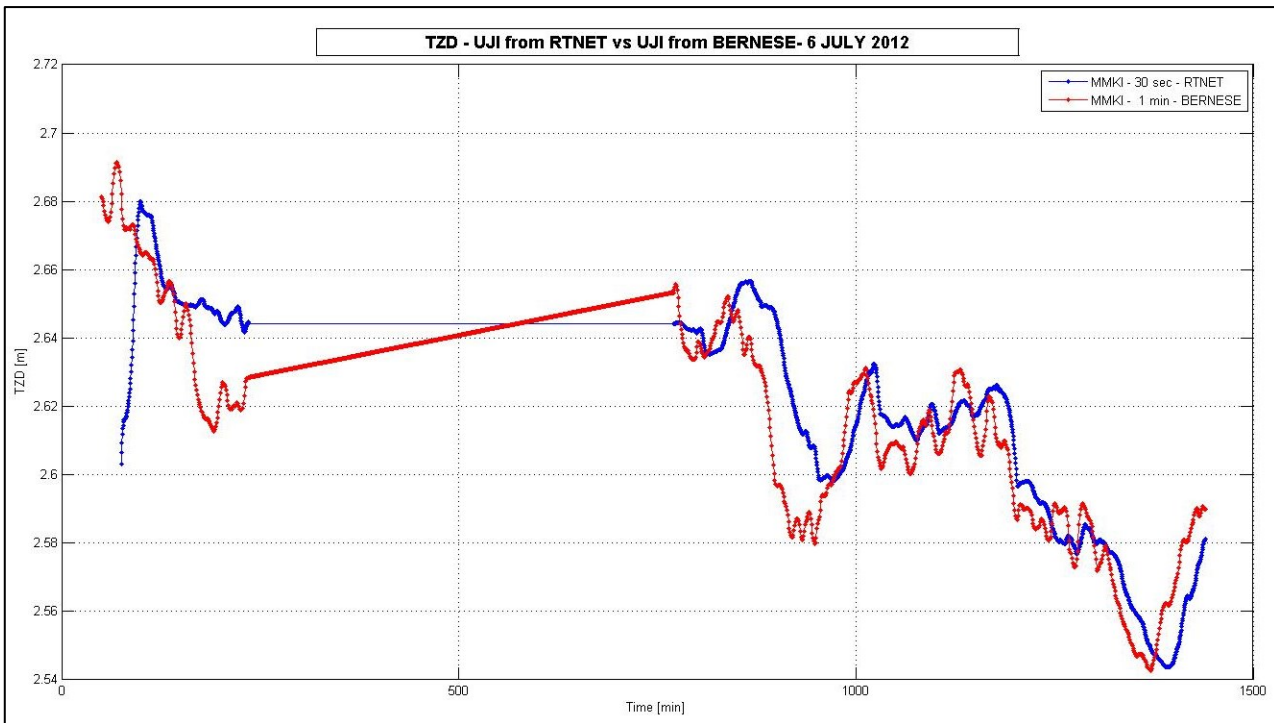


Figure 35: MMKI zenith tropospheric delay, note the strange behavior from 250th minute to 750th

As regards the solutions for the other stations, the maximum, minimum values differ in the order of millimeters, the mean differs in the centimeters, instead the standard deviation for the Bernese solution is always lower than the RTnet one. The correlation index is always greater than 94%. In Figure 36 the tropospheric solution for MMKI station is reported.

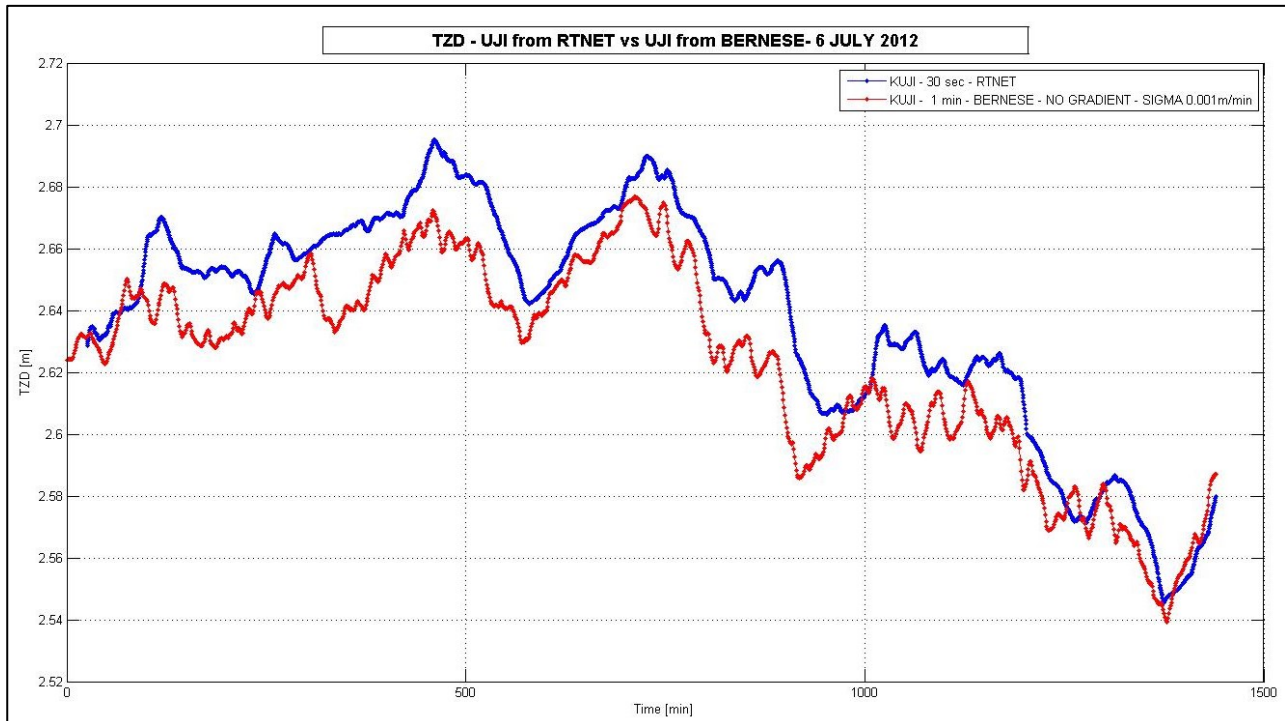
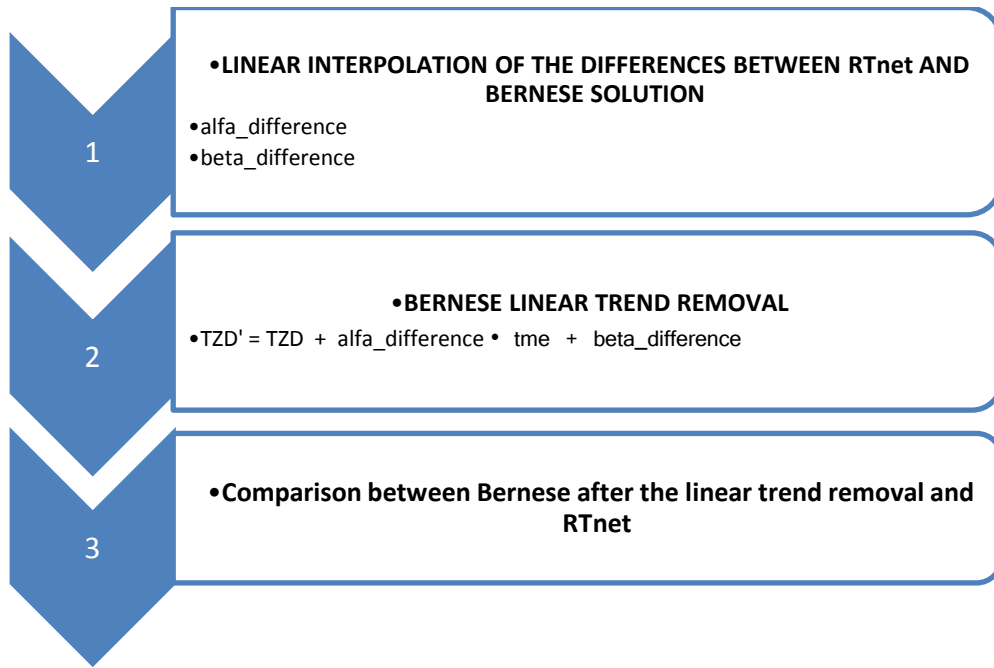


Figure 36: Tropospheric zenith delay for MMKI station (Uji_7), sigma 0,001 m/min

The reader should notice that the two solutions are very close but there is an evident bias.

This behavior has been studied more in detail.

The following procedure is applied:



Where the linear interpolation equation is:

$$y = \alpha \cdot x + \beta$$

Equation 53: Linear interpolation

In Table 35 there are correlation, maximum and minimum differences between RTnet and Bernese after linear trend removal solutions.

With respect to the previous homologous values (Table 34) now the correlation coefficient increase for all the stations except KMSM, RISH and YUTO, and the maximum/minimum differences decrease for all.

With respect to the homologous table, Table 34, the Bernese after linear trend removal solution shows values more similar with RTnet.

This is a further confirmation that the estimates of the two different software are quite equivalent from these mathematical indexes.

Sigma = 0,001 m/min (after linear trend removal)											
	UJI_7 vs UJI RTnet			UJI_7				UJI RTnet			
STATION	CORRELATION INDEX [-]	MAXIMUM DIFFERENCE [m]	MINIMUM DIFFERENCE [m]	Min [m]	Max [m]	Mean [m]	Std [m]	Min [m]	Max [m]	Mean [m]	Std [m]
FPOL	95,708%	0,030	-0,029	2,553	2,695	2,638	0,035	2,553	2,690	2,638	0,036
KUJI	95,860%	0,032	-0,027	2,551	2,691	2,638	0,035	2,545	2,695	2,638	0,036
SAYM	94,881%	0,030	-0,028	2,545	2,700	2,637	0,039	2,547	2,691	2,637	0,040
ISDA	95,215%	0,029	-0,045	2,558	2,695	2,638	0,034	2,548	2,690	2,638	0,036
MMKI	87,791%	0,043	-0,091	2,545	2,694	2,615	0,033	2,544	2,680	2,615	0,033
SCIN	95,979%	0,023	-0,026	2,545	2,686	2,613	0,033	2,551	2,694	2,613	0,033
KMSM	95,558%	0,029	-0,039	2,552	2,693	2,635	0,034	2,543	2,693	2,635	0,037
OYMZ	94,577%	0,042	-0,026	2,552	2,692	2,642	0,033	2,553	2,696	2,642	0,035
SKRA	94,676%	0,037	-0,033	2,545	2,688	2,632	0,033	2,544	2,684	2,632	0,034
KOGR	96,169%	0,028	-0,049	2,550	2,695	2,637	0,037	2,547	2,691	2,637	0,037
RISH	95,910%	0,023	-0,031	2,540	2,682	2,627	0,034	2,538	2,680	2,627	0,037
UGOL	94,305%	0,033	-0,032	2,553	2,694	2,641	0,035	2,547	2,689	2,641	0,036
KTGW	94,557%	0,048	-0,027	2,552	2,690	2,633	0,034	2,549	2,693	2,633	0,036
RKNN	95,952%	0,031	-0,031	2,542	2,684	2,634	0,035	2,538	2,689	2,634	0,036
YUTO	94,738%	0,042	-0,031	2,551	2,695	2,638	0,035	2,550	2,692	2,638	0,035

Table 35: Total zenith delay: Comparison between RTnet solution and Bernese (Uji_7) after linear trend removal

However, from a more careful analysis of Figure 37, it can be stated that some others effects act on the Bernese solution.

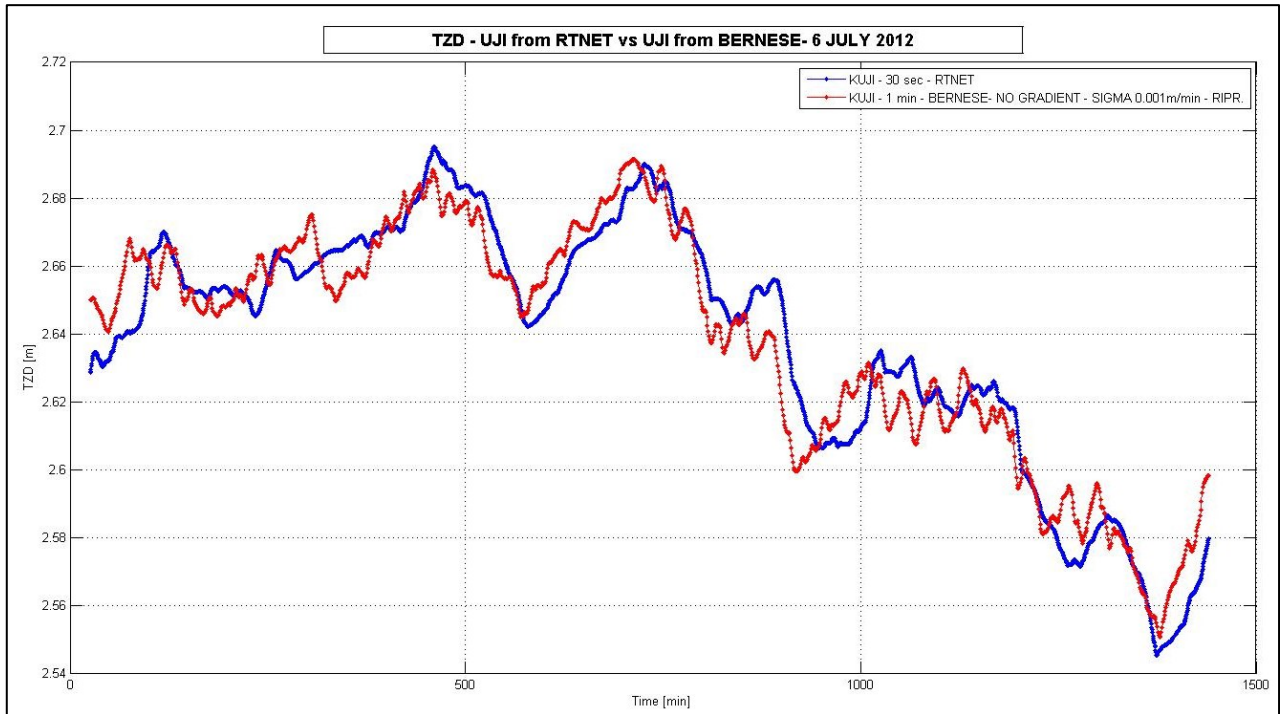


Figure 37: Tropospheric zenith delay for MMKI station, Bernese after linear trend removal solution in red (Uji_7)

Other comment is about the general trend observable from Figure 37. In some epochs, for example at about 250th minute, the two solutions are note coherent. In particular RTnet estimates an increase in the delay, while Bernese estimates a decrease. This difference in trend happens also in other stations; as an example Figure 38 is reported.

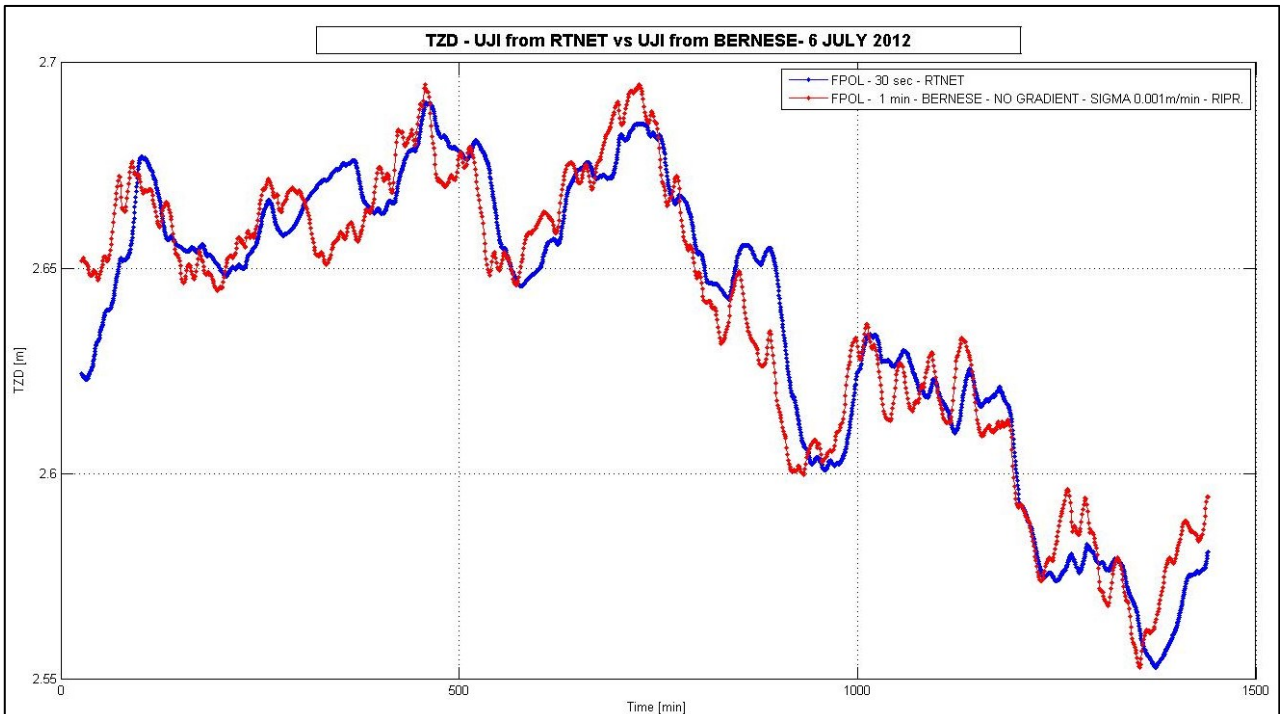


Figure 38: Tropospheric zenith delay for FPOL station, Bernese after linear trend removal solution in red (Uji_7)

Another comment regards the variability. Referring to Figure 38, one can see that, at the 1250th minute, the Bernese solution shows the same trend of RTnet but with peak values a little bit higher. In addition also a temporal shift is present due to the implemented Kalman filter.

The next experiments, based on these previous considerations, are obtained by varying the sigma parameter. An higher sigma means less constraint between the total zenith delay at epoch t and the next epoch $t+1$, so a more noisy solution is obtained. A lower value implies the reverse.

In Uji_8 campaign the sigma parameter is set to 0,003 meters/minutes. This value is coherent to RTnet value.

In Table 36 statistics are reported for all the stations.

From the mathematical point of view the same reasoning done for Uji_7 is valid also for Uji_8. The effect of the sigma parameter is evident by looking to Figure 39. The variability now is more pronounced, as expected, but substantially the behavior respect to RTnet solution is as in the previous campaign.

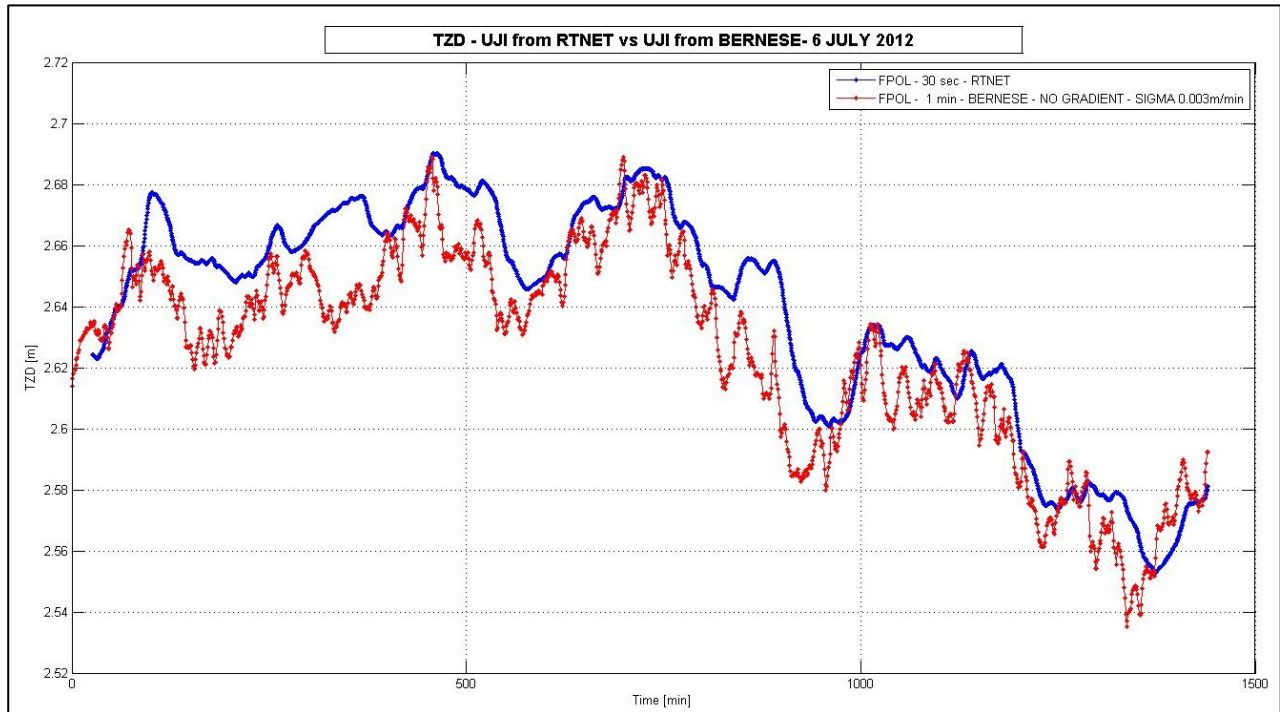


Figure 39: Tropospheric zenith delay for FPOL station, Bernese solution in red (Uji_8)

Sigma = 0,003 m/min											
	UJI_8 vs UJI RTnet			UJI_8				UJI RTnet			
STATION	CORRELATION INDEX [-]	MAXIMUM DIFFERENCE [m]	MINIMUM DIFFERENCE [m]	Min [m]	Max [m]	Mean [m]	Std [m]	Min [m]	Max [m]	Mean [m]	Std [m]
FPOL	93,720%	0,051	-0,020	2,535	2,689	2,625	0,034	2,553	2,690	2,638	0,036
KUJI	94,362%	0,049	-0,018	2,543	2,689	2,626	0,034	2,545	2,695	2,638	0,036
SAYM	93,405%	0,055	-0,022	2,534	2,695	2,623	0,037	2,547	2,691	2,637	0,040
ISDA	93,102%	0,052	-0,028	2,543	2,685	2,624	0,033	2,548	2,690	2,638	0,036
MMKI	86,550%	0,057	-0,083	2,540	2,699	2,625	0,031	2,544	2,680	2,615	0,033
SCIN	91,236%	0,055	-0,016	2,537	2,666	2,601	0,028	2,551	2,694	2,613	0,033
KMSM	93,760%	0,052	-0,028	2,535	2,688	2,624	0,034	2,543	2,693	2,635	0,037
OYMZ	92,606%	0,062	-0,040	2,538	2,687	2,632	0,035	2,553	2,696	2,642	0,035
SKRA	93,502%	0,057	-0,017	2,527	2,683	2,619	0,035	2,544	2,684	2,632	0,034
KOGR	93,740%	0,051	-0,030	2,537	2,685	2,624	0,034	2,547	2,691	2,637	0,037
RISH	94,802%	0,037	-0,030	2,529	2,679	2,619	0,035	2,538	2,680	2,627	0,037
UGOL	92,283%	0,057	-0,031	2,535	2,680	2,625	0,034	2,547	2,689	2,641	0,036
KTGW	93,462%	0,049	-0,025	2,537	2,694	2,626	0,035	2,549	2,693	2,633	0,036
RKNN	95,268%	0,043	-0,026	2,510	2,690	2,627	0,037	2,538	2,689	2,634	0,036
YUTO	93,752%	0,058	-0,022	2,520	2,703	2,627	0,036	2,550	2,692	2,638	0,035

Table 36: Total zenith delay: Comparison between RTnet solution and Bernese (Uji_8)

The output after the linear trend removal is graphically reported in Figure 40.

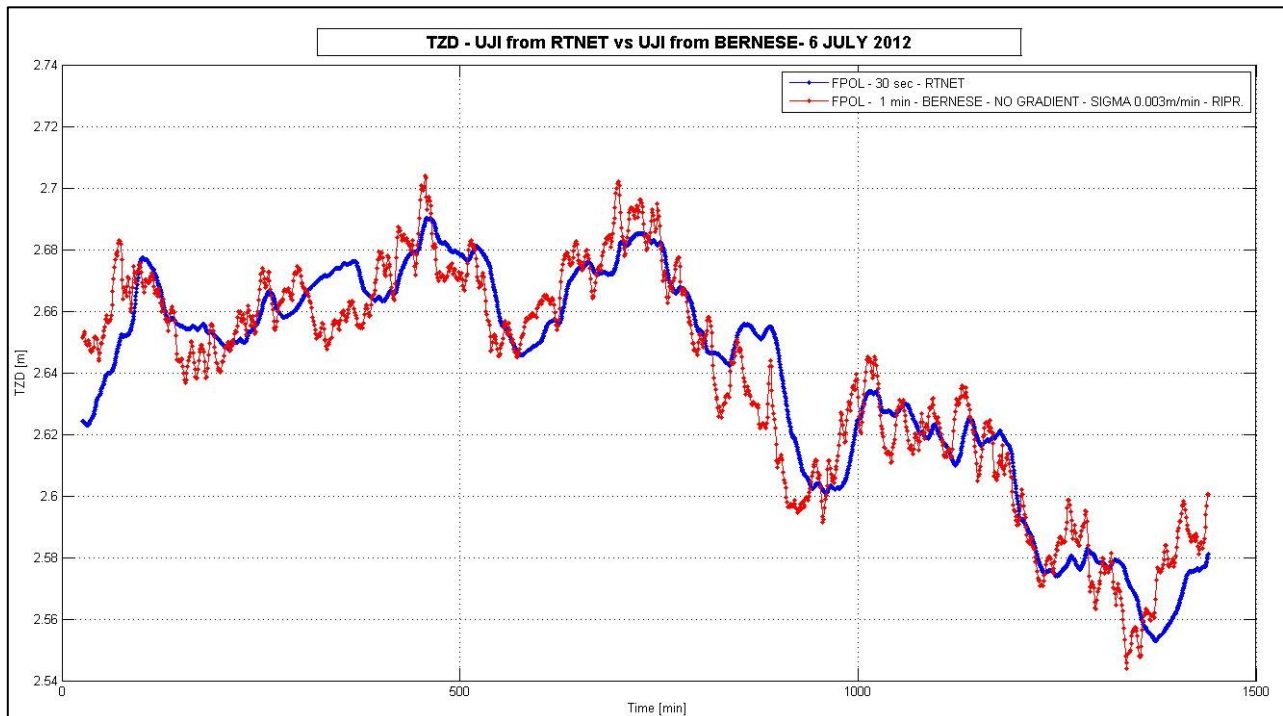


Figure 40: Tropospheric zenith delay for FPOL station, Bernese after linear trend removal solution in red (Uji_8)

With respect to Uji_7, both the original solution and after linear trend removal solutions Uji_8 presents lower correlation coefficients.

Even if Uji_8 campaign could suggest to move the sigma parameter in the other direction, in Uji_9 it is increased a little bit too. It's value is 0,005 meter/minute. This experiment is done in order to see how a small variation could affect the solution.

Sigma = 0,003 m/min (after linear trend removal)											
	UJI_8 vs UJI RTnet			UJI_8				UJI RTnet			
STATION	CORRELATION INDEX [-]	MAXIMUM DIFFERENCE [m]	MINIMUM DIFFERENCE [m]	Min [m]	Max [m]	Mean [m]	Std [m]	Min [m]	Max [m]	Mean [m]	Std [m]
FPOL	94,188%	0,039	-0,034	2,544	2,704	2,638	0,036	2,553	2,690	2,638	0,036
KUJI	94,503%	0,037	-0,032	2,553	2,701	2,638	0,035	2,545	2,695	2,638	0,036
SAYM	94,070%	0,040	-0,035	2,544	2,714	2,637	0,040	2,547	2,691	2,637	0,040
ISDA	93,337%	0,039	-0,045	2,553	2,698	2,638	0,035	2,548	2,690	2,638	0,036
MMKI	87,560%	0,053	-0,092	2,541	2,697	2,615	0,033	2,544	2,680	2,615	0,033
SCIN	94,175%	0,033	-0,031	2,539	2,694	2,613	0,034	2,551	2,694	2,613	0,033
KMSM	93,851%	0,042	-0,042	2,543	2,699	2,635	0,035	2,543	2,693	2,635	0,037
OYMZ	92,551%	0,050	-0,047	2,551	2,697	2,642	0,034	2,553	2,696	2,642	0,035
SKRA	93,354%	0,043	-0,032	2,542	2,696	2,632	0,034	2,544	2,684	2,632	0,034
KOGR	94,761%	0,039	-0,051	2,543	2,699	2,637	0,038	2,547	2,691	2,637	0,037
RISH	94,820%	0,030	-0,037	2,536	2,687	2,627	0,035	2,538	2,680	2,627	0,037
UGOL	92,483%	0,041	-0,044	2,549	2,696	2,641	0,035	2,547	2,689	2,641	0,036
KTGW	93,417%	0,041	-0,034	2,546	2,702	2,633	0,035	2,549	2,693	2,633	0,036
RKNN	95,164%	0,034	-0,037	2,521	2,698	2,634	0,036	2,538	2,689	2,634	0,036
YUTO	93,634%	0,047	-0,034	2,532	2,714	2,638	0,036	2,550	2,692	2,638	0,035

Table 37: Total zenith delay: Comparison between RTnet solution and Bernese after linear trend removal solution (Uji_8)

In Table 38 and in Table 39 statistics are reported for the original solution and for the solution after linear trend removal. The latter is obtained following the procedure reported before. In Figure 41 and Figure 42 the graphical solutions are reported, as an example, for YUTO station.

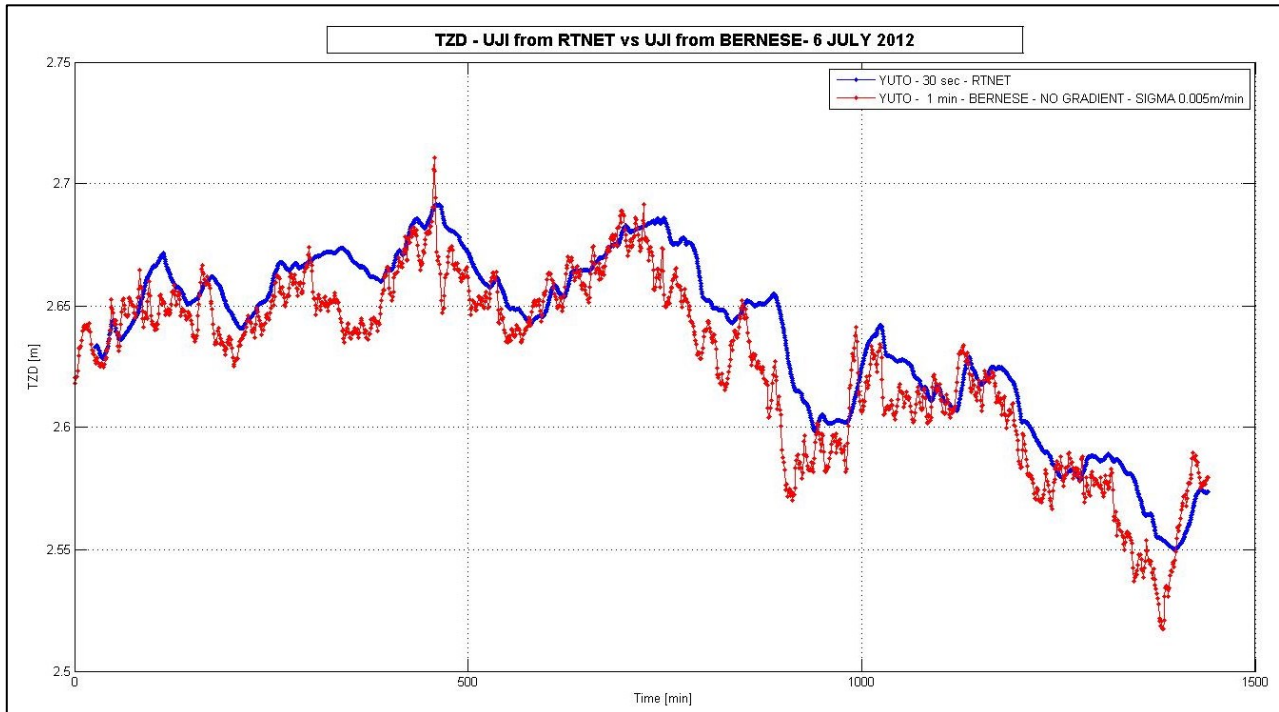


Figure 41: Tropospheric zenith delay for YUTO station, Bernese solution in red (Uji_9)

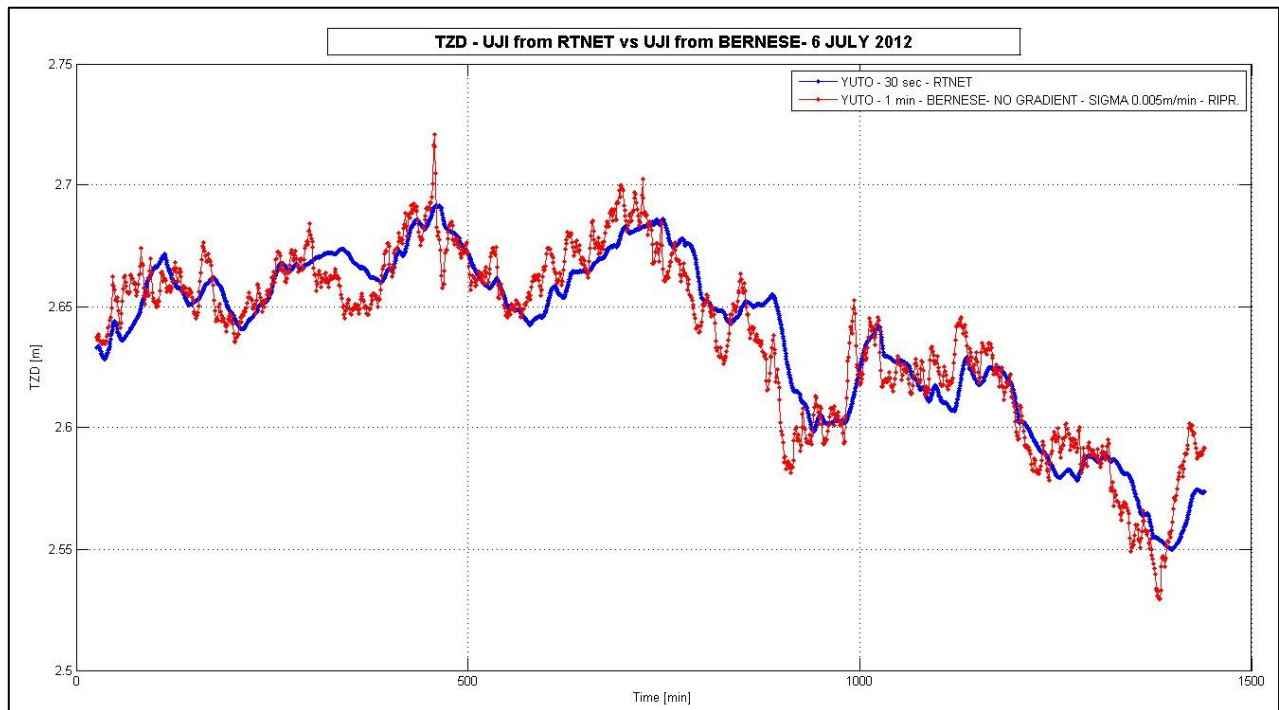


Figure 42: Tropospheric zenith delay for YUTO station, Bernese after linear trend removal solution in red (Uji_9)

Sigma = 0,005 m/min											
	UJI_9 vs UJI RTnet			UJI_9				UJI RTnet			
STATION	CORRELATION INDEX [-]	MAXIMUM DIFFERENCE [m]	MINIMUM DIFFERENCE [m]	Min [m]	Max [m]	Mean [m]	Std [m]	Min [m]	Max [m]	Mean [m]	Std [m]
FPOL	93,467%	0,054	-0,021	2,532	2,690	2,625	0,034	2,553	2,690	2,638	0,036
KUJI	94,116%	0,050	-0,019	2,541	2,689	2,626	0,034	2,545	2,695	2,638	0,036
SAYM	93,189%	0,057	-0,026	2,253	2,699	2,623	0,037	2,547	2,691	2,637	0,040
ISDA	92,775%	0,055	-0,028	2,541	2,688	2,624	0,033	2,548	2,690	2,638	0,036
MMKI	86,155%	0,061	-0,084	2,538	2,701	2,625	0,030	2,544	2,680	2,615	0,033
SCIN	90,708%	0,058	-0,016	2,535	2,668	2,601	0,028	2,551	2,694	2,613	0,033
KMSM	93,466%	0,056	-0,029	2,532	2,690	2,624	0,034	2,543	2,693	2,635	0,037
OYMZ	92,285%	0,064	-0,041	2,536	2,688	2,632	0,035	2,553	2,696	2,642	0,035
SKRA	93,260%	0,059	-0,018	2,525	2,685	2,619	0,035	2,544	2,684	2,632	0,034
KOGR	93,479%	0,055	-0,030	2,536	2,687	2,624	0,034	2,547	2,691	2,637	0,037
RISH	94,554%	0,040	-0,032	2,528	2,682	2,619	0,035	2,538	2,680	2,627	0,037
UGOL	91,940%	0,064	-0,034	2,533	2,682	2,625	0,034	2,547	2,689	2,641	0,036
KTGW	93,175%	0,050	-0,026	2,536	2,696	2,626	0,035	2,549	2,693	2,633	0,036
RKNN	95,065%	0,044	-0,029	2,508	2,693	2,623	0,037	2,538	2,689	2,634	0,036
YUTO	93,503%	0,059	-0,027	2,516	2,711	2,627	0,036	2,550	2,692	2,638	0,035

Table 38: Total zenith delay: Comparison between RTnet solution and Bernese solution (Uji_9)

Sigma = 0,005 m/min (after linear trend removal)											
	UJI_9 vs UJI RTnet			UJI_9				UJI RTnet			
STATION	CORRELATION INDEX [-]	MAXIMUM DIFFERENCE [m]	MINIMUM DIFFERENCE [m]	Min [m]	Max [m]	Mean [m]	Std [m]	Min [m]	Max [m]	Mean [m]	Std [m]
FPOL	93,970%	0,042	-0,034	2,541	2,705	2,638	0,036	2,553	2,690	2,638	0,036
KUJI	94,275%	0,039	-0,032	2,551	2,702	2,638	0,035	2,545	2,695	2,638	0,036
SAYM	93,887%	0,043	-0,040	2,543	2,717	2,637	0,040	2,547	2,691	2,637	0,040
ISDA	93,044%	0,042	-0,045	2,551	2,701	2,637	0,035	2,548	2,690	2,638	0,036
MMKI	87,216%	0,057	-0,093	2,539	2,701	2,615	0,034	2,544	2,680	2,615	0,033
SCIN	93,847%	0,036	-0,033	2,538	2,696	2,613	0,034	2,551	2,694	2,613	0,033
KMSM	93,577%	0,046	-0,042	2,541	2,701	2,635	0,035	2,543	2,693	2,635	0,037
OYMZ	92,204%	0,053	-0,049	2,549	2,699	2,642	0,034	2,553	2,696	2,642	0,035
SKRA	93,097%	0,045	-0,032	2,541	2,698	2,632	0,034	2,544	2,684	2,632	0,034
KOGR	94,552%	0,043	-0,052	2,542	2,701	2,637	0,038	2,547	2,691	2,637	0,037
RISH	94,577%	0,033	-0,038	2,534	2,689	2,627	0,035	2,538	2,680	2,627	0,037
UGOL	92,161%	0,048	-0,048	2,547	2,698	2,641	0,035	2,547	2,689	2,641	0,036
KTGW	93,120%	0,042	-0,035	2,545	2,704	2,633	0,035	2,549	2,693	2,633	0,036
RKNN	94,949%	0,035	-0,040	2,519	2,700	2,634	0,036	2,538	2,689	2,634	0,036
YUTO	93,376%	0,048	-0,039	2,530	2,721	2,638	0,036	2,550	2,692	2,638	0,035

Table 39: Total zenith delay: Comparison between RTnet solution and Bernese after linear trend removal solution (Uji_9)

In order to analyze the sensitivity of the sigma parameter also the Uji_10 campaign is performed. In this case the parameter is set to 0,009 meter/minute.

In Table 40 and Table 41 statistics are reported for original and after linear trend removal solution. In Figure 43 and in Figure 44 the graphical representations are reported, as an example, for YUTO station.

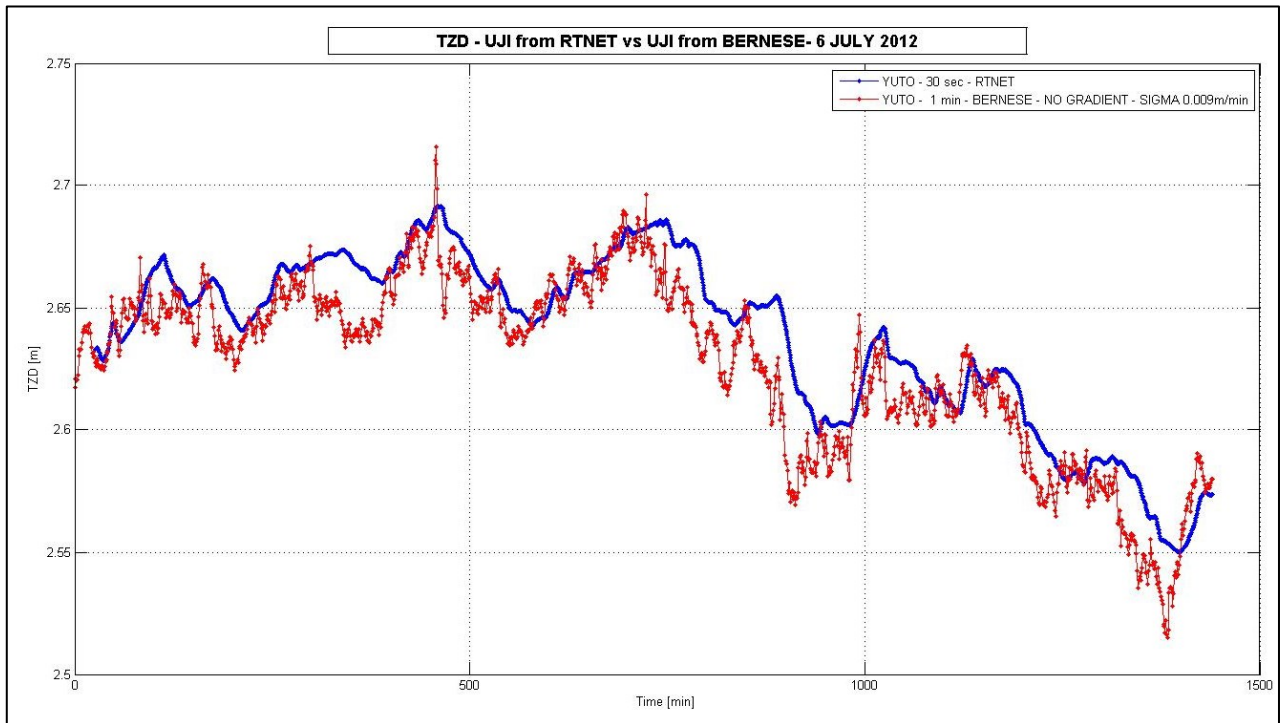


Figure 43: Tropospheric zenith delay for YUTO station, Bernese solution in red (Uji_10)

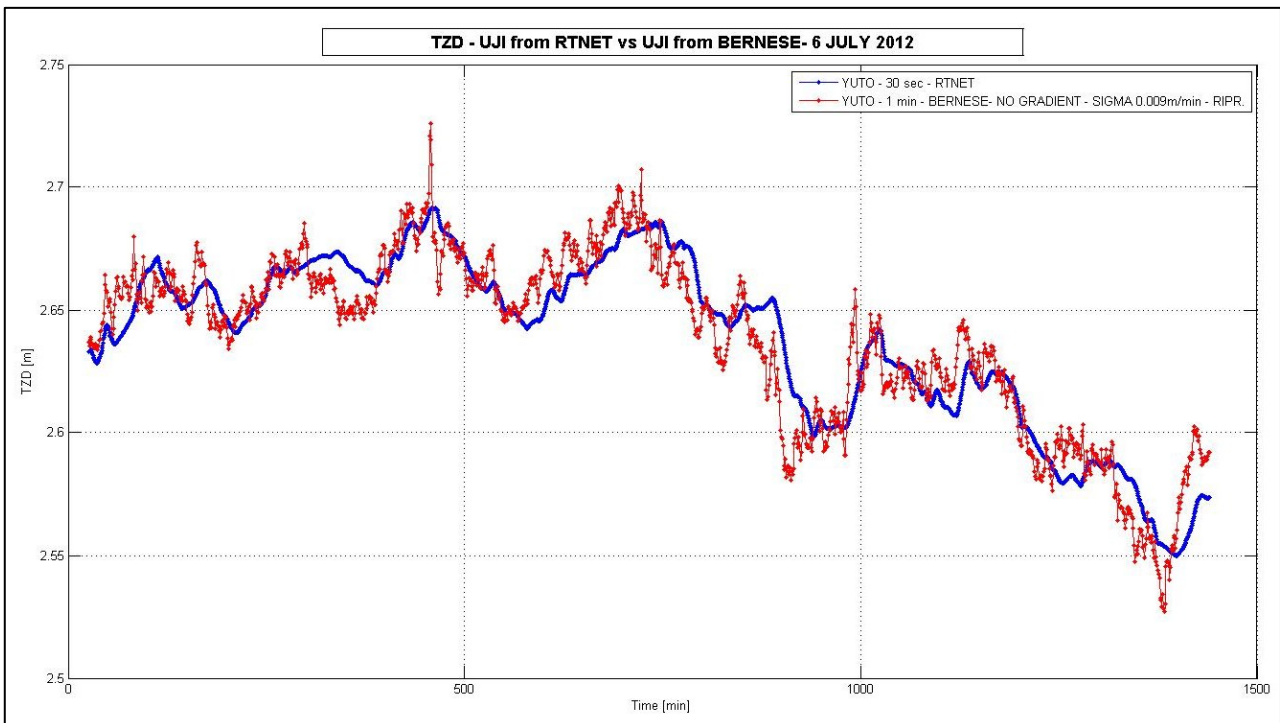


Figure 44: Tropospheric zenith delay for YUTO station, Bernese after linear trend removal solution in red (Uji_10)

Sigma = 0,009 m/min											
	UJI_10 vs UJI RTnet			UJI_10				UJI RTnet			
STATION	CORRELATION INDEX [-]	MAXIMUM DIFFERENCE [m]	MINIMUM DIFFERENCE [m]	Min [m]	Max [m]	Mean [m]	Std [m]	Min [m]	Max [m]	Mean [m]	Std [m]
FPOL	93,246%	0,058	-0,025	2,530	2,691	2,625	0,034	2,553	2,690	2,638	0,036
KUJI	93,899%	0,052	-0,020	2,540	2,691	2,626	0,034	2,545	2,695	2,638	0,036
SAYM	92,995%	0,059	-0,032	2,533	2,701	2,623	0,037	2,547	2,691	2,637	0,040
ISDA	92,499%	0,057	-0,034	2,539	2,692	2,624	0,033	2,548	2,690	2,638	0,036
MMKI	85,785%	0,065	-0,085	2,538	2,702	2,625	0,031	2,544	2,680	2,615	0,033
SCIN	90,247%	0,062	-0,016	2,534	2,670	2,602	0,028	2,551	2,694	2,613	0,033
KMSM	93,235%	0,060	-0,029	2,531	2,692	2,624	0,034	2,543	2,693	2,635	0,037
OYMZ	91,947%	0,066	-0,044	2,534	2,689	2,632	0,035	2,553	2,696	2,642	0,035
SKRA	93,039%	0,061	-0,021	2,523	2,686	2,619	0,035	2,544	2,684	2,632	0,034
KOGR	93,268%	0,059	-0,030	2,535	2,689	2,624	0,034	2,547	2,691	2,637	0,037
RISH	94,331%	0,042	-0,033	2,525	2,686	2,619	0,035	2,538	2,680	2,627	0,037
UGOL	91,619%	0,071	-0,037	2,531	2,684	2,625	0,034	2,547	2,689	2,641	0,036
KTGW	92,920%	0,051	-0,028	2,534	2,697	2,626	0,035	2,549	2,693	2,633	0,036
RKNN	94,878%	0,045	-0,033	2,506	2,694	2,627	0,037	2,538	2,689	2,634	0,036
YUTO	93,287%	0,060	-0,033	2,515	2,716	2,627	0,036	2,550	2,692	2,638	0,035

Table 40: Total zenith delay: Comparison between RTnet solution and Bernese solution (Uji_10)

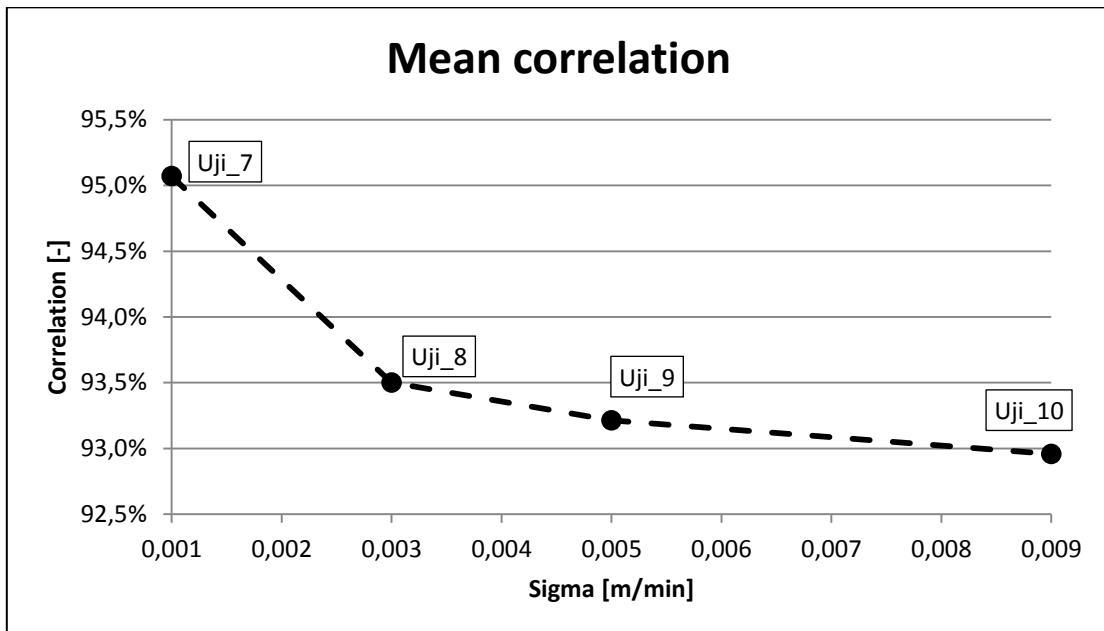
Sigma = 0,009 m/min (after linear trend removal)											
	UJI_10 vs UJI RTnet			UJI_10				UJI RTnet			
STATION	CORRELATION INDEX [-]	MAXIMUM DIFFERENCE [m]	MINIMUM DIFFERENCE [m]	Min [m]	Max [m]	Mean [m]	Std [m]	Min [m]	Max [m]	Mean [m]	Std [m]
FPOL	93,779%	0,046	-0,036	2,539	2,706	2,638	0,036	2,553	2,690	2,638	0,036
KUJI	94,073%	0,041	-0,033	2,550	2,704	2,638	0,035	2,545	2,695	2,638	0,036
SAYM	93,722%	0,045	-0,045	2,543	2,720	2,637	0,040	2,547	2,691	2,637	0,040
ISDA	92,796%	0,044	-0,046	2,549	2,705	2,638	0,035	2,548	2,690	2,638	0,036
MMKI	86,891%	0,061	-0,093	2,538	2,704	2,615	0,034	2,544	2,680	2,615	0,033
SCIN	93,553%	0,040	-0,034	2,537	2,698	2,613	0,034	2,551	2,694	2,613	0,033
KMSM	93,361%	0,050	-0,043	2,539	2,703	2,635	0,035	2,543	2,693	2,635	0,037
OYMZ	91,841%	0,055	-0,052	2,547	2,700	2,642	0,034	2,553	2,696	2,642	0,035
SKRA	92,863%	0,047	-0,033	2,539	2,699	2,632	0,034	2,544	2,684	2,632	0,034
KOGR	94,382%	0,047	-0,052	2,541	2,703	2,637	0,038	2,547	2,691	2,637	0,037
RISH	94,358%	0,036	-0,039	2,532	2,694	2,627	0,036	2,538	2,680	2,627	0,037
UGOL	91,860%	0,056	-0,050	2,545	2,700	2,641	0,035	2,547	2,689	2,641	0,036
KTGW	92,858%	0,043	-0,036	2,543	2,705	2,633	0,035	2,549	2,693	2,633	0,036
RKNN	94,752%	0,036	-0,044	2,517	2,702	2,634	0,036	2,538	2,689	2,634	0,036
YUTO	93,155%	0,049	-0,045	2,527	2,726	2,638	0,036	2,550	2,692	2,638	0,035

Table 41: Total zenith delay: Comparison between RTnet solution and Bernese after linear trend removal solution (Uji_10)

In Table 42 the mean correlation coefficient values are reported for the three campaigns (Uji_7, Uji_8, Uji_9 and Uji_10). In this evaluation the anomalous station, MMKI, is excluded. Graph 1 shows better the relationship between the sigma value and the correlation.

	Uji_7	Uji_8	Uji_9	Uji_10
Mean correlation index [-]	95,069%	93,500%	93,213%	92,958%
Sigma [m/min]	0,001	0,003	0,005	0,009

Table 42: Mean correlation coefficient for Uji_7, Uji_8, Uji_9 and Uji_10 campaigns



Graph 1: Graphical representation of mean correlation coefficients for Uji_7, Uji_8, Uji_9, and Uji_10

As already written, a higher sigma value implies a lower correlation. From the above graph this behavior is evident; in Table 43 are reported the angular coefficients derived from a linear interpolation of the points in Graph 1.

	Uji_7 vs Uji_8	Uji_8 vs Uji_9	Uji_9 vs Uji_10
Angular coefficient	7,847	1,435	0,638

Table 43: Angular coefficient between Uji_7, Uji_8, Uji_9 and Uji_10

So increasing the sigma value corresponds to a nonlinear decrement in the correlation between the two solutions.

The same procedure is followed in Uji_11 and Uji_12 campaigns.

In Table 44 and in Table 45 statistics are reported for Uji_11 and Uji_12 campaigns.

Sigma = 0,0001 m/min											
	UJI_11 vs UJI RTnet			UJI_11				UJI RTnet			
STATION	CORRELATION INDEX [-]	MAXIMUM DIFFERENCE [m]	MINIMUM DIFFERENCE [m]	Min [m]	Max [m]	Mean [m]	Std [m]	Min [m]	Max [m]	Mean [m]	Std [m]
FPOL	96,366%	0,041	-0,017	2,560	2,670	2,628	0,031	2,553	2,690	2,638	0,036
KUJI	96,345%	0,041	-0,018	2,563	2,669	2,628	0,031	2,545	2,695	2,638	0,036
SAYM	96,434%	0,042	-0,015	2,557	2,668	2,624	0,034	2,547	2,691	2,637	0,040
ISDA	96,150%	0,037	-0,034	2,561	2,667	2,626	0,030	2,548	2,690	2,638	0,036
MMKI	92,984%	0,028	-0,067	2,564	2,672	2,625	0,025	2,544	2,680	2,615	0,033
SCIN	96,420%	0,046	-0,014	2,564	2,649	2,604	0,024	2,551	2,694	2,613	0,033
KMSM	96,019%	0,033	-0,034	2,562	2,669	2,627	0,031	2,543	2,693	2,635	0,037
OYMZ	95,182%	0,035	-0,028	2,564	2,672	2,634	0,031	2,553	2,696	2,642	0,035
SKRA	95,735%	0,040	-0,013	2,551	2,661	2,622	0,031	2,544	2,684	2,632	0,034
KOGR	96,880%	0,036	-0,031	2,562	2,668	2,627	0,031	2,547	2,691	2,637	0,037
RISH	96,422%	0,033	-0,022	2,554	2,664	2,622	0,031	2,538	2,680	2,627	0,037
UGOL	95,554%	0,041	-0,016	2,561	2,667	2,626	0,030	2,547	2,689	2,641	0,036
KTGW	94,899%	0,045	-0,024	2,559	2,667	2,628	0,031	2,549	2,693	2,633	0,036
RKNN	96,938%	0,033	-0,019	2,552	2,668	2,629	0,032	2,538	2,689	2,634	0,036
YUTO	95,900%	0,041	-0,013	2,557	2,671	2,629	0,032	2,550	2,692	2,638	0,035

Table 44: Total zenith delay: Comparison between RTnet solution and Bernese solution (Uji_11)

Sigma = 0,0005 m/min											
	UJI_12 vs UJI RTnet			UJI_12				UJI RTnet			
STATION	CORRELATION INDEX [-]	MAXIMUM DIFFERENCE [m]	MINIMUM DIFFERENCE [m]	Min [m]	Max [m]	Mean [m]	Std [m]	Min [m]	Max [m]	Mean [m]	Std [m]
FPOL	94,959%	0,044	-0,014	2,546	2,681	2,626	0,033	2,553	2,690	2,638	0,036
KUJI	95,446%	0,043	-0,012	2,549	2,682	2,626	0,033	2,545	2,695	2,638	0,036
SAYM	94,639%	0,044	-0,017	2,539	2,680	2,623	0,036	2,547	2,691	2,637	0,040
ISDA	94,660%	0,043	-0,028	2,547	2,677	2,624	0,032	2,548	2,690	2,638	0,036
MMKI	88,218%	0,042	-0,082	2,546	2,694	2,625	0,030	2,544	2,680	2,615	0,033
SCIN	94,182%	0,041	-0,010	2,547	2,658	2,602	0,027	2,551	2,694	2,613	0,033
KMSM	95,276%	0,036	-0,027	2,549	2,681	2,625	0,033	2,543	2,693	2,635	0,037
OYMZ	93,901%	0,047	-0,031	2,547	2,681	2,632	0,034	2,553	2,696	2,642	0,035
SKRA	94,781%	0,046	-0,012	2,534	2,671	2,620	0,034	2,544	2,684	2,632	0,034
KOGR	95,119%	0,043	-0,031	2,546	2,678	2,625	0,034	2,547	2,691	2,637	0,037
RISH	95,844%	0,034	-0,021	2,538	2,673	2,620	0,034	2,538	2,680	2,627	0,037
UGOL	93,873%	0,046	-0,018	2,544	2,677	2,625	0,033	2,547	2,689	2,641	0,036
KTGW	94,662%	0,045	-0,015	2,544	2,679	2,626	0,034	2,549	2,693	2,633	0,036
RKNN	96,235%	0,037	-0,017	2,526	2,680	2,627	0,036	2,538	2,689	2,634	0,036
YUTO	94,932%	0,050	-0,015	2,536	2,681	2,627	0,035	2,550	2,692	2,638	0,035

Table 45: Total zenith delay: Comparison between RTnet solution and Bernese solution (Uji_12)

In Figure 45 and in Figure 46 the graphical representations are reported, as an example, for YUTO station.

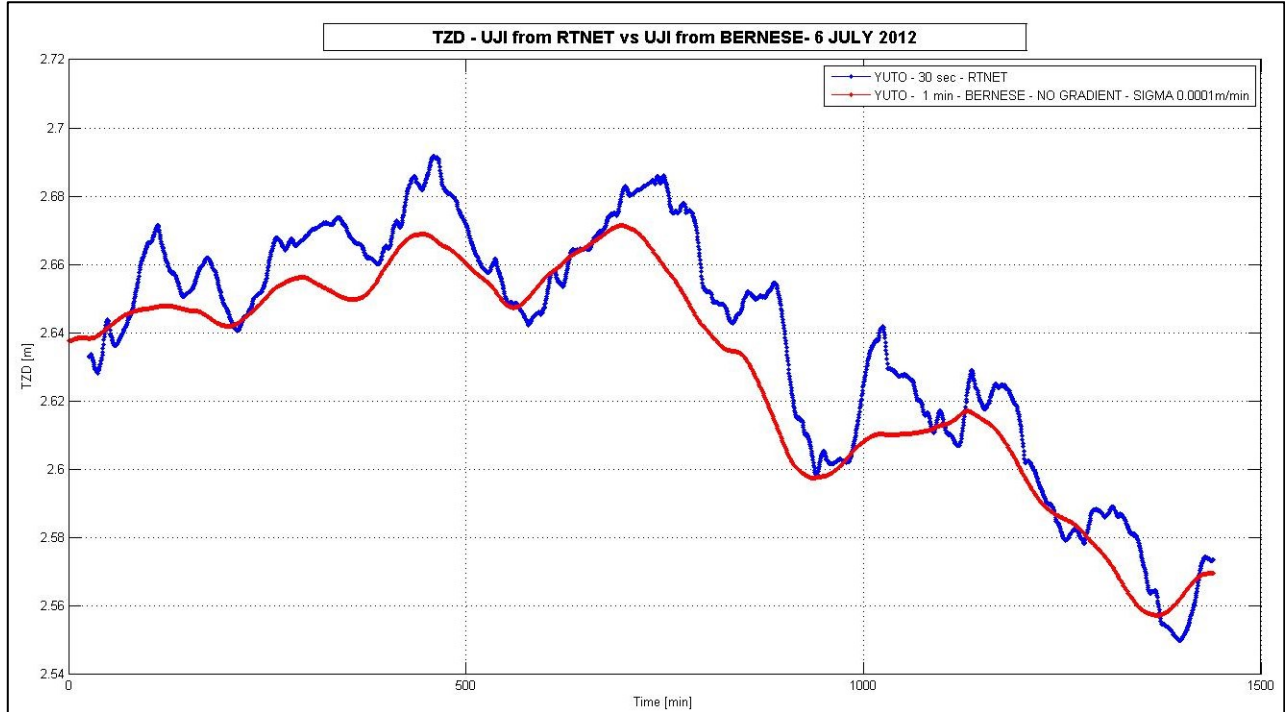


Figure 45: Tropospheric zenith delay for YUTO station, Bernese solution in red (Uji_11)

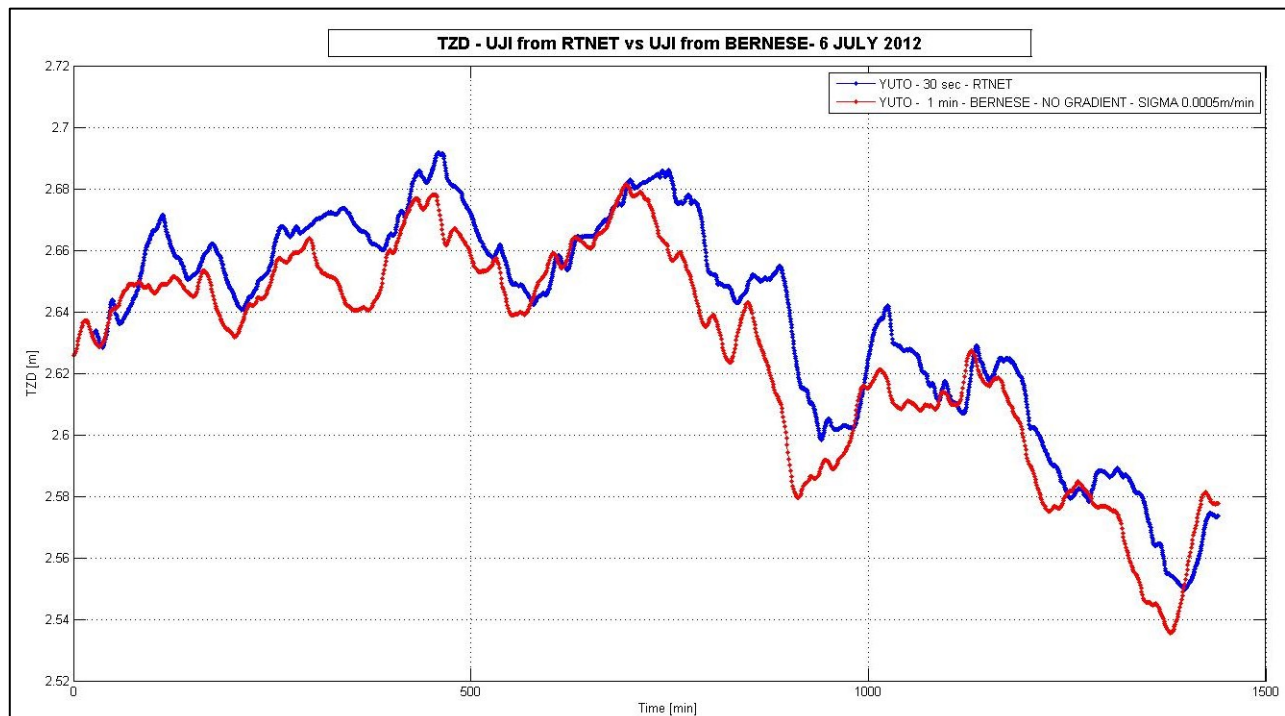
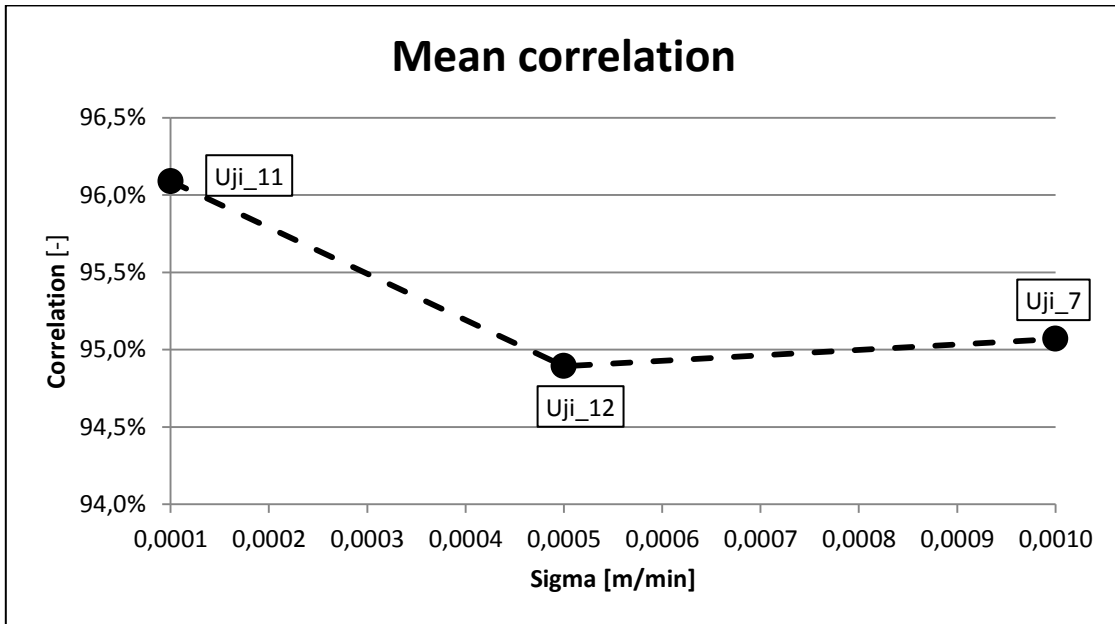


Figure 46: Tropospheric zenith delay for YUTO station, Bernese solution in red (Uji_12)

In Table 46 and in Graph 2 the homologous results of before are reported. Also in this case the MMKI station is excluded for this comparison.

	Uji_7	Uji_11	Uji_12
Mean correlation index [-]	95,069%	96,089%	94,893%
Sigma [m/min]	0,001	0,0001	0,0005

Table 46: Mean correlation coefficient for Uji_7, Uji_11 and Uji_12 campaigns



Graph 2: Graphical representation of mean correlation coefficients for Uji_7, Uji_11 and Uji_12

Now one can say that the situation is the reverse of before. That's true from the mathematical point of view, but looking carefully to Figure 45 and Figure 46 it is evident that not only the correlation coefficient has to be taken into account for this comparison.

In the previous tables, Table 44 and Table 45, also minimum, maximum, mean and standard deviation values are reported. This last index has to be analyzed in detail. For Uji_11 solution, in all the stations, it is always lower for the Bernese solution with respect to the RTnet solution. The same happens for Uji_12 solution. Instead, comparing the two Bernese solutions it is evident that the lower standard deviation values are for Uji_11. This is the reasons of the behavior shown in the two figures cited above.

The lowest sigma value brings a higher correlation coefficient and lower standard deviation values, and so, graphically speaking, the solution is smoother. Instead, Uji_12 sigma value brings a lower correlation coefficient, with respect to Uji_11, and higher standard deviation values.

In the next Table 47 and Table 48, sample size of the dataset and mean and standard deviation values for the differences between the solutions are reported.

	Bernese campaings						Rtnet
	UJI_7	UJI_8	UJI_9	UJI_10	UJI_11	UJI_12	
	# samples	# samples	# samples	# samples	# samples	# samples	
FPOL	1441	1441	1441	1441	1441	1441	2830
KUJI	1441	1441	1441	1441	1441	1441	2830
SAYM	1221	1221	1221	1221	1221	1221	2391
ISDA	1441	1441	1441	1441	1441	1441	2830
MMKI	1391	1391	1391	1391	1391	1391	1663
SCIN	711	711	711	711	711	711	1371
KMSM	1441	1441	1441	1441	1441	1441	2830
OYMZ	1441	1441	1441	1441	1441	1441	2830
SKRA	1441	1441	1441	1441	1441	1441	2830
KOGR	1376	1376	1376	1376	1376	1376	2677
RISH	1441	1441	1441	1441	1441	1441	2830
UGOL	1441	1441	1441	1441	1441	1441	2810
KTGW	1441	1441	1441	1441	1441	1441	2800
RKNN	1441	1441	1441	1441	1441	1441	2670
YUTO	1441	1441	1441	1441	1441	1441	2830

Table 47: Sample size of the different campaigns

	UJI_7-RTnet		UJI_8-RTnet		UJI_9-RTnet		UJI_10-RTnet		UJI_11-RTnet		UJI_12-RTnet	
	mean [m]	std [m]	mean [m]	std [m]	mean [m]	std [m]	mean [m]	std [m]	mean [m]	std [m]	mean [m]	std [m]
FPOL	0,011	0,011	0,013	0,013	0,013	0,013	0,013	0,013	0,011	0,010	0,012	0,011
KUJI	0,015	0,011	0,012	0,012	0,012	0,012	0,012	0,013	0,011	0,011	0,012	0,011
SAYM	0,014	0,013	0,015	0,014	0,015	0,014	0,015	0,015	0,013	0,011	0,015	0,013
ISDA	0,013	0,011	0,014	0,013	0,014	0,014	0,014	0,014	0,012	0,011	0,013	0,012
MMKI	0,006	0,016	0,004	0,017	0,004	0,017	0,003	0,017	0,001	0,013	0,004	0,015
SCIN	0,016	0,013	0,014	0,014	0,014	0,014	0,014	0,015	0,011	0,013	0,014	0,013
KMSM	0,011	0,011	0,011	0,013	0,011	0,013	0,011	0,013	0,009	0,011	0,011	0,011
OYMZ	0,012	0,012	0,011	0,014	0,011	0,014	0,011	0,014	0,008	0,011	0,010	0,012
SKRA	0,013	0,011	0,013	0,013	0,013	0,013	0,013	0,013	0,010	0,010	0,012	0,011
KOGR	0,012	0,011	0,013	0,013	0,013	0,013	0,013	0,013	0,011	0,010	0,013	0,012
RISH	0,008	0,010	0,007	0,012	0,007	0,012	0,007	0,012	0,005	0,010	0,007	0,010
UGOL	0,016	0,012	0,016	0,014	0,016	0,014	0,016	0,014	0,015	0,011	0,016	0,012
KTGW	0,009	0,012	0,008	0,013	0,008	0,013	0,008	0,013	0,006	0,012	0,008	0,012
RKNN	0,010	0,010	0,009	0,011	0,009	0,012	0,009	0,012	0,007	0,009	0,009	0,010
YUTO	0,012	0,011	0,011	0,013	0,011	0,013	0,011	0,013	0,009	0,010	0,011	0,011

Table 48: Mean and standard deviation for the differences between Bernese and RTnet solutions

4.3.2 Time windows solutions

Unlike the RTnet kalman solution, the batch Bernese PPP solution requires an adjustment of a minimum number of epochs to solve for all the parameters involved.

Some different time horizon are set up in order to check this behavior. The first time window starts at midnight and ends at one. This is done till midnight.

These experiments are performed only for the FPOL station.

In Table 49, the time windows, in which the estimation is performed, are reported.

Campaign name	Time window	
	From	To
Uji_13	00 – 00 – 00	01 – 00 – 00
Uji_15	00 – 00 – 00	02 – 00 – 00
Uji_16	00 – 00 – 00	03 – 00 – 00
Uji_17	00 – 00 – 00	04 – 00 – 00
Uji_18	00 – 00 – 00	05 – 00 – 00
Uji_19	00 – 00 – 00	06 – 00 – 00
Uji_20	00 – 00 – 00	07 – 00 – 00
Uji_21	00 – 00 – 00	08 – 00 – 00
Uji_22	00 – 00 – 00	09 – 00 – 00
Uji_23	00 – 00 – 00	10 – 00 – 00
Uji_37	00 – 00 – 00	12 – 00 – 00
Uji_36	00 – 00 – 00	13 – 00 – 00
Uji_35	00 – 00 – 00	14 – 00 – 00
Uji_34	00 – 00 – 00	15 – 00 – 00
Uji_33	00 – 00 – 00	16 – 00 – 00
Uji_32	00 – 00 – 00	17 – 00 – 00
Uji_31	00 – 00 – 00	18 – 00 – 00
Uji_30	00 – 00 – 00	19 – 00 – 00
Uji_29	00 – 00 – 00	20 – 00 – 00
Uji_28	00 – 00 – 00	21 – 00 – 00
Uji_27	00 – 00 – 00	22 – 00 – 00
Uji_26	00 – 00 – 00	23 – 00 – 00
Uji_25	00 – 00 – 00	24 – 00 – 00

Table 49: Basic information for Uji time windows solutions

The analysis is performed both in terms of coordinates and tropospheric zenith delay.

In Table 50 the coordinate results are reported in chronological order.

CAMP.	HEIGHT [m]	RMS [m]	LATITUDE	RMS [sec]	RMS [m]	LONGITUDE	RMS [sec]	RMS [m]
Uji_13	54,955	0,012	34°53'46,059"	0,003	0,093	135°45'18,201"	0,017	0,525
Uji_15	57,595	0,747	34°53'46,030"	0,269	8,309	135°45'17,890"	0,291	8,988
Uji_16	58,645	0,605	34°53'46,103"	0,210	6,486	135°45'18,088"	0,174	5,374
Uji_17	16,193	3,119	34°53'46,278"	1,452	44,849	135°45'17,919"	1,326	40,957
Uji_18	55,863	0,195	34°53'46,043"	0,068	2,1	135°45'18,194"	0,064	1,977
Uji_19	32,198	3,163	34°53'46,230"	0,459	14,177	135°45'17,964"	0,516	15,94
Uji_20	32,198	3,163	34°53'46,231"	0,459	14,180	135°45'17,965"	0,516	15,944
Uji_21	53,870	1,334	34°53'46,464"	0,548	16,917	135°45'17,979"	0,462	14,276
Uji_22	57,207	0,380	34°53'46,073"	0,101	3,123	135°45'18,198"	0,086	2,653
Uji_23	67,337	4,296	34°53'45,501"	1,555	48,033	135°45'18,479"	2,235	69,034
Uji_37	55,088	0,002	34°53'46,057"	0,000	0,009	135°45'18,200"	0,005	0,151
Uji_36	55,011	0,003	34°53'46,059"	0,001	0,025	135°45'18,194"	0,002	0,053
Uji_35	55,096	0,007	34°53'46,059"	0,002	0,059	135°45'18,201"	0,004	0,114
Uji_34	55,286	0,005	34°53'46,059"	0,001	0,019	135°45'18,199"	0,003	0,105
Uji_33	55,068	0,047	34°53'46,060"	0,007	0,219	135°45'18,196"	0,008	0,232
Uji_32	54,242	0,056	34°53'46,075"	0,015	0,448	135°45'18,182"	0,016	0,491
Uji_31	54,770	0,013	34°53'46,057"	0,002	0,074	135°45'18,200"	0,005	0,151
Uji_30	55,811	0,140	34°53'46,056"	0,028	0,859	135°45'18,169"	0,035	1,069
Uji_29	55,141	0,026	34°53'46,058"	0,005	0,161	135°45'18,192"	0,010	0,300
Uji_28	55,800	0,064	34°53'46,067"	0,018	0,568	135°45'18,185"	0,010	0,300
Uji_27	54,724	0,081	34°53'46,050"	0,020	0,608	135°45'18,189"	0,025	0,766
Uji_26	54,933	0,104	34°53'46,057"	0,014	0,420	135°45'18,177"	0,021	0,649
Uji_25	55,090	0,001	34°53'46,059"	0,000	0,006	135°45'18,195"	0,001	0,015

Table 50: Coordinate results for time windows solutions

Anomalous solutions are highlighted in bold format. The RMS errors are very high; those solutions are not acceptable.

In Table 51 the tropospheric solution is reported, in chronological order, in term of minimum, maximum, mean and standard deviation values. Also the number of samples is reported.

Campaign	Min [m]	Max [m]	Mean [m]	Std [m]	# samples
Uji_13	2,627	2,656	2,643	0,008	60
Uji_15	2,395	2,402	2,399	0,003	120
Uji_16	2,660	2,669	2,665	0,003	180
Uji_17	5,338	5,346	5,343	0,002	240
Uji_18	2,707	2,735	2,721	0,010	300
Uji_19	7,238	7,252	7,246	0,004	360
Uji_20	3,138	3,154	3,144	0,005	420
Uji_21	1,197	1,235	1,215	0,012	480
Uji_22	2,515	2,668	2,574	0,050	540
Uji_23	3,057	3,235	3,117	0,054	600
Uji_37	2,622	2,688	2,651	0,015	720
Uji_36	2,578	2,693	2,650	0,028	780
Uji_35	2,619	2,713	2,668	0,020	840
Uji_34	2,590	2,669	2,648	0,020	900
Uji_33	2,515	2,724	2,625	0,063	960
Uji_32	2,742	2,897	2,817	0,044	1020
Uji_31	2,613	2,716	2,674	0,019	1080
Uji_30	2,469	2,598	2,547	0,039	1140
Uji_29	2,567	2,703	2,657	0,036	1200
Uji_28	2,555	2,648	2,602	0,029	1260
Uji_27	2,464	2,785	2,694	0,073	1320
Uji_26	2,486	2,561	2,535	0,020	1380
Uji_25	2,546	2,681	2,626	0,033	1440

Table 51: Minimum, maximum, mean and standard deviation of tropospheric zenith delay

Also in the table above the anomalous solutions are highlighted in bold format.

These anomalous solutions are originated by the fact that, in the specific time window, some satellites are observed for not enough time to permit an adequate estimation.

In Figure 47 an output example is reported for an anomalous campaign (Uji_17). Note the chi squared test value in the last line. It is another indicator of the quality for the estimation procedure.

```
A POSTERIORI SIGMA OF UNIT WEIGHT (PART 1):
-----
A POSTERIORI SIGMA OF UNIT WEIGHT : 0.0166 M (SIGMA OF ONE-WAY L1 PHASE OBSERVABLE AT ZENITH)
DEGREE OF FREEDOM (DOF) : 74
CHI**2/DOF : 276.08
```

Figure 47: Output example after the estimation of an anomalous campaign (Uji_17)

Considering the above results a new set of campaigns is built in order to check if the minimum number of hours to reach a reasonable solution is twelve. The Uji_40 campaign starts from midday till midnight. The Uji_41 starts from six till eighteen.

In Table 52 and in Table 53 results are reported.

CAMP.	HEIGHT [m]	RMS [m]	LATITUDE	RMS [sec]	RMS [m]	LONGITUDE	RMS [sec]	RMS [m]
Uji_40	55,097	0,002	34°53' 46,059"	0,000	0,012	135°45' 18,195"	0,001	0,028
Uji_41	55,085	0,003	34°53'46,059"	0,001	0,019	135°45' 18,196"	0,001	0,043

Table 52: Coordinate results for Uji_40 (from midday to midnight) and Uji_41 (from six till eighteen)

Campaign	Min [m]	Max [m]	Mean [m]	Std [m]	# samples
Uji_40	2,542	2,673	2,600	0,031	720
Uji_41	2,585	2,679	2,651	0,033	720

Table 53: Tropospheric zenith delay results for Uji_40 (from midday to midnight) and Uji_41 (from six till eighteen)

Considering as reference campaign Uji_25 that covers all the day long, these solutions differ in the millimeter order for what concerns the total zenith delay statistics and also the coordinates are quite the same.

This last experiment suggests that twelve hours may be enough to obtain a reasonable solution. However this statement is valid only for this specific case. Moreover the window starting from midnight ending at eleven is not estimated at all.

So that the time window solutions are not always reliable and so it is not advisable this type of use of the software.

4.4 Results

In chapter four some examples are presented in order to understand the behavior of the software varying some parameters.

General considerations for the Precise point positioning, performed by the Bernese software, are:

- ◆ Comparable results in coordinate term with respect to the *Double differencing* technique
- ◆ Detailed modelling for the troposphere estimation:
 - The gradient model application implies a smoother solution
 - The maximum estimation rate for the troposphere, 1 min, is more than sufficient
 - The selection of the sigma parameter is directly and heavily connected to tropospheric parameter estimation

Conclusions and further improvements

This work is focused on reaching an adequate preliminary knowledge of the Bernese software. All the experiments are made for this purpose.

To achieve this goal some reference solutions have been used.

For what concern the Mist campaigns the term of comparison are the results coming from a *Double differences processing* technique plus the EUREF solution, for the troposphere estimates.

Instead for the Uji campaigns, a solution coming from another software is used. This last, in addition, was the starting point for a study focused to prove the reliability of GPS tropospheric signal delay for meteorologically application. Now that an use awareness's of the software is reached, the following work regards the possibility to improve the *Precise point positioning solution* in order to reach better troposphere estimates. To do this, for example, the station coordinates could be settled as constrained. Then the directly comparison between the GPS derived precipitable water vapor and the measured one has to be done.

References

- Ahmed, E.-R. (2008). *Introduction to GPS* (Vol. 26). <http://doi.org/10.3167/gps.2008.260401>
- Andrews, D. (2010). *An Introduction to Atmospheric Physics* (Second edi). Cambridge University Press.
- Ashby, N. (2003). Relativity in the Global Positioning. *Living Reviews in Relativity*, 42. <http://doi.org/10.1063/1.1485583>
- Awange, J. L. (2011). *Environmental monitoring using GNSS. Environmental Science and Engineering* (Vol. 3).
- Awange, J. L., & Kiema, J. B. K. (2013). *Environmental Geoinformatics*. <http://doi.org/10.1007/978-3-642-34085-7>
- Bernese GPS Software version 5.0, user manual.* (2007). Astronomical Institute, University of Bern.
- Bevis, M., Businger, S., Herring, T. a., Rocken, C., Anthes, R. a., & Ware, R. H. (1992). GPS meteorology - Remote sensing of atmospheric water vapor using the Global Positioning System, 97(92), 787–801. <http://doi.org/10.1029/92JD01517>
- Boehm, J., Heinkelmann, R., & Schuh, H. (2007). Short note: A global model of pressure and temperature for geodetic applications. *Journal of Geodesy*, 81(10), 679–683. <http://doi.org/10.1007/s00190-007-0135-3>
- Champion, F. C. (1960). *University Physics*. (G. Blackie & Son Ltd, Ed.).
- Chatzinikos, M., Fotiou, A., & Pikridas, C. (2009). The effects of the Receiver and Satellite Antenna Phase Center Models on Local and Regional Gps Networks. *Practice*, (November), 05 – 06.
- Davis, J. L., & Herrinch, T. A. (1985). Geodesy by radio interferometry: Effects of atmospheric modeling errors on estimates of baseline length, 1593–1607.
- Emardson, T. R., & Derk, H. J. P. (1998). On the relation between the wet delay and the integrated precipitable water vapour in the European atmosphere. *Doktorsavhandlingar Vid Chalmers Tekniska Hogskola*, 68(1404), 61–68. <http://doi.org/10.1017/S1350482700001377>
- Ferraro, C., & Nardi, A. (1996). Contribution to EUREF of the ASI (Agenzia Spaziale Italiana) Matera Space Geodesy Centre, 1–4.
- Fleming, Chandra, Barnett, & Corney. (1990). *Zonal mean temperature, pressure, zonal wind and geopotential height as functions of latitude*.
- Grimes, J. (2008). *Global Positioning System Standard Positioning Service*. Department of Defence, USA. Retrieved from <http://www.gps.gov/technical/ps/2008-SPS-performance-standard.pdf>

- Hall, M. P. M., Barcley, L. W., & Hewitt, M. T. (1996). *Propagation of Radiowaves*. The Institution of Electrical Engineers, London, England.
- Haltiner, G. J., & Martin, F. L. (1957). *Dynamical and Physical Meteorology*. McGraw-Hill Book Company, New York.
- Hofmann-Wellenhof, B., Lichtenegger, H., & Wasle, E. (2008). *GNSS – GPS, GLONASS, GALILEO and more*. SpringerWienNewYork.
- Hopfield, H. (1969). Two-quartic tropospheric refractivity profile for correcting satellite data. *Journal of Geophysical Research*, 4487–4499. <http://doi.org/doi: 10.1029/JC074i018p04487>
- <http://holt.oso.chalmers.se/loading/>. (n.d.). Ocean Tidal loading calculator.
- <http://www.g-red.eu/techniques-methods/gnss-meteorology/>. (n.d.). GNSS meteorology. Retrieved from <http://www.g-red.eu/techniques-methods/gnss-meteorology/>
- <Http://www.vmsi-microcosm.com/index.html>. (n.d.). Microcosm software.
- <https://igscb.jpl.nasa.gov/igscb/station/general/antex14.txt>. (n.d.). Antex file description.
- Jaume, S. S., José Miguel Juan, Z., & Manuel, H.-P. (2013). *Gnss Data Processing* (Vol. II). ESA.
- Kleijer, F. (2004). *Troposphere Modeling and Filtering for Precise GPS Leveling*.
- Kouba, J. A. N., & Heroux, P. (2001). Precise Point Positioning Using IGS Orbit and Clock Products, 5(2), 12–28.
- Leick, A. (2004). *GPS satellite surveyng* (3rd ed.). John Wiley & Sons.
- Martin, I. (2013). GNSS Precise Point Positioning : The enhancement with GLONASS.
- Meindl, M., Schaer, S., Hugentobler, U., & Beutler, G. (2004). Tropospheric Gradient Estimation at CODE: Results from Global Solutions. *Journal of the Meteorological Society of Japan*, 82(1B), 331–338. <http://doi.org/10.2151/jmsj.2004.331>
- Mendes, V. B. (1999). *Modeling the Propagation Delay in Radiometric Space Techniques*. Department of Geodesy and Geomatics Engineering, University of New Brunswick, Canada.
- Niell, A. E. (1996). Global mapping functions for the atmosphere delay at radio wavelengths. *Journal of Geophysical Research*, 3227–3246. <http://doi.org/doi:10. 1029/95JB03048>
- Realini, E., Tsuda, T., Sato, K., Oigawa, M., & Iwaki, Y. (2012). Analysis of the temporal and spatial variability of the wet troposphere at a local scale by high-rate PPP using a dense GNSS network. *Computer*, 3406–3412.
- Reguzzoni, I. (2012). *Gps tropospheric delays for meteorological applications*.

Saastamoinen, J. (1959). National Research Council of Canada. *Nature*.
<http://doi.org/10.1038/1841916b0>

Schuh, H., & Estermann, G. (2002). Atmospheric, Non-tidal oceanic and hydrological loading investigated by VLBI, 219–224.

Seeber, G. (2003). *Satellite Geodesy*. <http://doi.org/10.1515/9783110200089>

Smith, E. K., & Weintraub, S. (1953). *The constants in the equation for atmospheric refractive index at radio frequencies*. in Proc. IRE 41, pp. 1035–1037.

Stull, R. B. (1995). *Meteorology: For Scientists and Engineers*. West Publishing, St. Paul, Minneapolis.

Subirana, J. S., Zornoza, J., & Hernandez-Pajares, M. (2013). *Gnss Data Processing*. (K. Fletcher, Ed.) (Vol. II). ESA Communications.

Teunissen, P. J. G., & Kleusberg, a. (1998). *GPS for Geodesy*. <http://doi.org/10.1007/978-3-642-72011-6>

Tregoning, P., & van Dam, T. (2005). Atmospheric pressure loading corrections applied to GPS data at the observation level. *Geophysical Research Letters*, 32(22), 1–4.
<http://doi.org/10.1029/2005GL024104>

Wallace, J. M., & Hobbs, P. V. (2006). *Atmospheric Science: An Introductory Survey*. *Annals of surgery* (Vol. 92). <http://doi.org/10.1007/s007690000247>

Zumberge, J. F., Heflin, M. B., Jefferson, D. C., Watkins, M. M., & Webb, F. H. (1997). Precise point positioning for the efficient and robust analysis of GPS data from large networks. *Journal of Geophysical Research*, 102(B3), 5005. <http://doi.org/10.1029/96JB03860>

Acknowledgments

I'm very grateful to my supervisors, Prof.ssa Giovanna Venuti and Dott. Eugenio Realini, for giving me the opportunity to collaborate with them and for helping me during this thesis work. Special thanks go also to Dott. Alessandro Fermi, especially for taking the time to discuss with me of so many different problems caused by the software. I would also like to thank all members of the Geomatic Laboratory.

I wish to thank also my mates, in particular Walter, Daniele and Sanya. They have made these years enjoyable and have always encouraged me to do better.

Thanks to all my family for believing in me, especially in moments of discouragement in which they always encouraged me.